Copyright

by

Elsa Maalouf

2017

The Dissertation Committee for Elsa Maalouf Certifies that this is the approved version of the following dissertation:

Rapid Modeling and Inversion-Based Interpretation of Borehole Acoustic Measurements Acquired in Isotropic and Vertical Transversely Isotropic Formations

Committee:

Carlos Torres-Verdín, Supervisor

Hugh Daigle

Zoya Heidari

Kamy Sepehrnoori

Kyle T. Spikes

Rapid Modeling and Inversion-Based Interpretation of Borehole Acoustic Measurements Acquired in Isotropic and Vertical Transversely Isotropic Formations

by

Elsa Maalouf

Dissertation

Presented to the Faculty of the Graduate School of

The University of Texas at Austin

in Partial Fulfillment

of the Requirements

for the Degree of

Doctor of Philosophy

The University of Texas at Austin

December 2017

Dedication

To my beloved mother Mona, for her endless encouragement and unconditional support.

Acknowledgements

I want to thank my advisor, Dr. Carlos Torres-Verdín for his consistent support and guidance which made this dissertation possible. I am immensely grateful to him for giving me a chance to be a member of the Formation Evaluation research group at the University of Texas at Austin. He has had an incommensurable influence on my way of thinking and shaping my thought processes during my graduate studies. I would like to acknowledge the members of my dissertation committee, Dr. Hugh Daigle, Dr. Zoya Heidari, Dr. Kamy Sepehrnoori, and Dr. Kyle Spikes for their time, support, and reviews of this dissertation. Special thanks to Rey Casanova for his administrative support at the Formation Evaluation research consortium.

I want to thank Frankie Hart and Amy Douglas Stewart in the Petroleum Engineering department for their constant administrative support. I am thankful to Roger Terzian, Joaquin Ambia-Garrido, and Bruce Klappauf for IT support. I am grateful to the petroleum engineering department at the University of Texas at Austin, for providing travel and financial grants to attend professional and industry conferences.

Special thanks to Ron Bonnie, Mark Shannon, Ayelet Harris, and Li Ji for mentoring me during my time at ConocoPhillips. I extend my gratitude to Jim Seccombe, Adrian Purdy, Andy Brickell, Mehrnoosh Saneifar, and Amir Rangwala for their guidance and the opportunity to work in the geophysics team at BhP Billiton during the Summer of 2016.

I would like to thank my friends and colleagues at UT Austin: Vivek Ravi, Juan-Diego Escobar, Shaina Kelly, Tianqi Deng, Paul Sayar, Shan Huang, Mohammed Bennis, Siddharth Misra, Eva Vinegar, Mathilde Luycx, Adam McMullen, Colin Schroeder,

Elton Ferreria, Artur Posenato, Amir Frooqnia, Edwin Ortega, Hyungjoo Lee, David Gonzalez, Joshua Bautista-Anguiano, Mohammed Albusairi, and Jingxuan Liu.

A big thank you to the Postdoctoral fellows of the Formation Evaluation research group: David Medellin, Wilberth Herrera, Ruijia Wang, Ayaz Mehmani, and Pawel Matuszyk.

Finally, I am immensely grateful to my family for their never-failing support and patience throughout this journey. I thank my parents Walid and Mona, and my siblings Jihane, Diane, and Elio. I am grateful for their love, their guidance, and their prayers.

The work reported in this dissertation was funded by University of Texas at Austin Research Consortium on Formation Evaluation, jointly sponsored by AkerBP, Anadarko, Aramco, Baker-Hughes, BHP Billiton, BP, China Oilfield Services LTD., Chevron, ConocoPhillips, DEA, ENI, ExxonMobil, Hess, Inpex, Lundin-Norway, Nexen, Petrobras, Repsol, Shell, Southwestern, Statoil, TOTAL, Wintershall, and Woodside Petroleum Limited.

Rapid Modeling and Inversion-Based Interpretation of Borehole Acoustic Measurements Acquired in Isotropic and Vertical Transversely Isotropic Formations

Elsa Maalouf, Ph.D.

The University of Texas at Austin, 2017

Supervisor: Carlos Torres-Verdín

Borehole acoustic measurements are often affected by instrument noise, motion and eccentricity, environmental conditions, and spatial averaging that can compromise the accuracy of elastic properties of rock formations calculated with conventional interpretation methods. Forward and inverse modeling can be used to improve the interpretation of acoustic logs acquired in the presence of spatially complex rock formations and adverse borehole conditions. However, forward modeling of acoustic modes often requires time-consuming numerical algorithms.

The main objective of this dissertation is to develop fast-forward modeling and inversion-based interpretation procedures of borehole acoustic logs for isotropic and vertical transversely isotropic (VTI) formations. Fast-forward modeling is achieved with spatial sensitivity functions which are calculated from frequency-domain linear perturbation theory of borehole acoustic modes. Spatial sensitivity functions quantify both the dependence of measured slowness on elastic properties and the spatial averaging introduced by acoustic tools.

Fast-forward modeling using spatial sensitivity functions is applied to synthetic examples that include thin layers, anisotropy, and dipping layers, and is successfully

validated with numerical simulations performed with finite-difference and finite-element methods. Two inversion-based interpretation methods are then developed: (1) a physics-based inversion method to reduce noise and spatial averaging effects on acoustic logs acquired in horizontally layered formations penetrated by vertical wells, and (2) a sequential inversion method to estimate stiffness coefficients of VTI formations from multi-frequency flexural/quadrupole, Stoneley, and compressional logs.

The physics-based inversion method is applied to mitigate measurement noise and spatial averaging effects of acoustic logs acquired in two hydrocarbon reservoirs. Results confirm the accuracy and reliability of the estimated layer-by-layer elastic properties compared to conventional numerical filters and are obtained in less than 14 CPU seconds for a 100 ft-depth log.

In VTI formations penetrated by vertical wells, sequential inversion is applied to estimate layer-by-layer stiffness coefficients of synthetic formations from borehole acoustic logs. Results indicate that mitigating spatial averaging of frequency-dependent slowness logs prior to inversion improves the layer-by-layer estimation of slownesses by a factor of 2, and that sequential inversion yields accurate and reliable estimates of rock stiffness coefficients.

Finally, in high-angle wells fast-forward modeling yields flexural slownesses measured with orthogonal dipoles with 2% relative errors and in 3 CPU minutes for a log consisting of 50 measured-depth samples, compared to 15 CPU hours when using finite-difference simulation methods.

Analysis of field and synthetic examples confirms that inversion-based interpretation methods yield more accurate estimations of elastic properties than conventional sonic-log interpretation procedures. Spatial sensitivity functions constitute a

fast, reliable, and efficient alternative for interpreting acoustic logs acquired in isotropic and VTI formations.

Table of Contents

List of Tables

List of Figures

Chapter 1: Introduction

This dissertation introduces new methods for quantitative interpretation of wireline and logging-while-drilling borehole sonic measurements for isotropic and vertical transversely isotropic formations based on the physics of borehole measurements and inverse theory.

First, I develop a fast-forward model to calculate sonic borehole measurements (compressional, shear, flexural, quadrupole, and Stoneley modes) in vertical wells logged with wireline or logging-while-drilling (LWD) sonic instruments. Second, I introduce inversion-based interpretation methods of borehole acoustic logs for isotropic and vertical transversely isotropic (VTI) formations to mitigate noise and spatial averaging effects on acoustic logs, and estimate stiffness coefficients of layers. Finally, I extend the method for applications in high-angle wells for improved interpretation of sonic logs in complex geometries with azimuthal asymmetry.

1.1 Background and Problem Statement

Borehole acoustic logs are widely used in formation evaluation for optimal geosteering applications, fracturing operations, and reserves appraisal. Applications of borehole acoustic logs for petrophysical and seismic interpretations include:

- permeability estimation from Stoneley modes (Cheng and Tang, 1993; Tang and Cheng, 1996),
- fracture characterization (Prioul and Jocker, 2009),
- porosity and saturation estimations from shear and compressional logs (Wyllie et al., 1956; Lee and Waite, 2008),

- synthetic seismogram simulations for seismic interpretations (Luo and Schuster, 1991),
- description of stress-induced shear wave anisotropy for borehole stability applications (Kosset and Tutuncu, 2015),
- estimation of rock elastic properties for planning hydraulic fracturing operations (Willis et al., 2014), and
- pore pressure measurements for geosteering applications.

The interpretation of sonic logs, however, is affected by environmental noise and challenging features such as:

- averaging effects (Sams, 1995; Peyret and Torres-Verdín, 2006), when layers are thinner than the length of the receiver arrays of acoustic tools (typically between 3 ft and 6 ft),
- numerical noise, caused by the limitations of waveform processing algorithms (Kimball and Marzetta, 1984; Ellis and Singer, 2007),
- mode distortions (Mallan et al., 2011) at high-angle wells, when flexural modes interfere with Stoneley modes, biasing the estimation of shear slownesses from low-frequency flexural slownesses,
- residual tool modes and spatial aliasing in LWD operations (Market et al., 2001),
- borehole damage and variation of stress around the borehole that impact estimations of elastic properties (Winkler et al., 1998), and

- mud-filtrate invasion that produces unreliable estimates of elastic properties in vertical (Chi et al., 2006) and high-angle and horizontal (HA/HZ) wells from sonic logs.

Forward and inverse modeling of logs is often used to improve the interpretation of sonic logs acquired in one-dimensional (1D) (i.e., homogeneous formations) and two-dimensional (2D) media (i.e., heterogeneous formations with horizontal layers) penetrated by vertical wells. For example, in homogeneous formations, Burridge and Sinha (1996) calculate radial sensitivity functions of the flexural mode using first-order perturbation theory to quantify the effects of radial variations of formation elastic properties on the measured slownesses. Sinha (1997) applied a 1D inversion-based method, using radial sensitivity functions, to calculate flexural slownesses of formations exhibiting radial heterogeneities (i.e., altered zones surrounding the borehole or varying radial profiles of formation properties) (Sinha et al., 2006b). Similarly, Mallan et al. (2009) applied radial sensitivity functions to estimate elastic properties, porosity, and water saturation of 1D radial (homogeneous) models jointly from sonic and resistivity logs.

However, in heterogeneous formations (i.e., formations with horizontal layers), properties estimated with the above methods are often inaccurate because sonic logs are affected by spatial averaging effects and presence of thin beds that reduce the axial (i.e., along the direction of the borehole) resolution of logs. Hsu and Chang (1987) propose using sub-array processing of sonic waveforms to improve the axial resolution of sonic logs. They show that multi-shot semblance processing yields enhanced estimations of slownesses across bedded formations. However, this method is limited by depth

registration errors (imperfect knowledge of tool location) and by the length of the sub-array. Furthermore, processing waveforms with a subset of receivers decreases signal-to-noise ratio and may yield spurious estimations of slownesses (Thompson and Burns, 1989).

To account for the presence of heterogeneities and thin beds in the interpretation of sonic logs, Huang et al. (2015) introduced 1D axial sensitivity functions to fast-forward model compressional, shear, flexural, and Stoneley logs measured with wireline tools in a vertical borehole. Axial sensitivity functions describe the spatial averaging along the borehole axis introduced on sonic logs by the acoustic tool and depend on the geometrical and physical properties of both borehole and tool. The fast-forward method motivated the development of an inversion-based algorithm that combined shear and compressional logs to estimate layer-by-layer elastic properties of isotropic formations penetrated by vertical wells (Huang and Torres-Verdín, 2016). Inverted layer-by-layer elastic properties exhibit reduced spatial averaging effects; thus, their vertical resolution is greater compared to the vertical resolution of elastic properties obtained with conventional interpretation methods. Furthermore, Huang et al. (2015) constructed 2D axial-radial sensitivity functions to efficiently forward model flexural slownesses of 2D invaded and inter-bedded formations penetrated by vertical wells. They showed that axial-radial sensitivities were accurately obtained from the product of 1D axial and 1D radial sensitivities and successfully implemented them in the calculation of multi-frequency flexural modes of invaded formations. However, for formations logged with LWD instruments, the flexural mode is biased by the existence of tool modes originating

from the tool collar (Sinha et al., 2009). Thus, forward modeling and inversion of other borehole modes are required for the interpretation of LWD acoustic logs.

In recent years, the exploration and production of organic-shale formations that exhibit vertical transverse isotropy have increased; therefore, estimating the stiffness coefficients and petrophysical properties of VTI formations has become necessary for production optimization and reservoir appraisal (King, 2010). Many methods based on effective medium theories have been introduced to calculate elastic properties of rocks such as the self-consistent approximation (SCA) (Hill, 1965; Wu, 1966) or the differential effective medium (DEM) (Hornby et al., 1994). However, these methods can provide non-unique solutions of elastic properties (Fjar et al., 2008), they often require calibrations to core data (Suarez-Rivera and Bratton, 2009; Murphy et al., 2015; Yan et al., 2016), and are not always valid in anisotropic formations. Other methods estimate coefficients from tri-axial strength tests on core samples or from ultra-sonic measurements. However, core data analysis is scant and expensive, providing discontinuous estimates over the reservoir interval.

To overcome the aforementioned limitations, sonic log interpretation can be used to estimate dynamic elastic properties of rocks. Walsh et al. (2006, 2007) introduced a method to determine stiffness coefficients of formations using a set of sonic measurements including compressional, fast-shear, slow-shear, and Stoneley logs. The method yields four anisotropic moduli of orthorhombic and transversely-isotropic (TI) formations. Another method was introduced by Sinha et al. (2014, 2016) where multi-frequency flexural slownesses measured with wireline tools were used to extract stiffness coefficients of VTI formations. They calculated the sensitivity (derived from first-order

linear perturbation theory) of the flexural velocity to stiffness coefficients and used the sensitivities at different frequencies to calculate four of the five independent stiffness coefficients. However, this method is not applicable to formations logged with LWD instruments because flexural logs are affected by tool modes (Sinha et al., 2009), which bias the estimation of stiffness coefficients. Therefore, in LWD operations other borehole acoustic modes (e.g., quadrupole mode) need to be considered to estimate stiffness coefficients from logs. Furthermore, because sonic tools introduce spatial averaging effects on logs (Peyret and Torres-Verdín, 2006), calculated coefficients with this method are averaged vertically over the length of the receiver array of wireline tools, which typically varies between 3 ft and 6 ft in length. Therefore, to estimate layer-by-layer stiffness coefficients of formations, acoustic logs need to be corrected for spatial averaging effects.

Undulating wells are routinely drilled to improve reservoir exposure across hydrocarbon-bearing zones. However, conventional methods used to interpret sonic logs acquired in vertical wells penetrating horizontal layers can yield inaccurate results in HA/HZ wells due to azimuthal asymmetry, spatial averaging effects, eccentricity and wave-mode interference (Zheng et al., 2004; Byun and Toksöz, 2006; Ellis and Singer, 2007; Pardo et al., 2013). Furthermore, in VTI formations penetrated by a well that is not aligned with the symmetry axis, slownesses measured with cross dipoles at low frequencies are affected by formation dip (Sinha et al., 1994). Three-dimensional (3D) finite-difference and finite-element methods were implemented to study the effects of dipping beds (Liu et al., 1996) and anisotropy on measured slownesses in HA/HZ wells (Wang et al., 2002); however, these are extremely CPU-time and memory demanding in

formations with multiple layers. Therefore, the challenge remains to develop a fast-forward model to calculate flexural slownesses of isotropic and VTI formations penetrated by high-angle wells.

1.2 RESEARCH OBJECTIVES

The main objective of this dissertation is to develop fast-forward modeling and inversion methods for quantitative interpretation of borehole acoustic logs acquired in isotropic and VTI formations. Detailed objectives of this dissertation are as follows:

- To develop fast-forward modeling of borehole sonic modes in isotropic and VTI formations penetrated by a vertical well and a wireline or LWD instrument. Forward modeling is achieved by invoking spatial sensitivity functions which are calculated from frequency-domain linear perturbation theory.
- To decouple the effects of the spatial averaging introduced by acoustic tools and the intrinsic properties of layers on measured logs.
- To develop a physics-based method to mitigate averaging effects and borehole environmental noise on sonic logs. To achieve this objective, inversion techniques and a 1D forward model are implemented to estimate slownesses of layered formations.
- To verify the accuracy and efficiency of the noise-mitigation method with synthetic formations that include thin layers and high-amplitude noise.
- To apply the noise-mitigation method to hydrocarbon reservoirs and improve the assessment of angle reflectivity from sonic logs.

- To study the impact of layer thickness and position of bed boundaries on inversion-based results, and improve slowness estimations using subarray processing of acoustic logs.
- To develop inversion-based algorithms for the estimation of stiffness coefficients of VTI layers from multi-frequency compressional, Stoneley, flexural/quadrupole logs.
- To estimate layer-by-layer shear slownesses of formations in LWD applications.
- To quantify the error of estimating stiffness coefficients from acoustic logs.
- To develop a fast-forward model to calculate flexural logs of isotropic and VTI formations penetrated by high-angle wells using three-dimensional (3D) spatial sensitivity functions.
- To describe effective and apparent anisotropy of formations penetrated by high-angle wells from cross-dipole measurements.

1.3 METHOD OVERVIEW

In the first part of this dissertation, I introduce a new method for accurate fast-forward simulation of wireline and LWD borehole measurements in formations with horizontal layers penetrated by vertical wells. The method invokes axial sensitivity functions calculated using ray theory across the receivers of an acoustic tool.

A physics-based interpretation method is then developed to reduce noise and spatial averaging effects on sonic logs in formations with horizontal layers penetrated by vertical wells. Unlike current methods that mitigate noise on sonic logs by applying numerical filters directly to sonic measurements, the physics-based inversion method takes into account the physical properties of tool, formation, and wave propagation. Bed

boundaries, initial estimates of layer-by-layer slownesses, and tool and borehole geometry and elastic properties are inputs to the physics-based interpretation method. Accordingly, first I construct a multi-layer earth model of unknown slownesses where I determine the location of bed boundaries from gamma ray (GR), bulk density (ρ), or sonic logs. Next, I jointly invert shear and compressional logs to estimate layer-by-layer slownesses of the earth model and use the calculated slownesses to model sonic logs with mitigated measurement noise. The inversion minimizes a quadratic cost function with second-order regularization. Initial estimates of slownesses are calculated from the mean value of shear and compressional logs within each layer. Field and synthetic examples are used to validate the method. I show that slight variations in bed-boundary locations do not significantly modify the noise-mitigated logs. Furthermore, applying the method with bed boundaries uniformly spaced at the log sampling interval yields similar logs to those calculated when bed boundaries are known. For a formation with very thin layers, the inversion is applied to logs obtained by processing a subset of receivers. Accuracy of inversion results is verified using a 2D *hp*-adaptive finite-element algorithm (Matuszyk et al., 2013) and a 2D finite-difference numerical method.

The second part of this dissertation introduces an inversion-based interpretation method of wireline and LWD multi-frequency borehole acoustic measurements acquired in VTI formations penetrated by vertical wells. The inversion method is performed in two steps: (1) reduction of spatial averaging effects on multi-frequency flexural/quadrupole, Stoneley, and compressional logs, and (2) estimation of layer-by-layer stiffness coefficients of formations. To take advantage of the different sensitivities of borehole modes to stiffness coefficients, the inversion is performed sequentially: First, I invert the

compressional log and the low-frequency Stoneley log to calculate c_{33} and c_{66}, respectively. Then, I invert the quadrupole/flexural log at low frequencies to calculate c_{44}, and finally I invert the quadrupole/flexural logs at high frequencies to calculate c_{11} and c_{13}.

The sequential inversion implements a nonlinear minimization of a quadratic error cost function between the data (acoustic logs) and modeled slownesses within each layer. Numerical entries of the Jacobian matrix are constructed from one-dimensional real-axis integration simulations (Tang and Cheng, 2004). Stability and accuracy of estimated slownesses and stiffness coefficients are quantified using error propagation and first-order approximations. It was found that estimated slownesses and stiffness coefficients from the inversion method are more accurate than the ones obtained from conventional methods.

In the final part of the dissertation, I implement 3D fast-forward modeling to calculate flexural logs measured with orthogonal dipoles in high-angle wells. The forward model invokes 3D spatial sensitivity functions that are obtained from the product of 1D axial, radial, and azimuthal sensitivities. The forward model is the superposition of a reference background slowness and the convolution of a 3D spatial sensitivity function with layer-by-layer model of elastic properties. In VTI formations, the layers are modeled as equivalent-isotropic layers with apparent shear and compressional slownesses (Miller et al., 2012). The fast-forward modeling method is applied to synthetic examples and is verified using a three-dimensional time-domain finite difference (3D-TDFD) method.

1.4 OUTLINE OF THE DISSERTATION

The objectives are achieved in the four chapters that follow Chapter 1. A final chapter describes the conclusions and recommendations of this research work.

In Chapter 2, I introduce spatial sensitivity functions that are derived from frequency-domain linear perturbation theory of borehole acoustic modes. I show that axial sensitivity functions decouple the dependence of measured slowness on elastic properties and the spatial averaging introduced by acoustic tools on logs. Next, radial sensitivity functions are calculated to determine the radial depth of investigation of quadrupole and flexural modes. Finally, I describe the fast-forward modeling method used to calculate acoustic logs.

In Chapter 3, I develop a physics-based method to reduce noise and spatial averaging on acoustic logs acquired in horizontally layered formations penetrated by vertical wells. First, the method is validated using synthetic examples with noisy shear and compressional logs; synthetic examples include thinly-bedded formations with large contrast of elastic properties between adjacent layers. Next, the method is applied to mitigate measurement noise in two hydrocarbon reservoirs and improve estimations of angle reflectivity from sonic logs.

In Chapter 4, I introduce a sequential inversion to estimate stiffness coefficients of VTI formation penetrated by vertical wells from multi-frequency flexural/quadrupole, Stoneley, and compressional logs. Spatial averaging effects of frequency-dependent slownesses are mitigated prior to inversion. I apply the method to synthetic formations logged with wireline and LWD instruments and quantify the bias and uncertainty of estimated coefficients using first-order approximations.

In Chapter 5, I extend the forward modeling method to calculate slownesses of formations penetrated by a high-angle well. Several synthetic examples with varying dip, number of layers, formation type, and elastic properties are included to validate the method. Accordingly, I calculate flexural slownesses of isotropic and VTI formations obtained using orthogonal-dipole sources and verify the accuracy of the results using 3D-TDFD numerical simulations.

In Chapter 6, I summarize the conclusions of the research findings, and I give recommendations for potential future work.

1.5 LIST OF PUBLICATIONS

Based on the research work in the dissertation, the following is a list of journal and conference papers published or submitted for review.

1.5.1 Refereed Journal Publications

Maalouf E. and C. Torres-Verdín, 2017, Inversion-based method to mitigate noise in borehole sonic logs (*Manuscript accepted for publication)*.

Maalouf E. and C. Torres-Verdín, 2017, Interpretation of borehole sonic measurements acquired in VTI formations penetrated by vertical wells (*Manuscript submitted for review*).

Maalouf E. and C. Torres-Verdín, 2017, Interpretation of borehole acoustic dipole modes in high-angle wells using spatial sensitivity functions (*Manuscript to be submitted for review*).

1.5.2 Refereed Conference Proceedings

Maalouf E. and C. Torres-Verdín, 2016, New physics-based method to efficiently mitigate noise in borehole sonic logs: 86th Annual International Meeting, SEG, Expanded Abstracts, 627–631, Dallas, Texas, October, 16-21.

Maalouf E. and C. Torres-Verdín, 2017, Interpretation of sonic measurements acquired in high-angle and horizontal wells using 3D fast forward modeling: Presented at the SPWLA 58th Annual Logging Symposium, Oklahoma City, OK, June, 17-21.

Maalouf E. and C. Torres-Verdín, 2017, Estimation of rock stiffness coefficients in VTI formations using LWD acoustic measurements: Presented at the SPWLA 58th Annual Logging Symposium, Oklahoma City, OK, June, 17-21.

Chapter 2: Spatial Sensitivity Functions of Borehole Acoustic Measurements

In this chapter, I introduce the spatial sensitivity functions of borehole guided waves that are constructed using first-order perturbation theory and that quantify the influence of elastic properties on wave propagation. First, I calculate the sensitivity of flexural and quadrupole modes in isotropic formations logged with wireline and LWD instruments, respectively. Then, I introduce a new method to compute axial sensitivity functions in layered formations (formations with thin horizontal beds penetrated by a vertical borehole); the axial sensitivity functions represent the averaging introduced by acoustic tools on logs. Finally, I calculate the radial and the axial-radial sensitivity functions that quantify the length of investigation of borehole acoustic modes. Additionally, I describe how to use the spatial sensitivity functions to calculate sonic logs in homogeneous and heterogeneous formations penetrated by a borehole and an acoustic tool.

2.1 SENSITIVITY FUNCTIONS

Three elastic parameters describe the elastic behavior of isotropic formations, namely, shear slowness (ss), compressional slowness (sp), and density (ρ) that influence the wave propagation of guided modes (e.g., flexural and quadrupole modes). I use sensitivity functions to quantify the influence of each elastic parameter on wave phase-slowness. In a homogeneous formation with a vector of elastic properties $\mathbf{p_0} = [ss, sp, \text{and } \rho]$, the sensitivity $S_k^{\{l\}}$ of a sonic borehole mode $\{l\}$ to the elastic property p_{0k} is defined by

$$S_k^{\{l\}}(\mathbf{p_0}, f) = \frac{\partial s^{\{l\}}(\mathbf{p_0}, f)}{\partial p_{0k}}, \tag{2.1}$$

where s is mode slowness at frequency f measured by an acoustic tool of a homogeneous formation whose elastic properties are given by the vector $\mathbf{p_0}$, and p_{0k} is the k-th elastic property. Figure 2.1 and Figure 2.2 show the normalized sensitivity of the quadrupole and flexural modes calculated in slow and fast homogenous formations penetrated by LWD and wireline tools, respectively. The normalization factor is $s^{\{l\}}(\mathbf{p_0}, f)/p_{0k}$. Formation and borehole properties are given in Table 1, while the tool properties are given in Table 2. In subsequent sections, $\{l\}$ is equal to $\{q\}$ for quadrupole, $\{fl\}$ for flexural, $\{c\}$ for compressional, and $\{st\}$ for Stoneley modes. The sensitivities of the flexural and quadrupole modes to shear slowness are the largest at all frequencies, while the sensitivity to compressional slowness is small at low frequencies and increases at higher frequencies. The sensitivity of the flexural mode to density is the smallest, being one order of magnitude smaller than the previous ones.

As a first-order approximation, the slowness $s^{\{l\}}(\mathbf{p}, f)$ of a homogeneous formation of elastic property $\mathbf{p}$, is expressed as

$$s^{\{l\}}(\mathbf{p}, f) = s^{\{l\}}(\mathbf{p_0}, f) + \sum_k (p_k - p_{0k}) S_k^{\{l\}}(\mathbf{p_0}, f)\,, \tag{2.2}$$

where $(p_k - p_{0k})/p_{0k} \ll 1$.

2.2 AXIAL SENSITIVITY FUNCTIONS

In layered formations (formations with thin horizontal beds penetrated by a vertical borehole), the slowness measured by sonic tools is averaged over several layers.

Therefore, I construct axial sensitivity functions to quantify spatial averaging effects introduced by acoustic instruments on logs and forward-model slownesses of thinly-bedded formations.

2.2.1 Calculation of Axial Sensitivity Functions

In a layered formation, the slowness of a sonic mode $\{l\}$ measured by an acoustic tool is averaged along the borehole axis. The spatially averaged slowness $\bar{s}^{\{l\}}(d,f)$ of a sonic mode $\{l\}$ at frequency f measured by the tool at depth d is given by

$$\bar{s}^{\{l\}}(d,f) = \sum_{i=1}^{N} F(z_i - d)s^{\{l\}}(\mathbf{p}(z_i),f) + O(s^2), \tag{2.3}$$

where $s^{\{l\}}(\mathbf{p}(z_i),f)$ is slowness of the formation of elastic properties $\mathbf{p}$ at depth z_i, that is midway between receivers i and i +1, N is total number of receivers, and F is an averaging function that depends on the tool *geometrical* properties. Assuming higher-order terms contributing to the spatially averaged slowness are negligible, substitution of equation 2.2 into equation 2.3 yields

$$\bar{s}^{\{l\}}(d,f) = \bar{s}_0^{\{l\}}(d,f) + \sum_{i=1}^{N}\sum_{k} F(z_i - d)S_k^{\{l\}}(\mathbf{p_0}(z_i),f)(p_k(z_i) - p_{0k}(z_i)), \tag{2.4}$$

where $\{l\}$ denotes the sonic mode, $\bar{s}_0^{\{l\}}(d,f)$ is the average slowness of the reference homogeneous backgrounds between the first and the N-th receiver of the acoustic tool, $z_i = d + L/2 - (i - 1/2)L/(N-1)$, L is the length of the receiver array, and $p_k(z_i)$ is the value of rock property p_k at depth z_i. Therefore, to calculate sonic logs, the effects of

the spatial averaging on logs (given by F) and of the sensitivity of a borehole mode to elastic properties (given by $S^{\{l\}}$) can be decoupled.

Equation 2.4 is similar to the forward model proposed by Huang et al. (Huang et al., 2015) to calculate sonic logs in horizontally layered formations penetrated by vertical wells given by

$$\bar{s}^{\{l\}}(d,f) = s^{\{l\}}(\mathbf{p_0},d,f) + \sum_z \sum_k \frac{p_k(z) - p_{0k}(d)}{p_{0k}(d)} G^{\{l\}}(p_{0k},z,f)\, s^{\{l\}}(\mathbf{p_0},d,f), \qquad 2.5$$

where $G^{\{l\}}(p_{0k},z,f)$ is the normalized axial sensitivity function of the sonic mode $\{l\}$ to elastic property p_{0k} and is given by

$$G^{\{l\}}(p_{0k},z,f) = \frac{(s^{\{l\}}(z,f) - s^{\{l\}}(\mathbf{p_0},f))/s^{\{l\}}(\mathbf{p_0},f)}{(p_k - p_{0k})/p_{0k}}, \qquad 2.6$$

where $s^{\{l\}}(\mathbf{p_0},f)$ is the slowness of a homogeneous reference background of elastic properties $\mathbf{p_0}$ and $s^{\{l\}}(z,f)$ is the slowness measured by the sonic tool when a horizontal layer (layer *Y*) of elastic property $p_k \neq p_{0k}$ and thickness Δz_L is inserted at depth z between two consecutive receivers of the sonic tool that penetrates the reference homogeneous formation. To avoid time consuming numerical simulations to calculate $s^{\{l\}}(z,f)$, a semi-analytical method can be used to obtain $G^{\{l\}}$; a detailed explanation on the semi-analytical method is given in Section 2.2.2.

By comparing equations 2.4 and 2.5 I conclude that

$$G^{\{l\}}(p_{0k},z,f)\frac{p_{0k}(z)}{s^{\{l\}}(\mathbf{p_0},f)} = F(z)S_k^{\{l\}}(\mathbf{p_0}(z),f). \qquad 2.7$$

Furthermore, S depends on the borehole fluid, tool elastic properties, sonic mode, frequency, and elastic parameters, and is given by equation 2.1, while F is an analytical expression that depends on the tool *geometrical* properties and can be calculated using ray theory. Maalouf and Torres-Verdín (2017) showed that

$$F(z_i) = \frac{s(z_i) - s_r}{s_p - s_r}, \tag{2.8}$$

where s_r is slowness of a reference homogeneous formation and $s(z)$ is slowness measured by the sonic tool when a layer (layer *Y*) of slowness s_p and thickness Δz_L is inserted, centered at depth z_i, between two consecutive receivers i and $i+1$ of the sonic tool. The slowness, $s(z)$, measured by the N receivers of the tool when the center of the receiver array is at z is given by

$$s(z) = \frac{T}{D_T}, \tag{2.9}$$

where D_T is total distance traveled by the wave and T is total travel time. Total travel time is calculated by adding the travel time it takes the borehole wave to propagate from one receiver to the other, for all possible combinations of receiver pairs. The wave travels from lower receivers to top receivers and the total number of receiver pair combinations is

$$\binom{N}{2} = \frac{N(N+1)}{2}. \tag{2.10}$$

Total travel time is given by

$$T = \sum_{i=1}^{N-1} \sum_{j=i+1}^{N} t_{ij}, \tag{2.11}$$

where $t_{ij} = (j - i - 1)s_r\Delta z_R + s_p\Delta z_R$ if $i \leq k < j$, and $t_{ij} = (j - i)s_r\Delta z_R$ otherwise, when layer *Y* is centered at depth z_k. Therefore

$$T = \frac{1}{6}\Delta z_R\, s_r N(N^2 - 1) + \left(s_p - s_r\right)\Delta z_R k(N - k), \tag{2.12}$$

while the total distance traveled by the wave is

$$D = \sum_{i=1}^{N-1}\sum_{j=i+1}^{N}(j - i)\Delta z_R = \frac{1}{6}\Delta z_R\, N(N^2 - 1). \tag{2.13}$$

By combining equations 2.12, 2.13, and 2.9 I obtain

$$s(z_i) = \frac{\frac{1}{6}\Delta z_R\, s_r N(N^2 - 1) + \left(s_p - s_r\right)\Delta z_R i(N - i)}{\frac{1}{6}\Delta z_R\, N(N^2 - 1)}. \tag{2.14}$$

Substitution of equation 2.14 in equation 2.8 yields an analytical expression of the spatial averaging function F given by

$$F(z_i) = \begin{cases} \dfrac{6i(N - i)}{N(N^2 - 1)} & \text{for } z_i \text{ between receivers } i \text{ and } i\text{+1}, \\ 0 & \text{for } z_i \text{ outside the receiver array,} \end{cases} \tag{2.15}$$

where $i = [1 \ldots (N - 1)]$. Figure 2.3 shows $F(z_i)$ for the LWD and wireline tools given in Table 2 while Figure 2.4 shows the geometry and the position of the receivers. I show in Section 2.2.2 that the difference between G (equation 2.6) and the product $F(z)S_k^{\{l\}}(\mathbf{p}_0(z), f)$ is less than 1%, which confirms that second order-terms in equation 2.3 are negligible.

By substituting equations 2.15 into equation 2.3, I obtain the forward model of sonic logs in a layered formation penetrated by a vertical well, given by

$$\bar{s}^{\{l\}}(d,f) = \sum_{i=1}^{N} \frac{6i(N-i)}{N(N^2-1)} s^{\{l\}}(\mathbf{p}(z_i),f), \tag{2.16}$$

where $s^{\{l\}}(\mathbf{p}(z_i),f)$ is the slowness of mode $\{l\}$ at frequency f of the homogeneous formation with elastic properties $\mathbf{p}$ at depth $z_i = d + L/2 - (i-1/2)\ L/(N-1)$, N is total number of receivers, and $s^{\{l\}}$ is calculated using one-dimensional (1D) simulations of borehole modes (Tang and Cheng, 2004).

2.2.2 Semi-Analytical Axial Sensitivity Functions

Huang et al. (2015) showed that the normalized frequency-domain axial sensitivity function of a sonic mode $\{l\}$ at frequency f of a homogeneous formation of elastic properties $\mathbf{p_0}$ to perturbations of elastic property p_{0k} is given by

$$G^{\{l\}}(p_{0k},z,f) = \frac{(s^{\{l\}}(z,f) - s^{\{l\}}(\mathbf{p_0},f))/s^{\{l\}}(\mathbf{p_0},f)}{(p_k - p_{0k})/p_{0k}}, \tag{2.17}$$

where $s^{\{l\}}(\mathbf{p_0},f)$ is the slowness of a homogeneous reference background of elastic properties $\mathbf{p_0}$, and $s^{\{l\}}(z,f)$ is the slowness measured by the sonic tool when a horizontal layer (layer *Y*) of elastic property $p_k \neq p_{0k}$ and thickness Δz_L is inserted at depth z between two consecutive receivers of the sonic tool that penetrates the reference homogeneous formation. Layer *Y* is shifted in the vertical direction (z-axis) across the receiver array of the tool to calculate $G^{\{l\}}$ at every position z. At every position of layer *Y*, I calculate the spectrum of the wave mode $\{l\}$ registered by the receivers of the tool

and process the spectrum to obtain the slowness $s^{\{l\}}(z, f)$. In what follows, I show how to calculate the spectrum analytically, in a three-layer 1D medium, using boundary conditions of displacement and stress at the boundaries of layer *Y*. Assume a homogeneous formation of elastic property $\mathbf{p_0}$ where a layer (layer *Y*) of thickness Δz_L and elastic property $\mathbf{p}$ such that $\mathbf{p} = \mathbf{p_0} + \Delta\mathbf{p}$ is inserted. This divides the medium in three regions: region *I* has elastic property $\mathbf{p_0}$ and contains an incident and reflected wave with complex amplitudes A and B, respectively; region *II* has thickness Δz_L with elastic property $\mathbf{p}$ and transmitted and reflected waves with complex amplitudes C and D, respectively; and region *III* has elastic property $\mathbf{p_0}$ and contains only a transmitted wave with complex amplitude E. The upper and lower location of the boundaries of layer *Y* are z_u and z_l, respectively, as shown in Figure 2.5.

Using Lamé's (Aki and Richards, 2002) theorem, I express the displacement field u as $u = \frac{\partial \phi}{\partial z}$, where ϕ is the scalar wave potential. Because u satisfies the wave equation, ϕ satisfies the Helmholtz equation whose solution in regions *I*, *II*, and *III* are given by

$$\phi_I(z) = Ae^{-ik_I z} + Be^{ik_I z}, \tag{2.18}$$

$$\phi_{II}(z) = Ce^{-ik_{II} z} + De^{ik_{II} z}, \tag{2.19}$$

$$\phi_{III}(z) = Ee^{-ik_{III} z}, \tag{2.20}$$

where k_i is the wavenumber of layer i. At region boundaries z_l and z_u, the displacement u and stress σ must be continuous. They are given by

$$u(z) = \frac{\partial \phi}{\partial z}, \tag{2.21}$$

$$\sigma(z) = \lambda \frac{\partial u}{\partial z}, \tag{2.22}$$

where $\lambda = \rho c^2$ with ρ and c the density and velocity of the wave mode of the layer. Therefore, at z_l

$$-ik_I A e^{-ik_I z_l} + ik_I B e^{ik_I z_l} + ik_{II} C e^{-ik_{II} z_l} - ik_{II} D e^{ik_{II} z_l} = 0, \quad 2.23$$

$$\lambda_I\left(-k_I^2 A e^{-ik_I z_l} - k_I^2 B e^{ik_I z_l}\right) - \lambda_{II}(-k_{II}^2 C e^{-ik_{II} z_l} - k_{II}^2 D e^{ik_{II} z_l}) = 0, \quad 2.24$$

and at z_u

$$-ik_{II} C e^{-ik_{II} z_u} + ik_{II} D e^{ik_{II} z_u} + ik_{III} E e^{-ik_3 z_u} = 0, \quad 2.25$$

$$\lambda_{II}\left(-k_{II}^2 C e^{-ik_{II} z_u} - k_{II}^2 D e^{ik_{II} z_u}\right) - \lambda_{III}(-k_{III}^2 E e^{-ik_{III} z_u}) = 0, \quad 2.26$$

where k_i is the wavenumber of region i. In this example $k_I = k_{III} = k_r$ and $k_{II} = k_p$. I assume that A (the incident amplitude) is known and calculate the four unknowns B, C, D, and E by solving the following system of equations

$$\begin{bmatrix} k_r e^{ik_r z_l} & k_p e^{-ik_p z_l} & -k_p e^{ik_p z_l} & 0 \\ -\lambda_r k_r^2 e^{ik_r z_l} & \lambda_p k_p^2 e^{-ik_p z_l} & \lambda_p k_p^2 e^{ik_p z_l} & 0 \\ 0 & -k_p e^{-ik_p z_u} & k_p e^{ik_p z_u} & k_r e^{-ik_r z_u} \\ 0 & -\lambda_p k_p^2 e^{-ik_p z_u} & -\lambda_p k_p^2 e^{ik_p z_u} & \lambda_r k_r^2 e^{-ik_r z_u} \end{bmatrix} \begin{bmatrix} B \\ C \\ D \\ E \end{bmatrix} = \begin{bmatrix} A k_r e^{-ik_r z_l} \\ A\lambda_r k_r^2 e^{-ik_r z_l} \\ 0 \\ 0 \end{bmatrix}, \quad 2.27$$

to obtain

$$B = \frac{A e^{-2ik_r z_l}(e^{2ik_p z_l} - e^{2ik_p z_u})(k_r^2 - k_p^2)}{e^{2ik_p z_l}(k_r - k_p)^2 - e^{2ik_p z_u}(k_r + k_p)^2}, \quad 2.28$$

$$C = \frac{iAe^{-i(k_r z_l - k_p z_u)} k_r (k_r + k_p)}{2ik_r k_p \cos[k_p(z_l - z_u)] + (k_r^2 + k_p^2)\sin[k_p(z_l - z_u)]}, \quad 2.29$$

$$D = \frac{2Ae^{-i(k_r - k_p)z_l} k_r (k_r - k_p)}{e^{2ik_p z_l}(k_r - k_p)^2 - e^{2ik_p z_u}(k_r + k_p)^2}, \quad 2.30$$

$$E = \frac{2iAe^{-ik(z_l - z_u)} k_r k_p}{2ik_r k_p \cos[k_r(z_l - z_u)] + (k_r^2 + k_p^2)\sin[k_p(z_l - z_u)]}. \quad 2.31$$

Therefore, when layer Y is between receivers j and $j+1$, the spectrum X_i at each receiver i can be written as

$$\left[X_1(f), \ldots, X_j(f), X_{j+1}(f), X_{j+2}(f), \ldots, X_N(f)\right] = [A, AZ + BZ^*, \ldots, AZ^{(j-1)} + BZ^{*(j-1)}, Ce^{-ik_p j \Delta z_L} + De^{ik_p j \Delta z_L}, EZ^{(j+1)} \ldots, EZ^{(N-1)}], \quad 2.32$$

where $Z = e^{-ik_r \Delta z_L}$ and Z^* is the complex conjugate of Z.

Huang et al. (2015) ignore the reflections given by B and D, because in the limits of perturbation theory $|k_r - k_p|/k_r \ll 1$, therefore, $|B| \ll 1$ and $|D| \ll 1$. Another method to remove the interference causes by the reflections without imposing $|B| = 0$ is to calculate the axial sensitivity functions using an antireflective layer by taking $\Delta z_L = \pi n / k_p$, where n is an integer (see equation 2.28).

In Figure 2.5 and Figure 2.6, I compare $G^{\{l\}}/\Delta z_L$ to the product $FS^{\{l\}}/\Delta z_L$ normalized by $s^{\{l\}}(\mathbf{p_0}, f)/\mathbf{p_0}$ calculated with LWD and wireline tools, respectively, where Δz_L is the thickness of the layer used to construct the axial sensitivity functions. The sensitivity using both methods agrees within a relative difference of 1%. The advantages of calculating the axial sensitivity function using the product $FS^{\{l\}}$ are, (1) it is more efficient because it does not require processing the frequency spectrum (equation 2.32) for every position z of layer Y, and (2), it decouples the effects of the geometry of

the tool and of the intrinsic elastic properties of formations on the measured acoustic logs.

2.3 RADIAL SENSITIVITY FUNCTIONS

Radial sensitivity functions quantify the relative variation of phase slowness of a modal wave originating from local perturbations of rock properties in the radial direction (i.e., the radial direction, r, away from the borehole axis).

The radial sensitivity $R_k^{\{l\}}$ of a sonic mode $\{l\}$ to perturbation of elastic property p_{0k} is given by

$$R_k^{\{l\}}(\mathbf{p_0}, r, f) = \frac{s(\mathbf{p}, r, f) - s(\mathbf{p_0}, f)}{(p_k - p_{0k})}, \tag{2.33}$$

where $s(\mathbf{p_0}, f)$ is mode slowness at frequency f of a homogeneous formation whose stiffness coefficients are given by the vector $\mathbf{p_0}$, $s(\mathbf{p}, r, f)$ is the slowness measured by the receiver array when a cylindrical shell L of radius r, thickness Δr, and elastic property $\mathbf{p} \neq \mathbf{p_0}$, is inserted concentric to the borehole. To calculate $R_k^{\{l\}}$ for all positions r, I vary the radius of the cylindrical shell L.

Figure 2.8 and Figure 2.9 show the radial sensitivity of the quadrupole and flexural modes to perturbations of shear slowness, compressional slowness, and density in slow and fast homogeneous formations logged with an LWD and a wireline instrument, respectively. The radial sensitivity functions show that the length of investigation of both the quadrupole and flexural modes to perturbations of shear slowness varies between 0.3 m and 1 m. The length of investigation depends on frequency and formation type (i.e., slow, intermediate, and fast); faster formations have

extended length of investigations. Furthermore, quadrupole and flexural modes are less sensitive to perturbations of compressional slowness and density compared to perturbations of shear slowness.

2.4 AXIAL-RADIAL SENSITIVITY FUNCTIONS

Axial-radial sensitivity functions can be approximated by the product of 1D axial and 1D radial sensitivity functions (Huang et al., 2015). In Section 2.2, I showed that the axial sensitivity function could be expressed as the product FS, where F is the spatial averaging introduced by the sonic tool in the axial direction, and S is the sensitivity of a borehole mode in a homogeneous formation. Similarly, the axial-radial sensitivity function ${G_{rz}}_k^{\{l\}}$ of a borehole mode $\{l\}$ to perturbations of elastic property p_k can be expressed as

$$ {G_{rz}}_k^{\{l\}}(\mathbf{p_0}, r, z, f) = F(z) R_k^{\{l\}}(\mathbf{p_0}, r, f), \tag{2.34} $$

where F and $R_k^{\{l\}}(\mathbf{p_0}, r, f)$ are obtained from equations 2.15 and 2.33, respectively, and r and z are radial and axial distances, respectively.

Figure 2.10 and Figure 2.11 show the axial-radial sensitivity of the quadrupole mode to perturbation of shear slowness in slow and fast formations, respectively, while Figure 2.12 and Figure 2.13 show the axial-radial sensitivity of the flexural mode to perturbation of shear slowness in slow and fast formations, respectively.

2.5 SUMMARY AND CONCLUSIONS

In this chapter, I calculated the sensitivity of the dispersive flexural and quadrupole modes to perturbation of shear slowness, compressional slowness, and density in isotropic formations. I showed that flexural and quadrupole modes are mostly

sensitive to shear slowness at low frequencies, and to shear slowness, compressional slowness, and density, at higher frequencies.

I introduced a new method to calculate axial sensitivity functions by decoupling geometrical averaging effects from the intrinsic elastic properties of formations on borehole dispersive modes. The geometrical averaging function (F) depends on the acoustic tool and is derived using ray theory. One-dimensional radial sensitivity functions, $R_k^{\{l\}}(\mathbf{p_0}, r, f)$, of quadrupole and flexural modes were computed in slow and fast formations logged with LWD and wireline tools. The radial length of investigation of flexural and quadrupole modes to elastic parameters depends on the frequency and the formation type (i.e., slow or fast) and varies between 0.3 m and 1 m. I construct the axial-radial sensitivity function using the averaging function $F(z)$ that depends on the tool geometrical properties and the radial sensitivity function $R_k^{\{l\}}(\mathbf{p_0}, r, f)$ that depends on the tool, borehole fluid, and formation properties.

Spatial sensitivity functions quantify the variation of phase slowness measured by the sonic tool due to spatial perturbations of elastic properties. Thus, they can be used to fast-forward model borehole acoustic logs. Fast-forward modeling allows the implementation of new methods to interpret acoustic logs which I investigate in Chapter 3, Chapter 4, and Chapter 5.

2.6 TABLES AND FIGURES

Table 2.1: Summary of the assumed elastic properties of borehole fluid and rock formations in Chapter 2.

	Borehole	**Slow Formation**	**Fast Formation**
$\boldsymbol{\rho}$ **(kg/m^3)**	1000	2500	2500
$\boldsymbol{v_p}$ **(m/s)**	1500	2380	3230
$\boldsymbol{v_s}$ **(m/s)**	0	1400	1900

Table 2.2: Geometric properties assumed for the LWD and wireline instruments in Chapter 2.

	LWD	**Wireline**
Number of receivers	12	13
Inter-receiver spacing (m)	0.1017	0.1524
Inner/outer radius (m)	0.0254/0.0857	NA/0.046

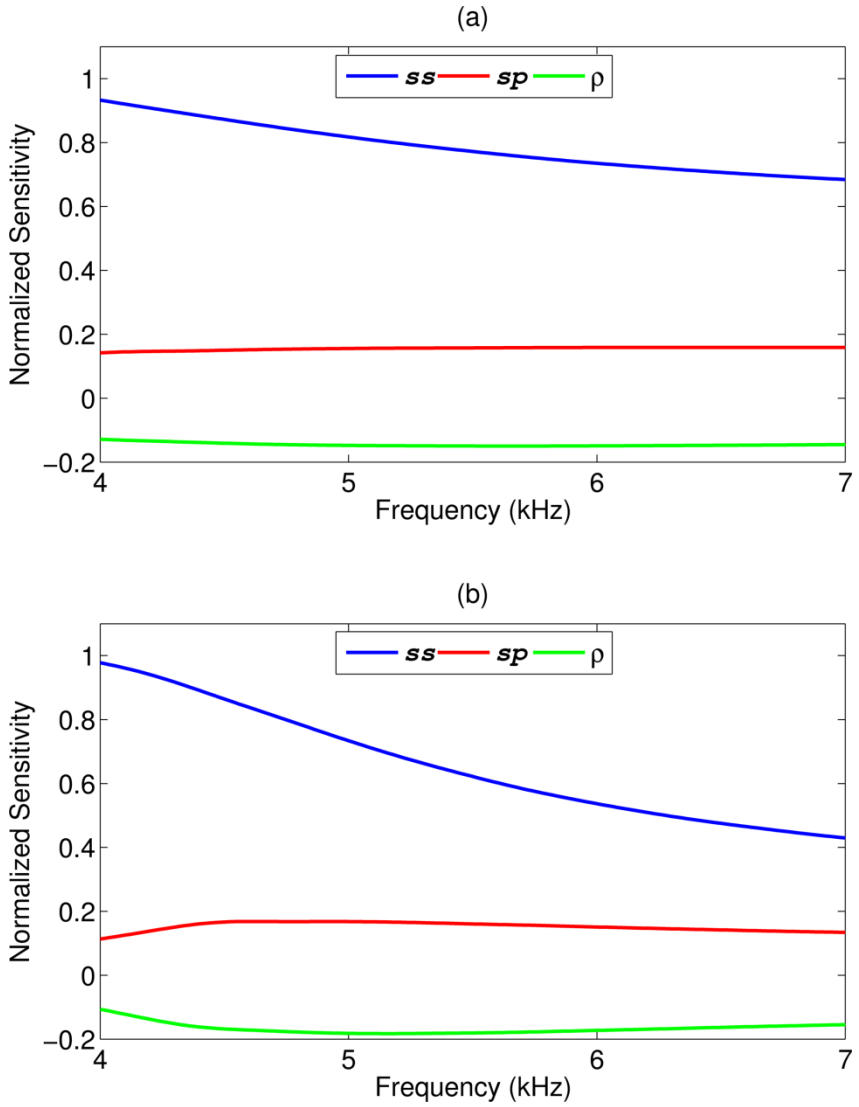

Figure 2.1: Normalized sensitivity of the quadrupole mode to shear slowness (ss), compressional slowness (sp), and formation density (ρ), for the (a) slow and (b) fast formations logged with an LWD instrument.

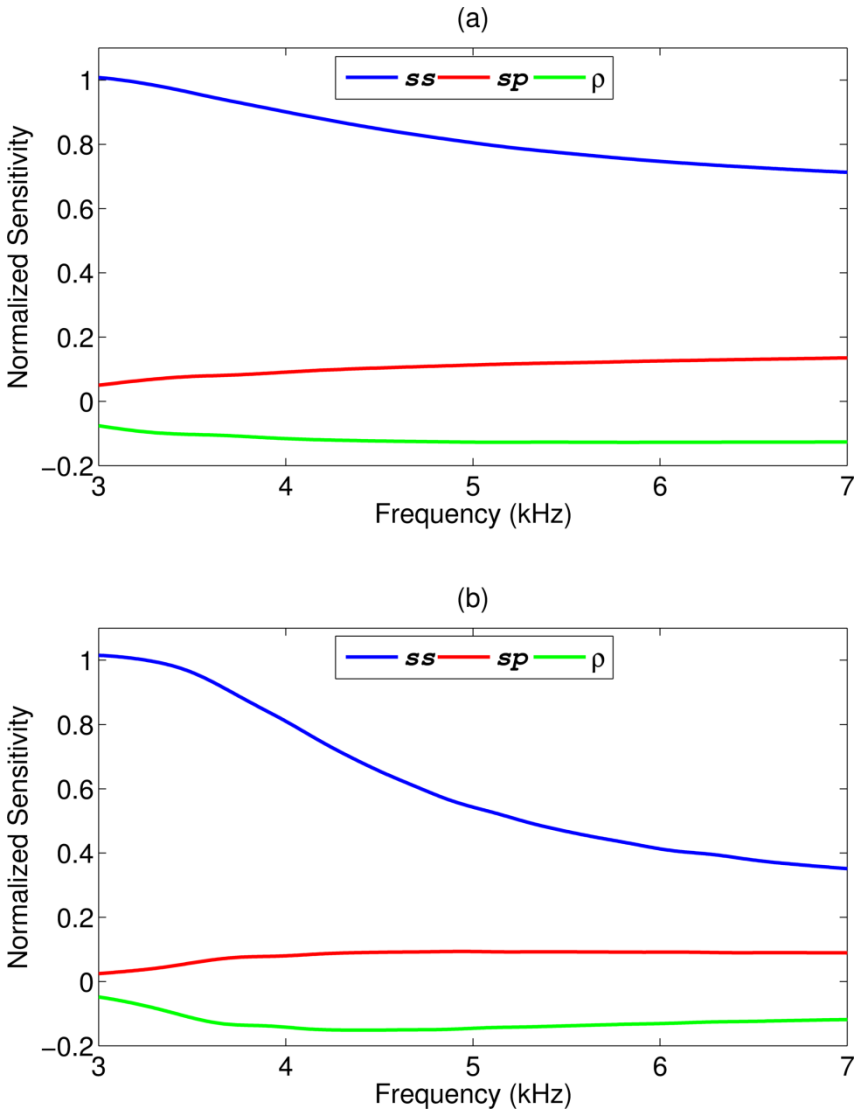

Figure 2.2: Normalized sensitivity of the flexural mode to shear slowness (ss), compressional slowness (sp), and formation density (ρ), for the (a) slow and (b) fast formations logged with a wireline instrument.

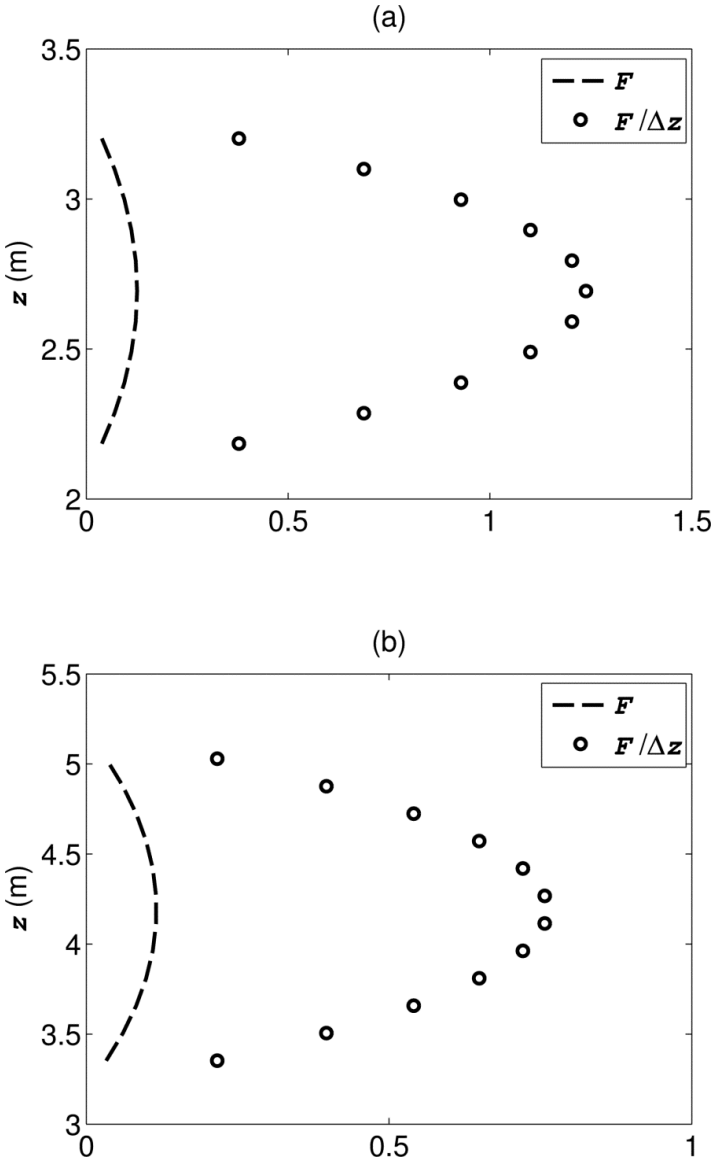

Figure 2.3: Values of the function F (equation 2.15) quantifying the averaging introduced by sonic tools on slownesses measured with the (a) LWD and (b) wireline instruments given in Table 2.2. The circles represent the ratio of F by the inter-receiver distance Δz.

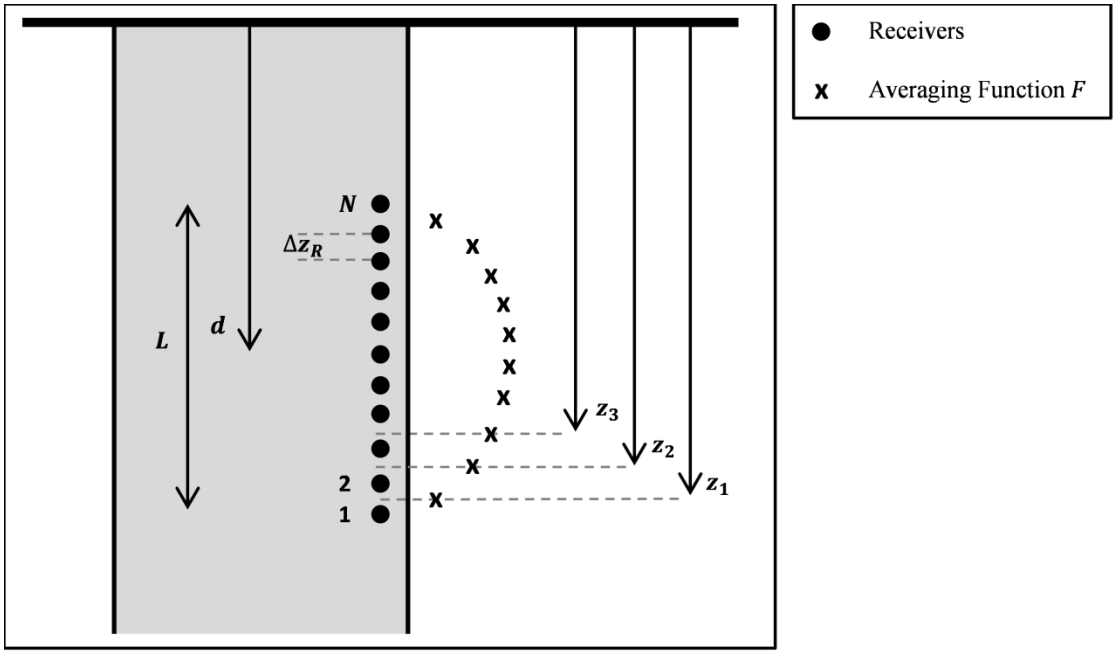

Figure 2.4: Geometry and positions of the receivers (circles) of the acoustic instrument (shown in grey). The total number of receivers is N. The mid-position between receivers i and $i+1$ is z_i; d is the position of the center of the receiver array, and L is the length of the receiver array; Δz_R is the distance between two consecutive receivers. The averaging function F is illustrated with crosses: the sensitivity at position z_i is proportional to the distance between the cross and the receiver array.

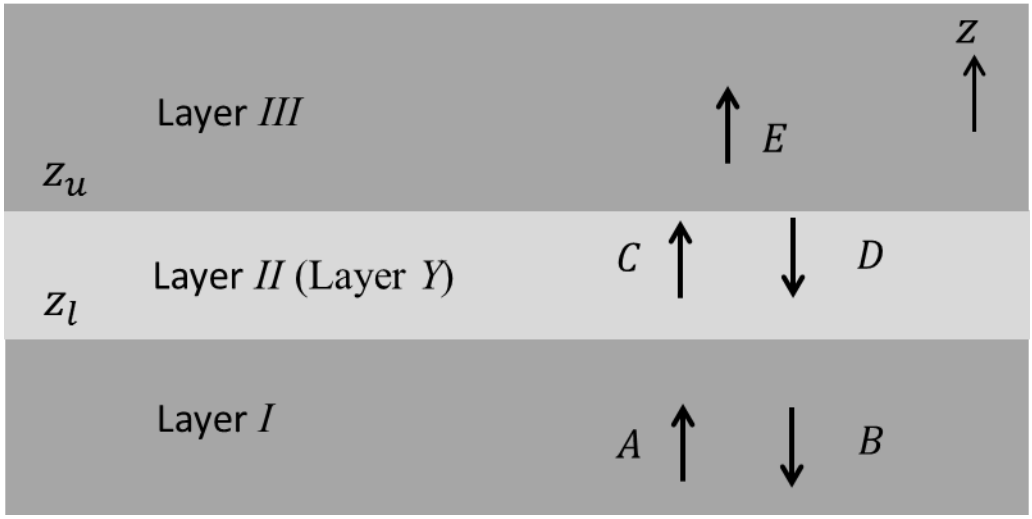

Figure 2.5: Homogeneous formation with an embedded horizontal layer (layer Y) of perturbed elastic properties. Lower and upper boundaries of layer Y are z_l and z_u, respectively. The complex amplitudes of the transmitted waves are A, C, and E, while the complex amplitudes of the reflected waves are B and D.

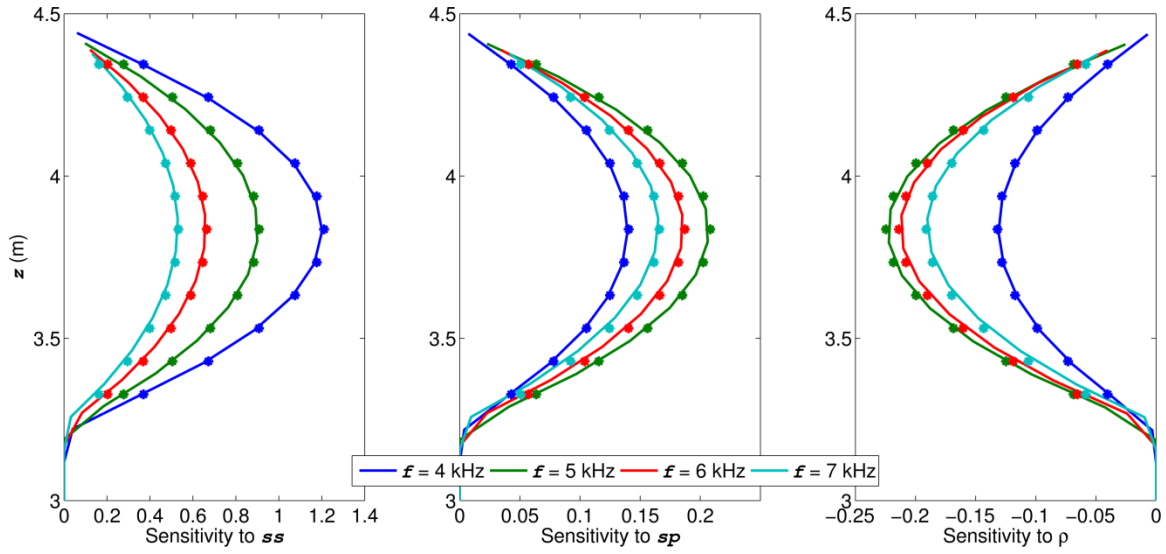

Figure 2.6: Axial sensitivity of the quadrupole mode measured with an LWD instrument at 4 kHz, 5 kHz, 6 kHz, and 7 kHz to perturbations of shear slowness (ss), compressional slowness (sp), and formation density (ρ). The axial sensitivity function G, calculated using equation 2.17 and normalized by the inter-receiver distance, Δz_R , is shown with continuous lines, while the axial sensitivity function calculated using the product of FS normalized by $(s^{\{l\}}(\mathbf{p_0}, f)\Delta z_R)/\mathbf{p_0}$ is shown with circles.

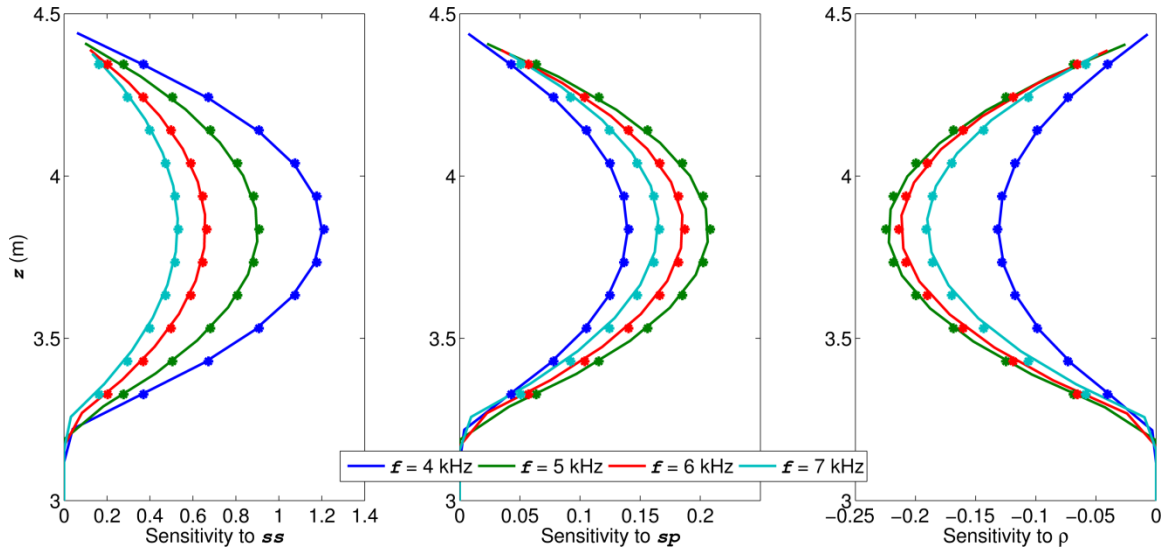

Figure 2.7: Axial sensitivity of the quadrupole mode measured with a wireline tool at 3 kHz, 4 kHz, 5 kHz, 6 kHz, and 7 kHz to perturbations of shear slowness (ss), compressional slowness (sp), and formation density (ρ). The axial sensitivity function G, calculated using equation 2.17 and normalized by the inter-receiver distance, Δz_R , is shown with continuous lines, while the axial sensitivity function calculated using the product of FS normalized by $(s^{\{l\}}(\mathbf{p_0}, f)\Delta z_R)/\mathbf{p_0}$ is shown with circles.

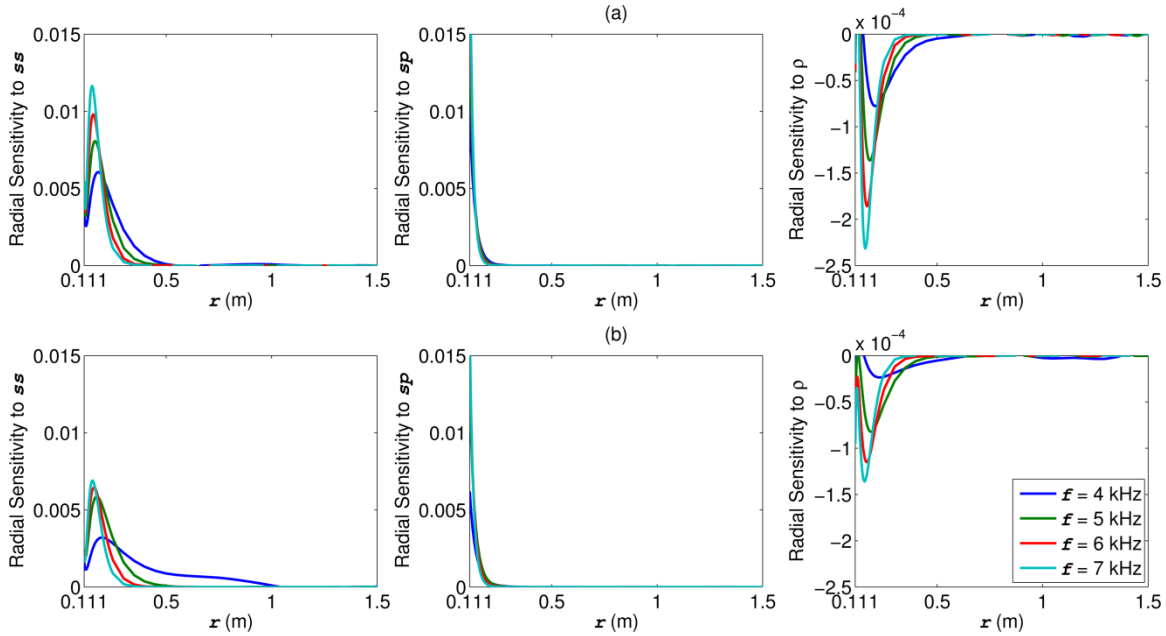

Figure 2.8: Radial sensitivity of the quadrupole mode to perturbations of shear slowness (ss), compressional slowness (sp), and formation density (ρ), measured with an LWD instrument at 4 kHz, 5 kHz, 6 kHz, and 7 kHz in (a) slow and (b) fast formations. Radial sensitivities are given by equation 2.33.

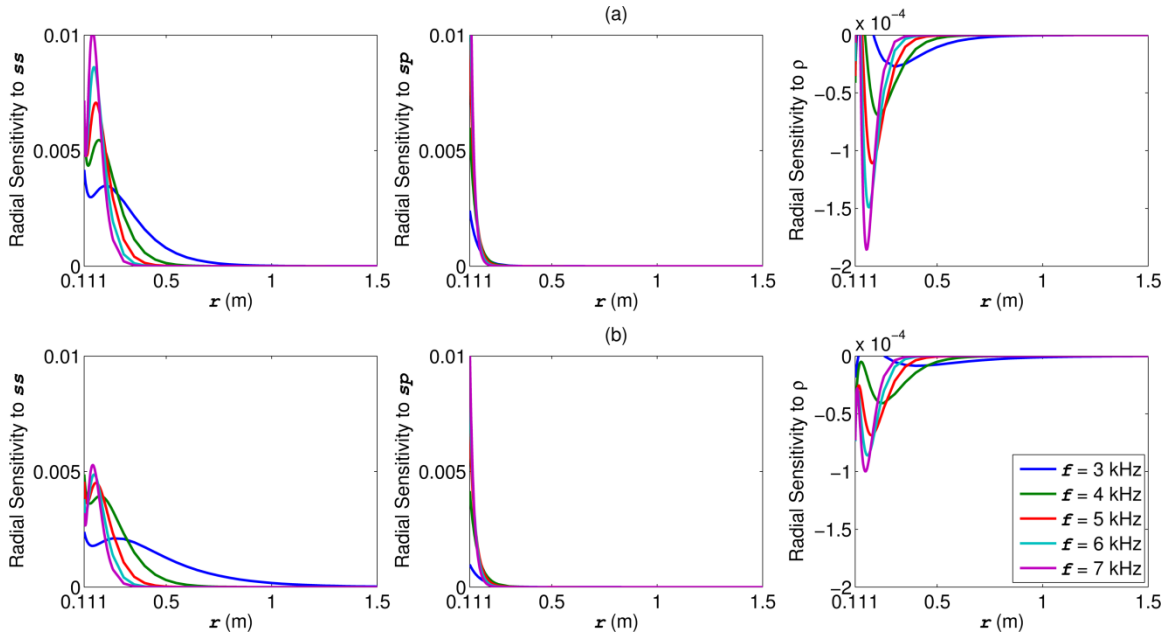

Figure 2.9: Radial sensitivity of the flexural mode to perturbations of shear slowness (ss), compressional slowness (sp), and formation density (ρ), measured with a wireline tool at 3 kHz, 4 kHz, 5 kHz, and 6 kHz in (a) slow and (b) fast formations. Radial sensitivities are given by equation 2.33.

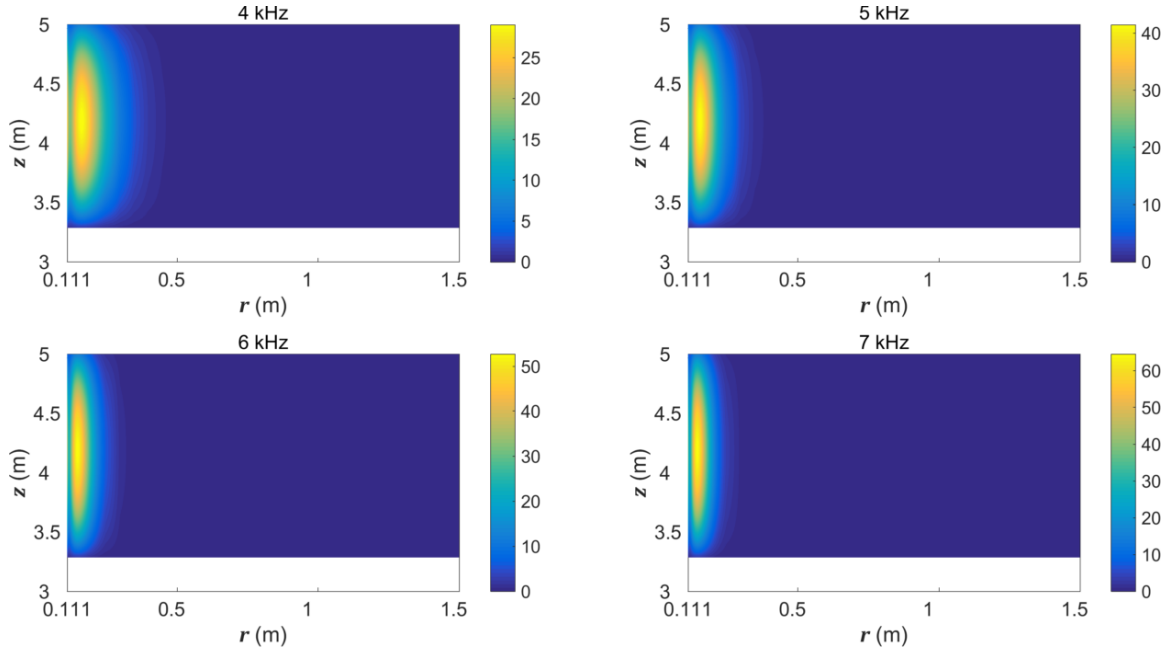

Figure 2.10: Axial-radial sensitivity of the quadrupole mode to perturbations of shear slowness measured with an LWD tool at 4 kHz, 5 kHz, 6 kHz, and 7 kHz in a slow formation. Axial-radial sensitivities are given by equation 2.34 normalized by $r\Delta r\Delta z$. The depth of investigation is approximately 0.5 m at low frequencies and decreases to 0.3 m at higher frequencies.

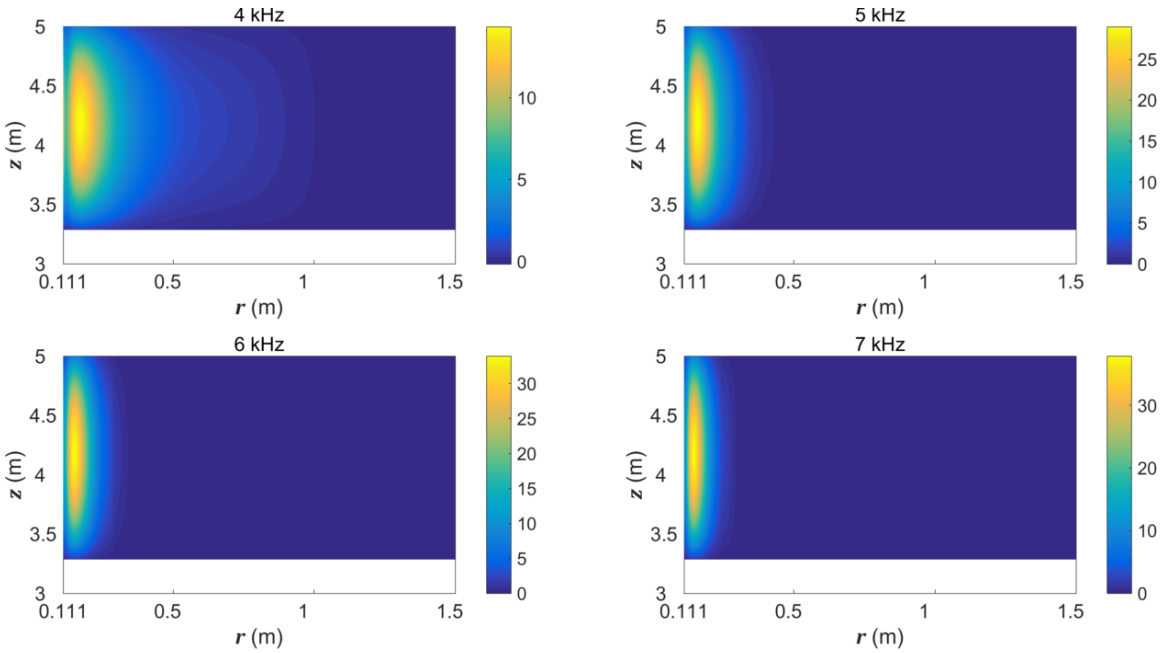

Figure 2.11: Axial-radial sensitivity of the quadrupole mode to perturbations of shear slowness measured with an LWD tool at 4 kHz, 5 kHz, 6 kHz, and 7 kHz in a fast formation. Axial-radial sensitivities are given by equation 2.34 normalized by $r\Delta r\Delta z$. The depth of investigation is approximately 1 m at low frequencies and decreases to 0.3 m at higher frequencies.

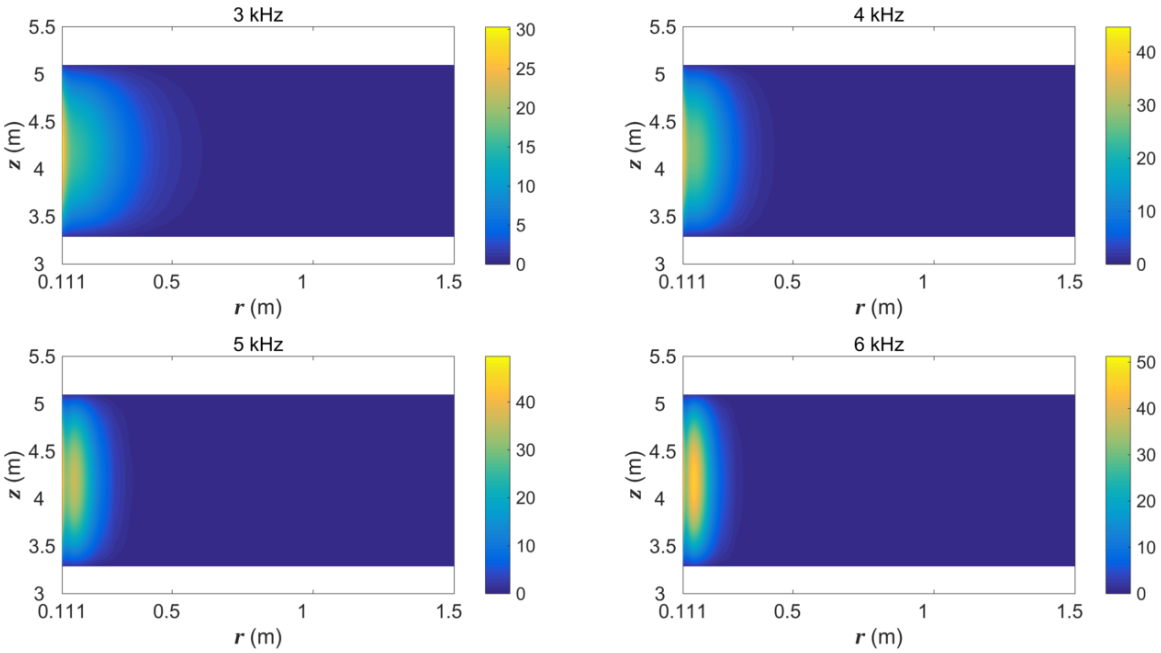

Figure 2.12: Axial-radial sensitivity of the flexural mode to perturbations of shear slowness measured with a wireline tool at 3 kHz, 4 kHz, 5 kHz, 6 kHz, and 7 kHz in a slow formation. Axial-radial sensitivities are given by equation 2.34 normalized by $r\Delta r\Delta z$. The depth of investigation is approximately 0.5 m at low frequencies and decreases to 0.3 m at higher frequencies.

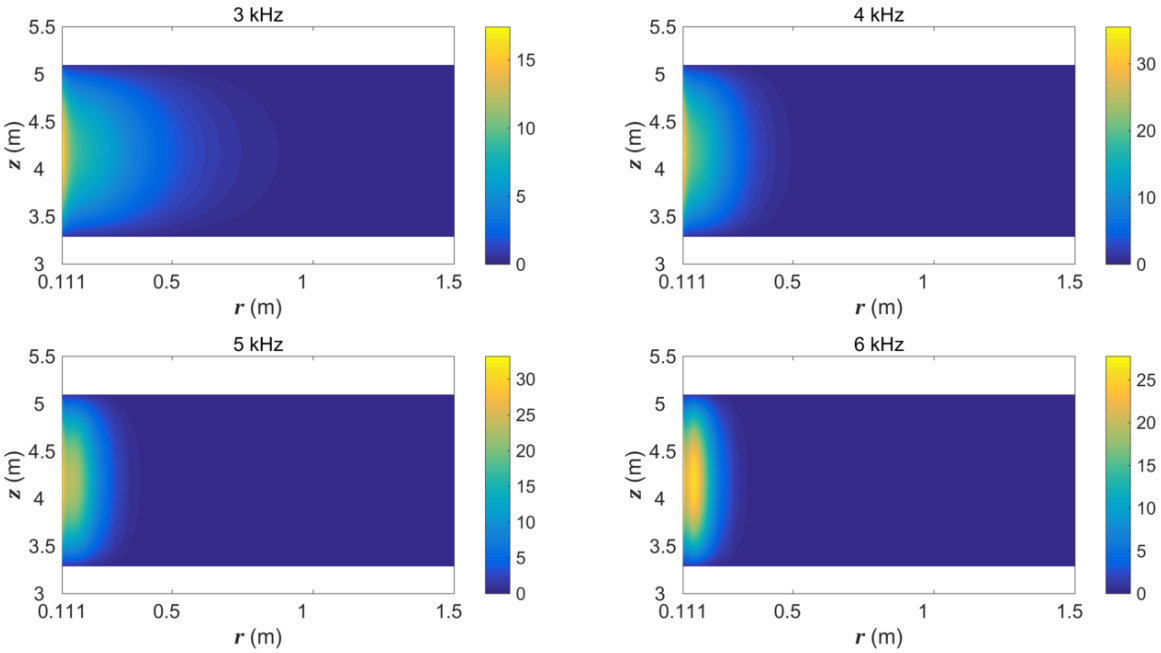

Figure 2.13: Axial-radial sensitivity of the flexural mode to perturbations of shear slowness measured with a wireline tool at 3 kHz, 4 kHz, 5 kHz, and 6 kHz in a fast formation. Axial-radial sensitivities are given by equation 2.34 normalized by $r\Delta r\Delta z$. The depth of investigation is approximately 0.9 m at low frequencies and decreases to 0.3 m at higher frequencies.

Chapter 3: Physics-Based Method to Mitigate Noise in Borehole Sonic Logs Using Fast-Forward Modeling and Inversion

A major challenge in the interpretation of seismic measurements and sonic logs is the presence of deleterious noise that impacts the quality and reliability of estimated seismic wavelets and seismic inversion products. I introduce an inversion-based method to mitigate processing errors, spatial averaging effects, and borehole environmental noise on sonic logs. The inversion-based method estimates layer-by-layer elastic properties via joint inversion of shear and compressional logs measured in a vertical well and uses the estimated elastic properties of the assumed horizontal layers to model noise-mitigated sonic logs. Sonic logs are efficiently modeled by invoking axial sensitivity functions of shear and compressional logs. I first test the inversion-based method with synthetic sonic logs contaminated with noise. Estimated layer-by-layer elastic properties exhibit maximum relative differences of 5% compared to those of the original model while efficiently reducing the numerical noise included in the input measurements. I then apply the method to noisy sonic logs acquired in the deepwater Gulf of Mexico and in the North Sea and estimate angle reflectivity from the noise-mitigated logs. Results verify the reliability of the inversion-based method to reduce biases in the calculated angle reflectivity within a few minutes of CPU time. By making use of geometrical and physical constraints for noise reduction, implicit in the inversion-based method, I obtain sonic logs that more accurately reflect the physical properties of rock formations penetrated by wells.

3.1 INTRODUCTION

Noise and spikes typically present in sonic logs decrease the accuracy with which the latter can be used to determine rock elastic properties. I classify noise present in sonic logs into three categories: (1) numerical noise caused by round-off errors and limitations of waveform processing algorithms (Kimball and Marzetta, 1984); (2) instrument errors caused by tool vibration (Song et al., 2017), tool eccentricity (Pardo et al., 2013), temperature drift, electronic noise, and spatial averaging effects (Close et al., 2009; Mallan et al., 2011); and (3) formation irregularities, such as washouts, breakouts, mudcake, and fractures (Souder, 2002; Chi et al., 2006; Ellis and Singer, 2007; Oyler et al., 2008).

Presence of noise in sonic logs must be addressed to reliably estimate in-situ rock elastic properties for geomechanical, seismic, and petrophysical studies (Mallan et al., 2009). Noise reduction in sonic logs is typically performed by re-processing and filtering sonic waveforms. These methods, however, are time-consuming and often disregard the fundamentals of borehole wave propagation. Other methods rely on effective-medium theories (Sayar and Torres-Verdín, 2016), neural networks, or compressional-to-shear velocity ratio models to reconstruct sonic logs, but such methods are non-unique and often require calibration with core data.

I introduce a physics-based method to mitigate noise present in borehole sonic logs via joint inversion of shear and compressional logs. First, I assume a vertical well and construct a multi-layer (horizontal layers) earth model of unknown slownesses where I determine the location of bed boundaries from gamma ray (GR), bulk density (ρ), or sonic logs. Next, I jointly invert shear and compressional logs to estimate layer-by-layer

slownesses of the earth model and use the calculated slownesses to model sonic logs with mitigated measurement noise. There are two advantages to the inversion-based method: First, the joint-inversion method invokes mechanical and geometrical properties of the actual sonic tool used to acquire the measurements to model the sonic logs, rather than using numerical filters to remove noise. Second, because I construct a layered earth model prior to inversion, the inversion-based method mitigates spatial averaging effects and estimates layer-by-layer slownesses. I use axial sensitivity functions to fast-forward model sonic logs in a few seconds of CPU time, thereby improving the efficiency of the inversion. Because the sensitivity function takes into account the averaging effects implicit in the measurement of sonic logs, any spike present in the log with a full-width at half-maximum (FWHM) smaller than the FWHM of the sensitivity function is explicitly regarded as noise.

I apply the inversion-based method to synthetic examples to verify its accuracy, reliability, and stability. Synthetic shear and compressional logs are generated from numerical simulations by solving the wave equation via finite-element and finite-difference methods, respectively. Application of the inversion-based method to noisy sonic logs decreases noise contamination with minimal effect on the estimated rock properties. I show that applying the inversion-based method with bed boundaries uniformly spaced at the log sampling interval yields similar logs to those calculated when bed boundaries are known (correlation > 0.97). It is also found that inversion results improve when layer thicknesses are larger than the FWHM of the sensitivity function; for the case of synthetic formations where average layer thicknesses are smaller than the FWHM of the sensitivity function of the full receiver array, I show that applying the

inversion-based method on sonic logs calculated with a subset of the receiver array yields accurate inversion results.

I apply the inversion-based method to sonic logs acquired in the North Sea that exhibit noisy shear slownesses. Both sonic-log noise and spatial averaging effects are successfully mitigated concomitant with the estimation of layer-by-layer slownesses of 60 m-thick formations within a few minutes of CPU time. Seismic angle reflectivities are estimated from the modeled sonic logs which are effectively corrected for spikes and noise that would otherwise give rise to fictitious reflections on synthetic seismograms. Furthermore, I show that slight variations in bed-boundary locations do not significantly modify the noise-mitigated logs, and conclude that for noise reduction the exact location of bed boundaries is not strictly necessary.

3.2 METHOD

I first show how to construct the forward model and then describe how to use the forward model and implement the inversion-based interpretation approach.

3.2.1 Forward Modeling and Inversion

The forward modeling of shear and compressional logs is expressed as a function of the spatial averaging function F (equation 2.15), and is given by

$$\bar{s}^{\{l\}}(d) = \sum_{i=1}^{N} F(z_i - d)\, s^{\{l\}}\big(\mathbf{p}(z_i)\big), \tag{3.1}$$

where $\{l\}$ denotes shear or compressional mode, $s^{\{l\}}(\mathbf{p}(z_i))$ is slowness of the formation of elastic properties $\mathbf{p}$ at depth z_i, that is midway between receivers i and i +1 (see Section 2.2), d is depth of the log, and N is total number of receivers.

I apply the forward model (equation 3.1) to estimate layer-by-layer slownesses jointly from shear and compressional logs by minimizing the quadratic cost function given by

$$e(\mathbf{m}) = \|\mathbf{W_d} \cdot [\mathbf{f(m)} - \mathbf{u}]\|_2^2 + \alpha^2 \|\mathbf{\Lambda} \cdot [\mathbf{m} - \mathbf{m_0}]\|_2^2 \qquad 3.2$$

where the unknown model parameter vector $\mathbf{m} = [P_1 \dots P_{n_t}, L_1 \dots L_{n_t}]$, with $P_i = sp_i^2$, $L = ss_i^2 - 2sp_i^2$, where sp_i and ss_i are the compressional and shear slownesses of layer i, respectively and n_t is number of layers, while the data (measurement) vector is given by $\mathbf{u} = [\mathbf{u_p}, \mathbf{u_s}]$, where $\mathbf{u_p}$ and $\mathbf{u_s}$ are the measured slowness logs, and $\mathbf{f(m)} = [\mathbf{s_{sp}(m)}, \mathbf{s_{ss}(m)}]$, where $\mathbf{s_{sp}}$ and $\mathbf{s_{ss}}$ are the compressional and shear slowness logs, respectively, calculated with axial sensitivity functions. The second term in equation 3.2 is a Tikhonov regularization (stabilization) term, where α is the regularization parameter and $\mathbf{\Lambda}$ is a regularization weighing matrix; for first- and second-order regularization $\mathbf{m_0} = 0$, while for zeroth-order regularization $\mathbf{m_0} = [\bar{P}_1 \dots \bar{P}_{n_t}, \bar{L}_1 \dots \bar{L}_{n_t}]$, where $\bar{P}_i$ and $\bar{L}_i$ are calculated from the average values of shear and compressional logs within layer i. The data weighing matrix, denoted as $\mathbf{W_d}$, is a diagonal matrix equal to $\mathrm{diag}[w_1 \dots w_Q]$, where Q is the total number of data; $w_k = 0$, when the k-th measurement is unreliable and does not satisfy rock physics constraints (e.g., $u_s/u_p < \sqrt{2}$ or $u_s/u_p > 4$) and $w_k = 1$ otherwise.

I use the Levenberg-Marquardt method (Aster et al., 2005) to minimize the quadratic cost function (equation 3.2). To choose the regularization parameter α, I plot the norm of the misfit between measured and forward-modeled logs versus α and choose α for which the curvature of the misfit is maximum. Maximum curvature yields the value

of α at which the forward model has been devoid of most of the high-amplitude noise. The forward model can be further restricted with additional rock physics models (e.g., mineralogy-based models relating porosity and elastic modulus to slowness) to constrain the estimation of **m.**

Although at first glance the inversion might appear to be only a low-pass filter, there are two major differences. First, low-pass filters are applied directly to noisy logs, thereby smoothing both noise and useful signal features while the inversion-based method incorporates the low-pass filter action of the sonic tool to produce blocky logs consistent with rock elastic constraints. And second, the low-pass filter action of the tool is applied on the blocky log to *simulate the measurements*, not on the data to *eliminate noise*.

3.2.2 Calculation of Jacobian

The Jacobian matrix can be derived analytically from equation 3.2. When $\alpha = 0$, and model parameters are expressed in terms of elastic constants the cost function is given by

$$e(\mathbf{m}) = \left\|E^{(p)}\right\|_2^2 + \left\|E^{(s)}\right\|_2^2, \tag{3.3}$$

$$e(\mathbf{m}) = \left\|{F_{ij}}^{(p)} B_j^{(p)} - {u_i}^{(p)}\right\|_2^2 + \left\|{F_{ij}}^{(s)} B_j^{(s)} - {u_i}^{(s)}\right\|_2^2, \tag{3.4}$$

where $E^{(p)}$and $E^{(s)}$are the misfits of forward model and data of compressional (p) and shear (s) slownesses, respectively and **B** is the model vector of slownesses of the layers. Therefore, the gradient of the cost function to model parameters *L* and *P* is given by

$$\frac{\partial e}{\partial L_k} = 2\left(F_{ij}{}^{(p)} B_j{}^{(p)} - u_i{}^{(p)}\right) F_{ik}{}^{(p)} \frac{\partial B_k{}^{(p)}}{\partial s_p} \frac{\partial s_p}{\partial L_k} + 2\left(F_{ij}{}^{(s)} B_j{}^{(s)} - u_i{}^{(s)}\right) F_{ik}{}^{(s)} \frac{\partial B_k{}^{(s)}}{\partial s_s} \frac{\partial s_s}{\partial L_k}, \tag{3.5}$$

$$\frac{\partial e}{\partial P_k} = 2\left(F_{ij}{}^{(p)} B_j{}^{(p)} - u_i{}^{(p)}\right). F_{ik}{}^{(p)} \frac{\partial B_k{}^{(p)}}{\partial s_p} \frac{\partial s_p}{\partial P_k} + 2\left(F_{ij}{}^{(s)} B_j{}^{(s)} - u_i{}^{(s)}\right). F_{ik}{}^{(s)} \frac{\partial B_k{}^{(s)}}{\partial s_s} \frac{\partial s_s}{\partial P_k}, \tag{3.6}$$

where

$$s_s = \sqrt{L + 2P}, \tag{3.7}$$

$$s_p = \sqrt{P}, \tag{3.8}$$

$$\frac{\partial s_p}{\partial L_k} = 0, \tag{3.9}$$

$$\frac{\partial s_p}{\partial P_k} = \frac{1}{2\sqrt{P_k}}, \tag{3.10}$$

$$\frac{\partial s_s}{\partial L_k} = \frac{1}{2\sqrt{L_k + 2P_k}}, \tag{3.11}$$

$$\frac{\partial s_s}{\partial P_k} = \frac{1}{\sqrt{L_k + 2P_k}}. \tag{3.12}$$

Therefore, the Jacobian matrix is expressed as

$$\mathbf{J} = \begin{bmatrix} 0 & \frac{F^{(s)}}{2\sqrt{L+2P}} \\ \frac{F^{(p)}}{2\sqrt{P}} & \frac{2F^{(s)}}{\sqrt{L+2P}} \end{bmatrix}. \tag{3.13}$$

3.3 SYNTHETIC EXAMPLE

I consider a thinly bedded formation logged with a wireline tool (Table 3.1) centered in an 8-inch (0.2032 m) vertical borehole. Noise-free shear and compressional logs are calculated via numerical simulations. To calculate the shear log, I first simulate the flexural mode spectrum at low frequencies using an hp-adaptive finite-element numerical method (Matuszyk et al., 2013) and then process the spectrum with the matrix-

pencil method. To calculate the compressional log, I first simulate the time-domain waveforms using a finite-difference method and then process the waveforms with the slowness-time-coherence (STC) method (Kimball and Marzetta, 1984). The sampling interval of the logs is one measurement per 0.5 ft. I then add exponential noise with a minimum amplitude cut-off to the noise-free logs. Depth locations of spikes on sonic logs are chosen randomly. Spike width varies from 1 ft (0.3048 m) to 2.5 ft (0.762 m), while noise appears simultaneously on shear and compressional logs. Figure 3.1 shows the noise-free and noisy shear and compressional logs together with the true layer slownesses (identified with dashed lines). Slowness contrast between adjacent layers varies between 5% and 19%. Layer boundaries are assumed known, and I derive initial estimates of slownesses in each layer from the average of the shear and compressional logs within that layer.

I apply the inversion-based method to the noisy shear and compressional logs with a unity data weighting matrix at all depths. The method converges in a few seconds of CPU time and after only 8 iterations, indicating stability and high convergence rate of the nonlinear minimization procedure. Figure 3.2 shows the inverted shear and compressional slownesses together with the modeled logs that are almost noise free given that the inversion process has removed the spikes. To quantify the uncertainty of inversion results, I add the same amount of exponential noise to the modeled sonic logs and invoke the inversion method to calculate the mean and standard deviation of the inverted slownesses. Figure 3.2 shows the error (uncertainty) bars and the inverted slownesses (shown with dashed lines), which fall within the error-bar range 68% of the time; the maximum standard deviation is 3.2 μs/ft. Finally, Figure 3.3 shows that the

inverted slownesses and the modeled sonic logs match the true slownesses and the noise-free sonic logs, respectively, with a standard deviation under 2.4 μs/ft as detailed in Table 3.2. Additionally, the inversion-based method mitigates averaging effects; initially, the difference between noise-free compressional and shear logs and true layer slownesses exhibited standard deviations of 3.17 μs/ft and 5.43 μs/ft, respectively. By estimating layer-by-layer slownesses, the standard deviation is decreased by a factor of 2 (see the summary of results in Table 3.2).

3.4 FIELD EXAMPLES OF APPLICATION

3.4.1 Field Example 1, Deepwater Gulf of Mexico

I apply the inversion method to noisy slowness logs acquired in the deepwater Gulf of Mexico (waveforms were not available). Bed boundaries are detected from the GR log by locating its inflection points. I discard beds located in depth sections where log data variations are small (slope << 1) as well as beds separated by a distance smaller than the FWHM of the sensitivity function. Initial estimates of slownesses in each layer are calculated from the average values of shear and compressional slowness logs within that layer. Figure 3.4 shows the caliper, GR, density, and compressional and shear slowness logs; layer boundaries detected with the GR log are shown with dashed lines. The well segment is approximately 30 m and is oil saturated below 3640 m and gas saturated above 3640 m; the gas-saturated depth interval is shaly.

I calculate the axial sensitivity function with the tool properties described in Table 3.3. Figure 3.5 shows the estimated layer-by-layer shear and compressional slownesses

together with the noise-mitigated sonic logs calculated by minimizing equation 3.2 using 2nd order Tikhonov regularization.

3.4.2 Field Example 2, North Sea

I apply the inversion method to noisy slowness logs acquired in the North Sea (waveforms were not available). Bed boundaries are detected from three sets of logs: GR, density, and compressional slowness by locating their inflection points. I discard beds located in depth sections where slowness variations are small (slope << 1) as well as beds separated by a distance smaller than the FWHM of the sensitivity function. Initial estimates of slownesses in each layer are calculated from the average values of shear and compressional slowness logs within that layer. Figure 3.6 shows the caliper, GR, density, and compressional and shear slowness logs; layer boundaries detected with the GR log are shown with dashed lines. Formations were drilled with oil-based mud, are gas saturated from 2540 m to 2560 m, and exhibit variable borehole enlargements from 2496 m to 2530 m. In the latter depth interval, the quality of shear slowness is low, and measurements are missing at 2498 m, 2508 m, and 2526 m.

I calculate the axial sensitivity function with the tool properties described in Table 3.3. Figure 3.7 shows the estimated layer-by-layer shear and compressional slownesses together with the noise-mitigated sonic logs calculated by minimizing equation 3.2 using 2nd order Tikhonov regularization; spikes are removed by the inversion-based method, and the noise-mitigated shear slowness more closely follows the compressional slowness variations. I evaluate the effect of the choice of bed boundaries on the noise-mitigated logs; Figure 3.8 compares the estimated layer slownesses and noise-mitigated sonic logs calculated when bed boundaries are detected with GR, density, and compressional logs.

Differences between the noise-mitigated logs exhibit standard deviations below 3 μs/ft, implying that slight variations in bed-boundary locations have a negligible effect on the noise-mitigated sonic logs.

To show the impact of noisy sonic logs on synthetic seismograms, I calculate angle reflectivities with both the field logs and noise-mitigated logs shown in Figure 3.7 using Shuey's approximation (Shuey, 1985), given by

$$R(\theta) = R(0) + H \sin^2(\theta), \tag{3.14}$$

$$R(0) = \frac{1}{2}\left(\frac{\Delta v_p}{v_p} + \frac{\Delta \rho}{\rho}\right), \tag{3.15}$$

$$H = \frac{1}{2}\frac{\Delta v_p}{v_p} - 2\frac{v_s^2}{v_p^2}\left(\frac{\Delta \rho}{\rho} + 2\frac{\Delta v_s}{v_s}\right), \tag{3.16}$$

where $R(\theta)$ is angle reflectivity at angle θ; ρ is density, v_p compressional velocity, and v_s shear velocity; Δv_p, Δv_s, and $\Delta \rho$ are the variation across a layer boundary of compressional velocity, shear velocity, and density, respectively. Figure 3.9 shows the calculated angle reflectivity at 10^o, 20^o, and 30^o. Comparison of reflectivity calculated with field logs (black) to reflectivity calculated with noise-mitigated logs (gray) confirms that noise-mitigated sonic logs significantly reduce the deleterious influence of artificial reflections on synthetic seismograms.

3.5 DISCUSSIONS

3.5.1 Bed-Boundary Locations

Before applying the inversion-based interpretation method, it is necessary to determine the location of bed boundaries. When bed-boundary locations are not known, I assume layer boundaries uniformly spaced by the sampling interval of the sonic logs. In

this case, the inversion method mitigates noise and spikes on sonic logs but does not reduce averaging effects; inverted layer slownesses approach the sonic logs. I illustrate the previous statement by recalculating the noise-mitigated logs of Figure 3.3 with bed boundaries placed every 0.1524 m (log sampling interval). Figure 3.10 shows the noise-mitigated modeled logs (gray) corrected for noise and the inverted slownesses (gray dashed lines) that approach the modeled sonic logs. As described in Table 3.4, increasing the number of bed boundaries does not significantly change the correlation or the difference between modeled and noise-free sonic logs.

3.5.2 Effect of Thin Layers

In the previous synthetic and field examples, layers were thicker than the FWHM of the sensitivity function (0.4 m). I now test the inversion-based method across a formation with layer thicknesses varying from 0.24 m to 0.5 m. The regularization parameter is set to $\alpha = 0$ because sonic logs are noise free. Figure 3.11 shows that inverted properties do not agree with true layer properties, having a standard deviation of 3.46 μs/ft and 4.89 μs/ft for the compressional and shear slownesses, respectively, and a maximum error bar of 32 μs/ft. To improve the inversion results, and better resolve thin beds, I use a sub-array of receivers of 0.914 m (7 receivers) to calculate sonic logs rather than using the complete receiver array of 1.83 m (13 receivers) included in the sonic tool (Hsu and Chang, 1987; Zhang et al., 2000). In Figure 3.12, I show the inversion results obtained when the input data consist of sub-array logs; estimated slownesses agree with the original slownesses with a standard deviation below 2 μs/ft and a maximum error bar of 8.4 μs/ft. Therefore, I conclude that sub-array processing increases the vertical resolution of logs from 1.83 to 0.9 m and the inversion-based method further improves

the estimation of layer slownesses. When shortening the receiver array further to 0.3048 m (3 receivers), the signal-to-noise ratio of sonic logs decreases (Figure 3.13). Thus, using fewer receivers to calculate sonic logs introduces additional processing noise to the inversion-based interpretation method.

3.5.3 Limitations of the Method

An important step in the proposed inversion-based interpretation method is the construction of a geometrical model composed of homogeneous and horizontal beds penetrated by a borehole orthogonal to bedding. Therefore, if bed boundaries are ill-defined or are missing the inversion-based method can over smooth actual features present in rock formations. Additionally, the accuracy of the method decreases in complex geometries that include dipping layers or variations of layer properties in the azimuthal direction (e.g., non-symmetric washouts or breakouts) because using axial sensitivity functions to calculate logs assumes that elastic properties are constant in the azimuthal and radial directions. Consider, for example, the washout of 3.62 cm filled with water-based mud shown in Figure 3.14. Figure 3.15 compares the simulated logs with and without borehole washout, indicating that presence of the washout in the center layer alters the quality of sonic logs in adjacent layers and that the shear log is less affected by the presence of washouts than the compressional log. Figure 3.16 shows that inverted slownesses are biased compared to true layer slownesses because the inversion-based method assumes homogeneous layers and calculates an effective slowness for the washout-formation layer, which will not correspond to the true formation slowness.

To appraise the accuracy of inversion results, it is important to examine the data residuals yielded by the inversion. A bimodal distribution or a biased (nonzero mean)

distribution could indicate model limitations (e.g., depth mismatches, complex geometries, etc.), while outliers could indicate noise. For example, if two layers in the formation with different shear/compressional velocities are modeled as a single layer, the calculated slowness using the inversion-based method would be an averaged slowness across the two layers; this would yield a bimodal distribution of data residuals.

3.6 SUMMARY AND CONCLUSIONS

I developed and successfully verified a new inversion-based method to reduce noise contamination in shear and compressional sonic logs. The method uses axial sensitivity functions to estimate layer-by-layer slownesses of rock formations penetrated by a vertical well and uses the estimated slownesses to calculate noise-mitigated shear and compressional logs. Noise-mitigated shear and compressional logs can be used to improve the calculation of angle reflectivity, synthetic seismograms, and seismic waveforms.

The accuracy and reliability of the inversion-based method were verified with synthetic examples where sonic logs were affected by spikes, processing noise, and averaging effects. I mitigated these effects by calculating sonic logs that honor rock-physics constraints and by estimating layer-by-layer slownesses. It was found that the estimation of rock elastic properties was accurate when layer thickness was greater than the FWHM of the sensitivity function and when the width of spikes was smaller than the corresponding layer thickness. For layer thicknesses smaller than the FWHM of the sensitivity function, I showed that combining sub-array processing with the inversion-based method yields accurate and reliable inversion results. The proposed inversion-based interpretation method requires the construction of a layered geometrical model;

when bed-boundary locations are not known, the method can be implemented with uniformly spaced bed boundaries along the depth interval at the expense of decreased accuracy of the estimated layer-by-layer slownesses.

The inversion-based method to mitigate noise can also be used to quality-check sonic logs and process several hundred feet of logs in a few minutes of CPU time. It is a practical and reliable alternative to costly sonic waveform re-processing, filtering, or to reproducing sonic logs via effective medium theories.

3.7 TABLES AND FIGURES

Table 3.1: Geometric properties for the wireline tool assumed in the synthetic examples considered in Chapter 3.

Number of receivers	13
Inter-receiver spacing (m)	0.1524
First receiver offset (m)	3.2766
Inner/outer radius (m)	NA/0.046

Table 3.2: Standard deviation of the difference between noise-free compressional (P) and shear (S) logs, modeled logs, and true and inverted slownesses for the synthetic example described in Figure 3.3.

	Noise-free P/S logs	**Inverted P/S slownesses**
True P/S slownesses	3.17 μs/ft / 5.43 μs/ft	1.49 μs/ft / 2.36 μs/ft
Modeled P/S logs	1.21 μs/ft / 1.62 μs/ft	

Table 3.3: Geometrical properties of the tool used to construct the sensitivity functions for rock formations in the deepwater Gulf of Mexico and the North Sea.

Number of receivers	8
Inter-receiver spacing (m)	0.1524
Receiver offset of dipole source (m)	2.74
Receiver offset of monopole source(m)	3.35
Inner/outer radius (m)	NA/0.046

Table 3.4: Correlation and standard deviation of the difference between modeled logs and inverted compressional (P) and shear (S) slownesses shown in Figure 3.3 and Figure 3.10 to noise-free logs.

	P/S modeled logs for the synthetic example shown in Figure 3.3	**P/S modeled logs for the synthetic example with thin layers (Figure 3.10)**	**P/S inverted slownesses for the synthetic example shown in Figure 3.3**	**P/S inverted slownesses for the synthetic example with thin layers (Figure 3.10)**
Correlation to noise-free logs	0.98/0.98	0.98/0.97	0.98/0.98	0.90/0.87
Standard deviation to noise-free logs	1.21 μs/ft / 1.62 μs/ft	1.17 μs/ft /1.98 μs/ft	1.50 μs/ft / 2.36 μs/ft	3.35 μs/ft / 6.04 μs/ft

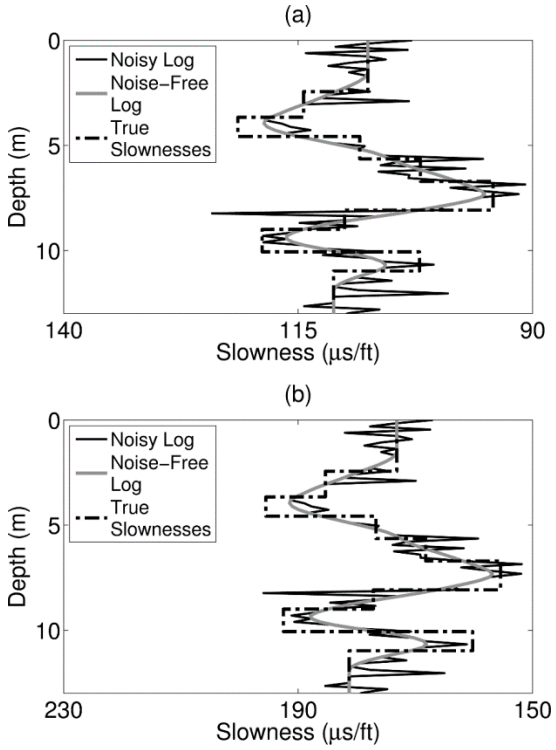

Figure 3.1: Comparison of noise-free logs (gray) to noisy logs (black) for (a) compressional and (b) shear slownesses measured with a wireline tool. Dashed lines identify the original layer-by-layer slownesses.

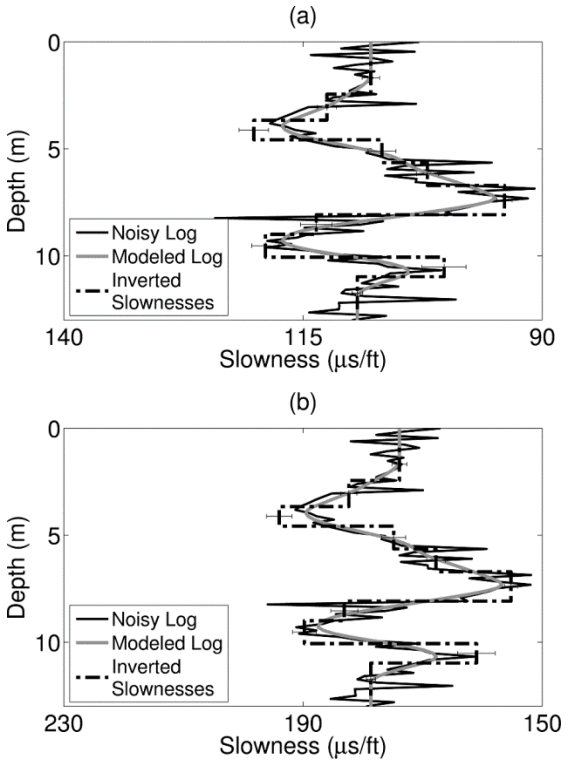

Figure 3.2: Comparison of noisy (black) to modeled (gray) logs calculated with the inversion-based method for (a) compressional and (b) shear slownesses measured with a wireline tool. Dashed lines with error bars identify the estimated layer-by-layer slownesses.

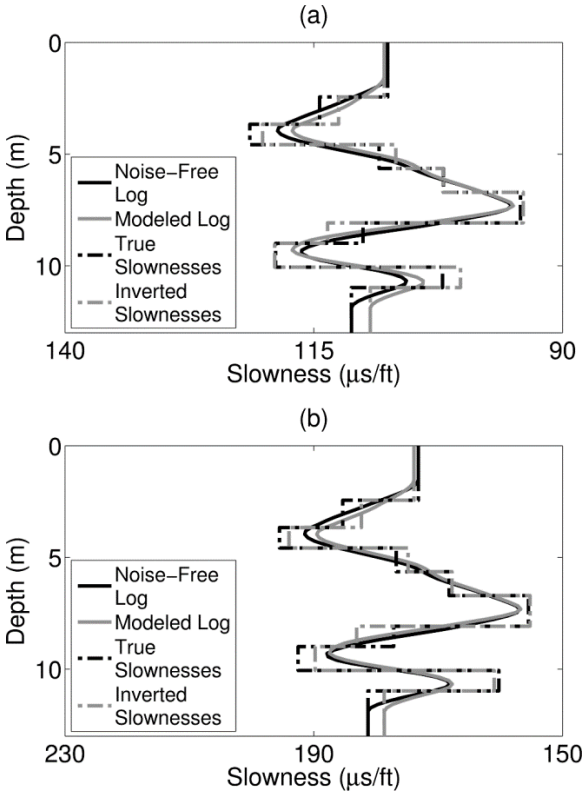

Figure 3.3: Comparison of noise-free (black) to modeled (gray) logs calculated with the inversion-based method for (a) compressional and (b) shear slownesses measured with a wireline tool. Black and gray dashed lines identify original and inverted layer-by-layer slownesses of the synthetic model, respectively.

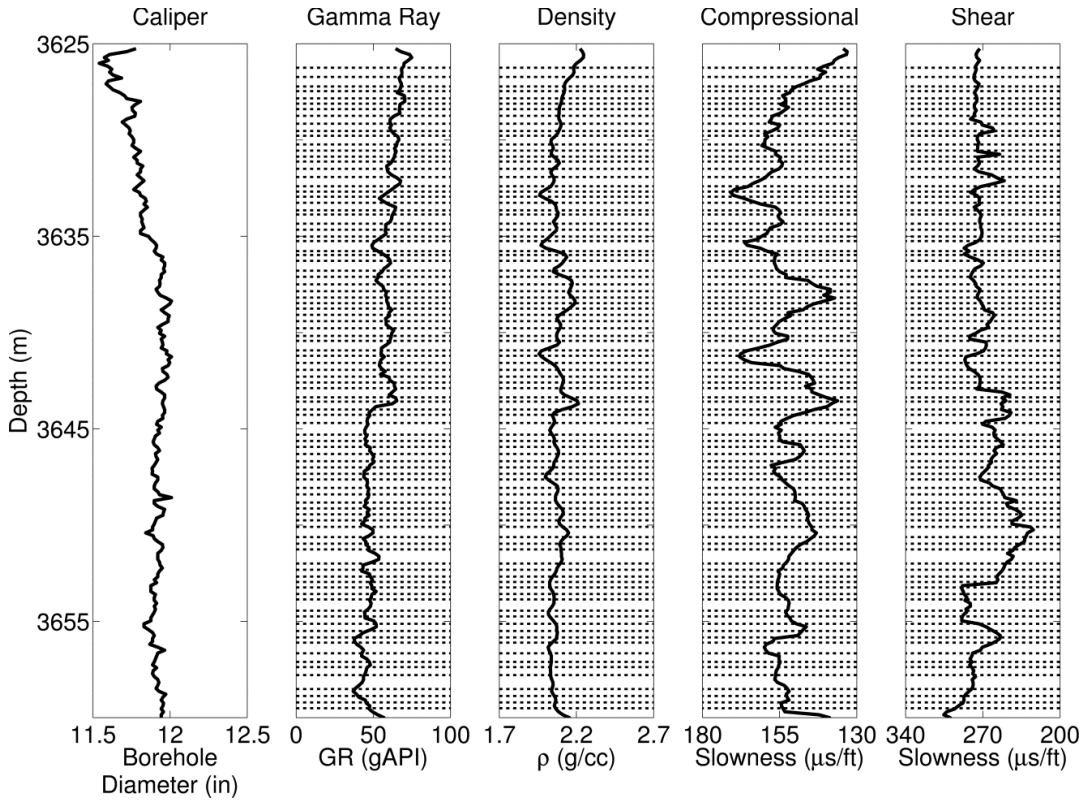

Figure 3.4: (From left to right) caliper, gamma ray, density, compressional slowness, and shear slowness logs acquired in the deepwater Gulf of Mexico. Horizontal dashed lines identify the locations of bed boundaries detected with the gamma-ray log.

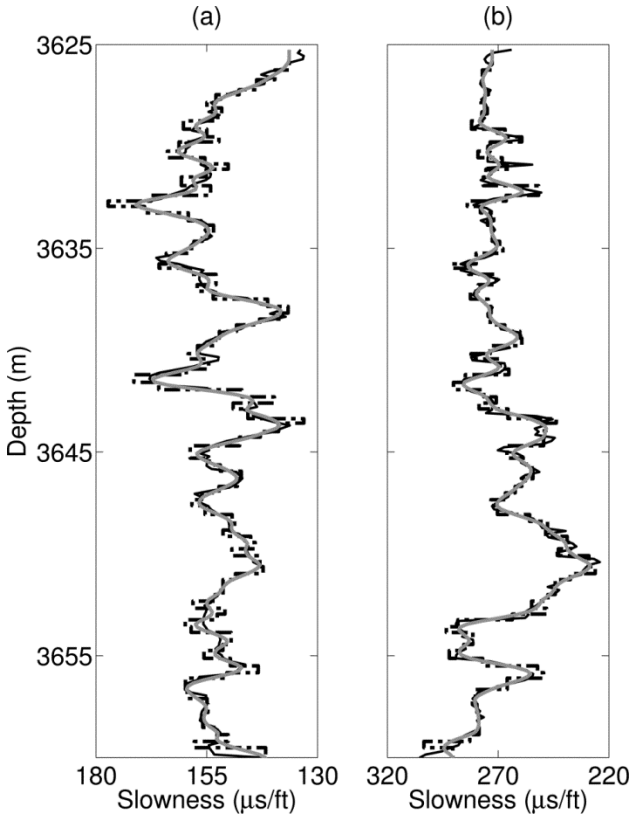

Figure 3.5: Comparison of field (black) and modeled sonic logs (gray) for (a) compressional and (b) shear slownesses in the deepwater Gulf of Mexico. Dashed lines identify the estimated layer-by-layer slownesses.

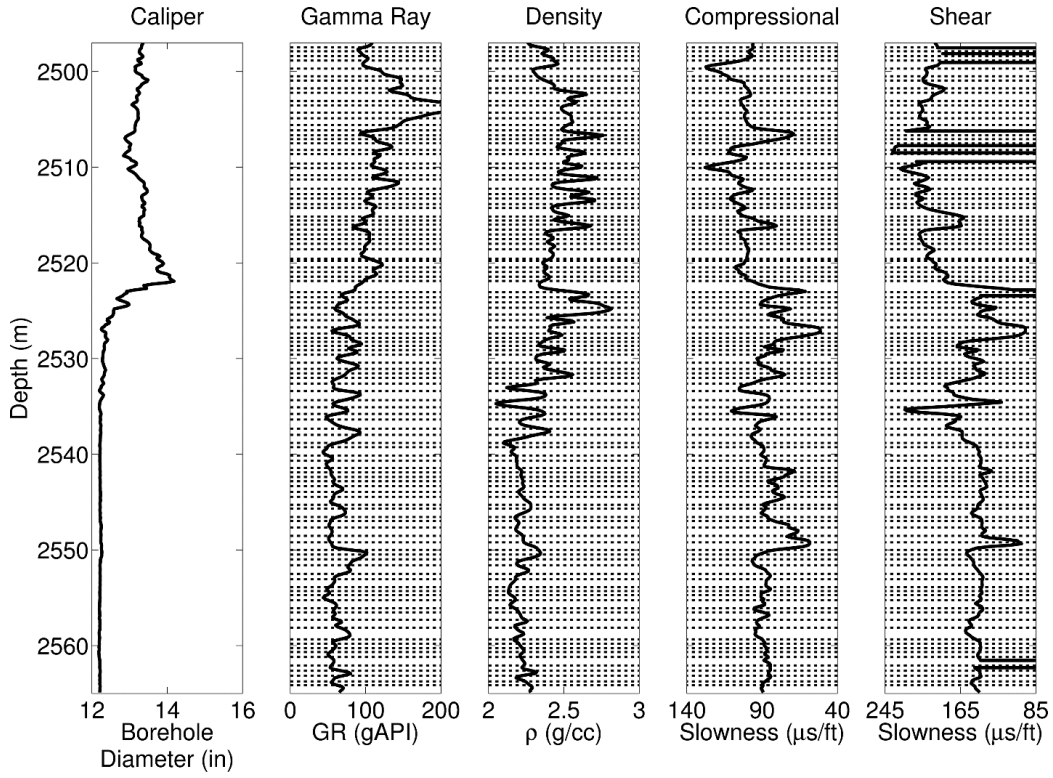

Figure 3.6: (From left to right) caliper, gamma ray, density, compressional slowness, and shear slowness logs acquired in the North Sea. Horizontal dashed lines identify the locations of bed boundaries detected with the gamma-ray log.

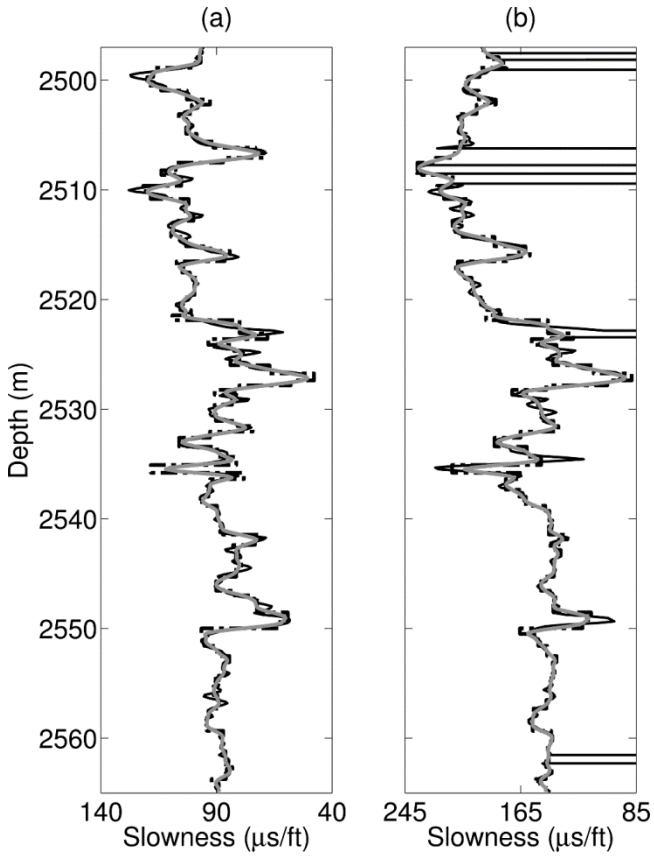

Figure 3.7: Comparison of field (black) and modeled sonic logs (gray) for (a) compressional and (b) shear slownesses in the North Sea. Dashed lines identify the estimated layer-by-layer slownesses.

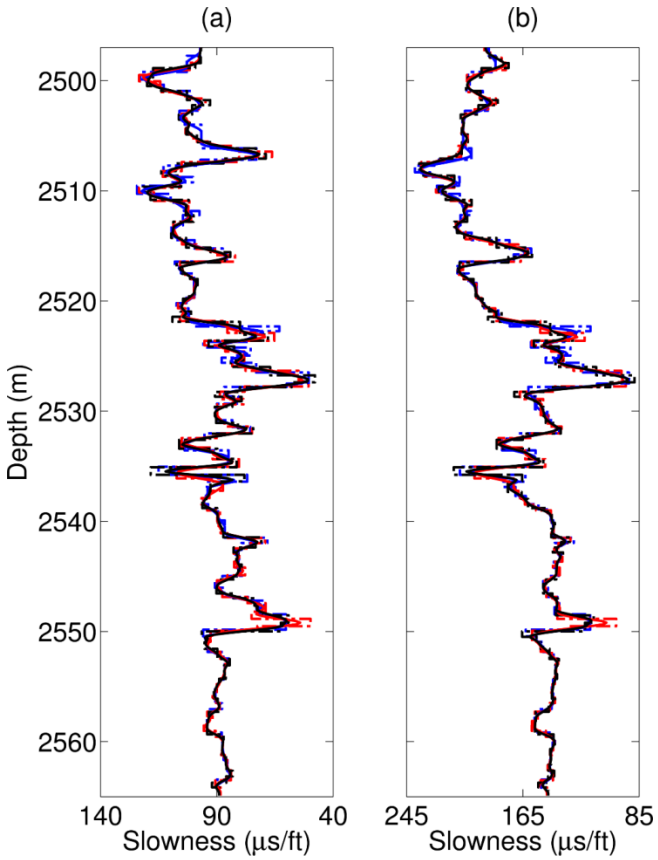

Figure 3.8: Modeled (a) compressional and (b) shear slowness logs in the North Sea calculated from the inversion-based method with bed boundaries detected with the gamma-ray log (black), the compressional log (blue), and the density log (red). Dashed lines identify the estimated layer-by-layer slownesses.

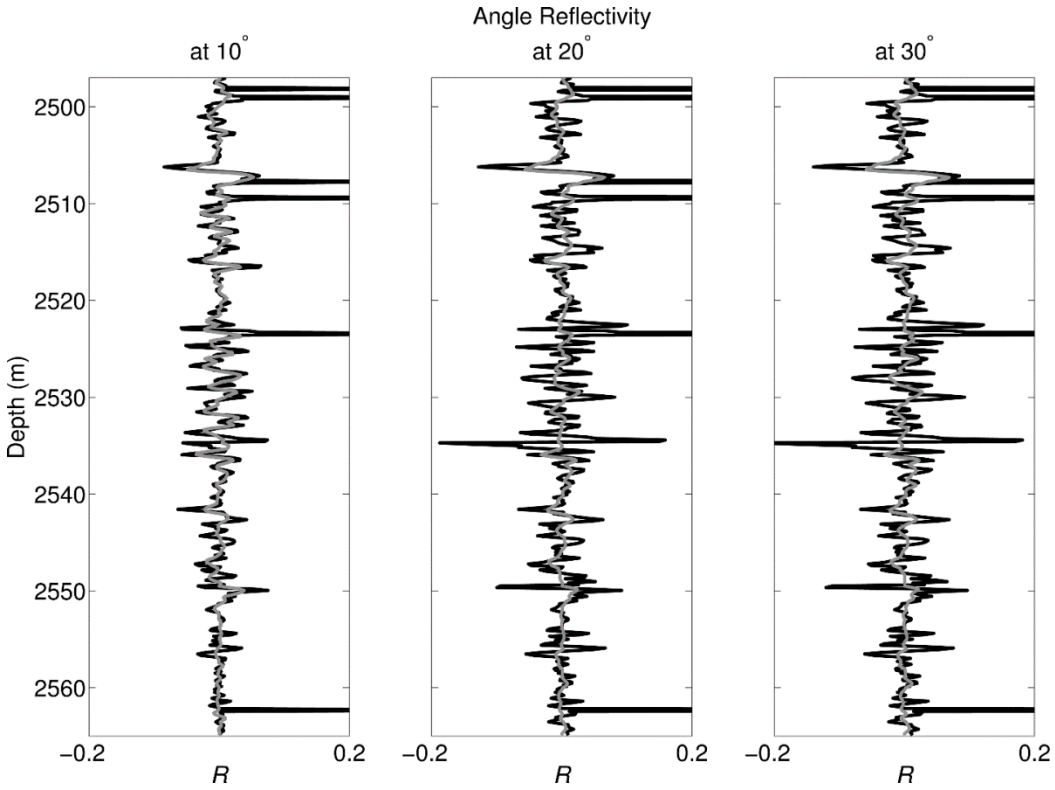

Figure 3.9: (From left to right) PP reflectivity at 10, 20, and 30 degrees calculated from measured sonic logs (black) and modeled sonic logs (gray) with bed boundaries detected with the gamma-ray log.

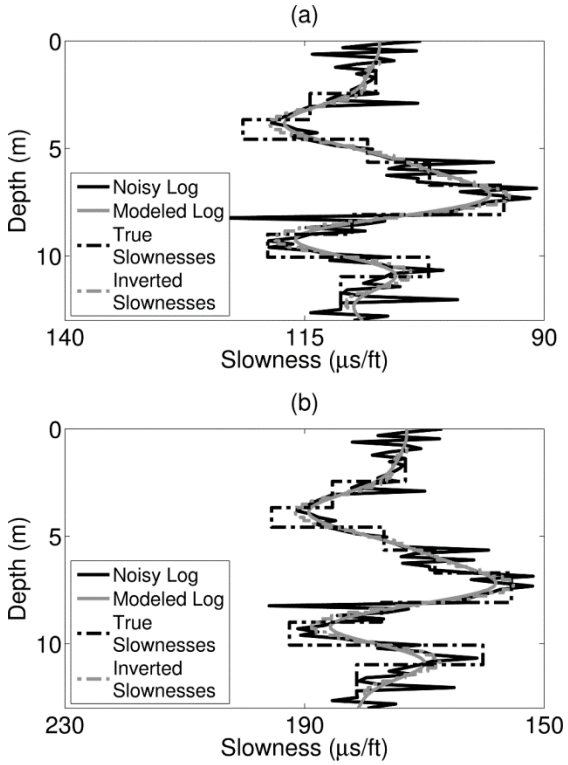

Figure 3.10: Comparison of noisy (black) and modeled (gray) logs calculated with the inversion-based method for (a) compressional and (b) shear slownesses measured with a wireline tool. Black and gray dashed lines identify original and inverted layer-by-layer slownesses. Inverted slownesses approach the modeled logs because layer thickness is constant and equal to 0.5 ft.

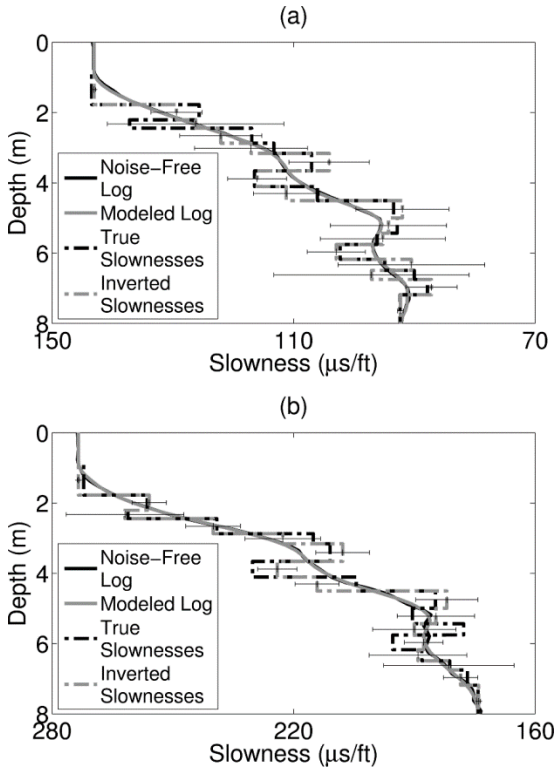

Figure 3.11: Comparison of noise-free (black) to modeled (gray) logs calculated with the inversion-based method for (a) compressional and (b) shear slownesses measured with a wireline tool. Black and gray dashed lines identify the original and inverted layer-by-layer slownesses of the inter-bedded formation, respectively. Error bars assess the relative uncertainty of inverted slownesses.

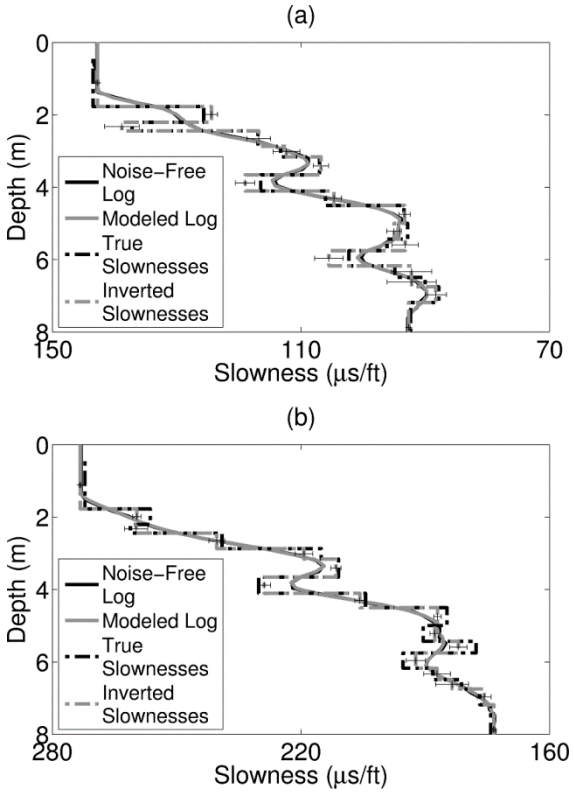

Figure 3.12: Comparison of noise-free (black) to modeled (gray) logs of (a) compressional and (b) shear slownesses calculated with receivers 4-10 of the wireline tool. Black and gray dashed lines identify original and inverted layer-by-layer slownesses of the inter-bedded formation, respectively. Error bars assess the relative uncertainty of inverted slownesses.

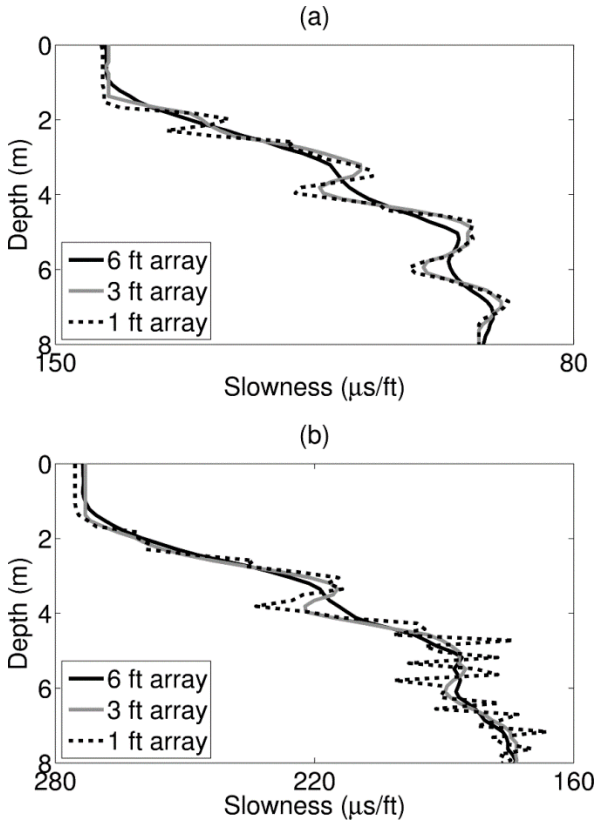

Figure 3.13: Comparison of the processed (a) compressional and (b) shear logs with receivers 1 – 13 (black), 4 – 10 (gray), and 6 – 8 (dashed) for the formation with thin layers shown in Figure 3.11.

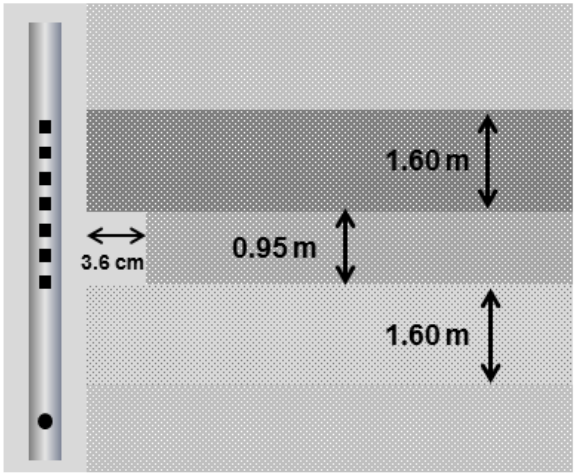

Figure 3.14: Geometrical description of a formation with five layers and a washout enlargement of 3.6 cm in the center layer. Receivers are identified with squares and the sonic transmitter with a circle on the wireline tool (figure not drawn to scale).

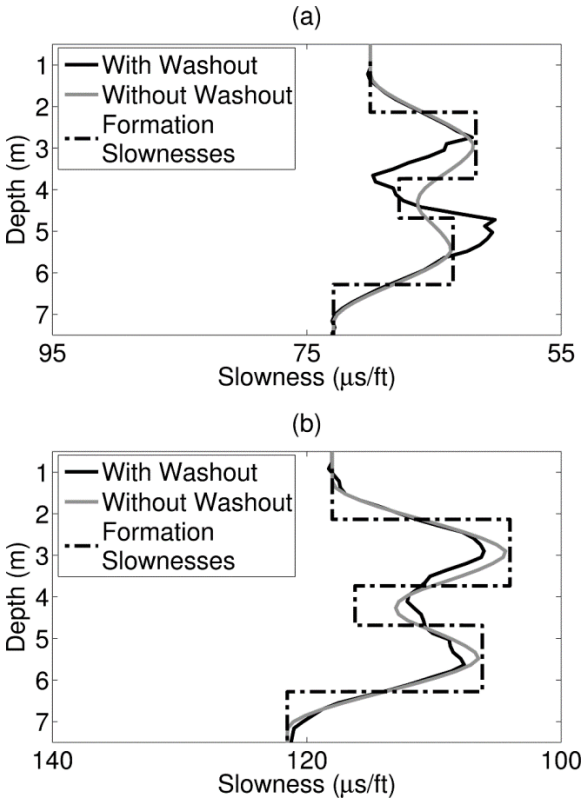

Figure 3.15: Comparison of noise-free logs without washout effects (gray) to logs simulated with washout effects (black) for (a) compressional and (b) shear slownesses measured with a wireline tool. Dashed lines identify layer-by-layer slownesses.

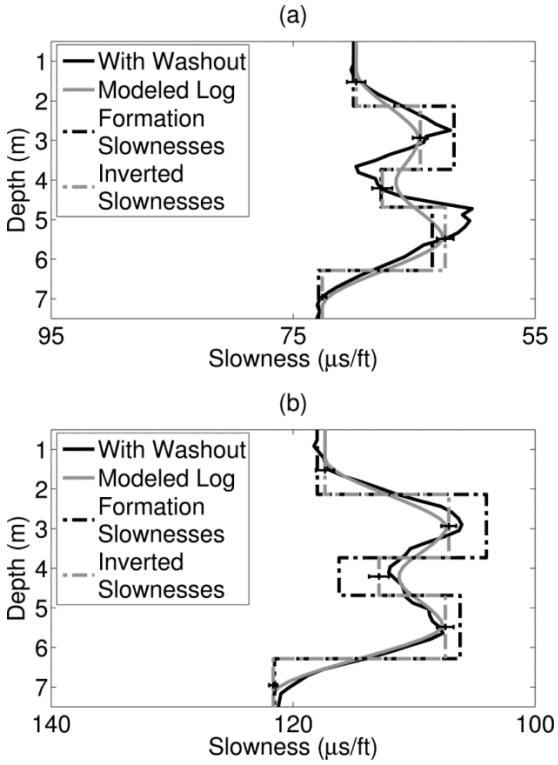

Figure 3.16: Comparison of logs with washout effects (black) to modeled logs (gray) of the formation shown in Figure 3.14 for (a) compressional and (b) shear slownesses. Dashed lines with error bars identify the estimated layer-by-layer slownesses.

Chapter 4: Estimation of Rock Stiffness Coefficients of Vertical Transversely Isotropic Formations from Borehole Sonic Measurements Acquired with Wireline and Logging-While-Drilling Instruments

In this chapter, I introduce an inversion-based method to estimate stiffness coefficients of VTI formations penetrated by vertical wells from compressional, Stoneley, and quadrupole/flexural modes measured with wireline or logging-while-drilling (LWD) instruments. First, I calculate the sensitivity functions of borehole sonic modes to stiffness coefficients; next, I use the sensitivities to estimate the stiffness coefficients of VTI layers from frequency-dependent borehole sonic logs. Because logs exhibit spatial averaging effects, I invoke inversion to calculate layer-by-layer slownesses of the formation prior to estimating stiffness coefficients. The method is verified with synthetic models of homogeneous and thinly-bedded formations.

4.1 INTRODUCTION

The relation between stress and strain of a solid is given by the generalized Hooke's law expressed as

$$\boldsymbol{\sigma} = \mathbf{C}\boldsymbol{\varepsilon} \tag{4.1}$$

where $\boldsymbol{\sigma}$ is the stress tensor, $\boldsymbol{\varepsilon}$ is the strain tensor, and $\mathbf{C}$ is the elastic stiffness tensor.

4.1.1 Isotropic Media

In isotropic media, the stiffness tensor with Voigt's notation is expressed as

$$\mathbf{C} = \begin{bmatrix} c_{33} & c_{13} & c_{13} & 0 & 0 & 0 \\ c_{13} & c_{33} & c_{13} & 0 & 0 & 0 \\ c_{13} & c_{13} & c_{33} & 0 & 0 & 0 \\ 0 & 0 & 0 & c_{44} & 0 & 0 \\ 0 & 0 & 0 & 0 & c_{44} & 0 \\ 0 & 0 & 0 & 0 & 0 & c_{44} \end{bmatrix}, \tag{4.2}$$

where $c_{13} = c_{33} - 2c_{44}$. The stiffness tensor, $\mathbf{C}$, contains two independent entries; c_{33} and c_{44} in an isotropic media that relate to compressional (v_p) and shear (v_s) velocities and density (ρ) as follows:

$$v_p = \sqrt{\frac{c_{33}}{\rho}}, \tag{4.3}$$

$$v_s = \sqrt{\frac{c_{44}}{\rho}}. \tag{4.4}$$

Therefore, it is customary to calculate c_{33} and c_{44} from compressional and shear logs in isotropic media.

4.1.2 VTI Media

Most hydrocarbon-bearing shales are described as VTI rocks because the elastic properties of the rock are symmetric about a vertical axis that is normal to bedding planes. In a VTI media, the stiffness tensor with Voigt's notation is expressed as

$$\mathbf{C} = \begin{bmatrix} c_{11} & c_{12} & c_{13} & 0 & 0 & 0 \\ c_{12} & c_{11} & c_{13} & 0 & 0 & 0 \\ c_{13} & c_{13} & c_{33} & 0 & 0 & 0 \\ 0 & 0 & 0 & c_{44} & 0 & 0 \\ 0 & 0 & 0 & 0 & c_{44} & 0 \\ 0 & 0 & 0 & 0 & 0 & c_{66} \end{bmatrix}, \tag{4.5}$$

where $c_{12} = c_{11} - 2c_{66}$. In a VTI media, the stiffness tensor, $\mathbf{C}$, contains five independent entries; c_{11}, c_{13}, c_{33}, c_{44}, and c_{66} that relate to compressional (v_p) and shear (v_s) velocities, and density (ρ) as follows:

$$v_{pv} = \sqrt{\frac{c_{33}}{\rho}}, \tag{4.6}$$

$$v_{sv} = \sqrt{\frac{c_{44}}{\rho}}, \tag{4.7}$$

$$v_{ph} = \sqrt{\frac{c_{11}}{\rho}}, \tag{4.8}$$

$$v_{sh} = \sqrt{\frac{c_{66}}{\rho}}, \tag{4.9}$$

$$v_{p45} = \sqrt{\frac{\frac{c_{11} + c_{33}}{2} + c_{44} + \sqrt{\frac{(c_{11} - c_{33})^2}{4} + (c_{13} + c_{44})^2}}{2\rho}}, \tag{4.10}$$

where the subscripts v and h denote the directions parallel and perpendicular to the vertical axis of symmetry, respectively, and v_{p45} is the P-wave velocity at an angle of 45 degrees from the axis of symmetry.

4.1.3 Estimating Stiffness Coefficients from Sonic Logs

In hydrocarbon-bearing shales, the ability to initiate and propagate hydraulic fractures correlates with stiffness coefficients of layers near well-bore region. Hence, estimating stiffness coefficients in VTI formations is necessary to calculate in-situ stresses in hydrocarbon reservoirs for drilling applications and production optimization. To determine formation stresses, stiffness coefficients are typically estimated using

effective-medium models calibrated to core data. However, effective-medium models are non-unique while core data analysis is scant and expensive. Other methods estimate three of the five independent stiffness coefficients from compressional, shear, and Stoneley slownesses. Because sonic tools introduce spatial averaging effects on logs, calculated coefficients from logs are averaged vertically over the length of the receiver array of acoustic instruments.

In this chapter, I develop an inversion-based algorithm to estimate stiffness coefficients of VTI formations using compressional, flexural/quadrupole, and Stoneley logs measured with wireline or LWD instruments. The inversion algorithm is performed in two sequential steps: (1) reduction of spatial averaging effects on compressional, flexural/quadrupole, and Stoneley logs and calculation of layer-by-layer slownesses, and (2) estimation of stiffness coefficients from the calculated layer-by-layer slownesses. To take advantage of the different sensitivities of borehole modes to stiffness coefficients and to improve the robustness of the inversion, I estimate the stiffness coefficients sequentially: First, I invert the compressional log and the low-frequency Stoneley log to calculate c_{33} and c_{66}, respectively. Then, I invert the quadrupole/flexural log at low frequencies to calculate c_{44}, and finally, I invert the quadrupole/flexural logs at higher frequencies to calculate c_{11} and c_{13}.

I implement the method with synthetic examples to assess its reliability and accuracy under controlled conditions. To construct the synthetic cases I only consider homogeneous and horizontally layered-formations penetrated by vertical wells, where layers are thinner than the length of the receiver array, varying between 0.60 m and 0.91 m, while Thomson's parameters vary within the range of values observed in organic

shales, i.e., $0.1<\varepsilon<0.3$, $0.09<\gamma<0.29$, and $0.04<\delta<0.11$ (Vernik and Liu, 1997; Tutuncu, 2010; Murphy et al., 2015). I observe three sources of error in the estimated coefficients: (a) bias error originating from de-averaging the logs prior to inversion, (b) error propagated during the sequential inversion, and (c) error associated with noisy slowness logs. It is found that the relative bias and uncertainty of the estimated coefficients is largest for c_{11} and c_{13} because borehole modes exhibit low sensitivity to these two coefficients. The main advantage of the method is that it mitigates spatial averaging effects of sonic logs in the estimated coefficients while at the same time yielding continuous estimations along the depth interval of interest.

4.2 FORWARD MODELING IN VTI FORMATIONS PENETRATED BY VERTICAL WELLS

In a homogeneous formation with a vector of elastic properties $\mathbf{p_0} = [c_{11}, c_{13}, c_{33}, c_{44}, \text{and } c_{66}]$, the sensitivity, $S_k^{\{l\}}$, of a sonic borehole mode $\{l\}$ to the elastic property p_{0k} is given by

$$S_k^{\{l\}}(\mathbf{p_0}, f) = \frac{\partial s^{\{l\}}(\mathbf{p_0}, f)}{\partial p_{0k}}, \tag{4.11}$$

where $s^{\{l\}}$ is slowness of mode $\{l\}$ at frequency f of a homogeneous formation whose stiffness coefficients are given by the vector $\mathbf{p_0}$ and p_{0k} is the k-th stiffness coefficient. Figure 4.1 and Figure 4.2 show the normalized sensitivity of the quadrupole and flexural modes calculated in slow and fast homogenous formations penetrated by LWD and wireline tools, respectively. The normalization factor is $s^{\{l\}}(\mathbf{p_0}, f)/p_{0k}$. Formation and borehole properties are given in Table 4.1, while the assumed tool properties are given in Table 4.2. In a layered formation (formation with horizontal thin beds penetrated by a

vertical borehole), the slowness of a sonic mode $\{l\}$ is given by equation 2.4 where $\mathbf{p_0} = [c_{11}, c_{13}, c_{33}, c_{44}, \text{and } c_{66}]$.

4.3 INVERSION-BASED INTERPRETATION WORKFLOW

I perform inversion-based interpretation of borehole sonic logs in two steps: in the first step, I mitigate spatial averaging effects on the borehole sonic logs to obtain layer-by-layer slownesses of formations, while in the second step, I estimate stiffness coefficients from the calculated layer-by-layer slownesses.

Inversion Step 1

In *Step 1* of the inversion method, I mitigate spatial averaging effects on frequency-dependent (dispersive) and non-dispersive (compressional) sonic logs introduced by acoustic instruments when calculating layer-by-layer slownesses. This is accomplished by minimizing the quadratic cost function given by

$$e_1(\mathbf{m}(f_i)) = \left\|\mathbf{F}\mathbf{m}(f_i) - \mathbf{d}_{\log}(f_i)\right\|_2^2 + \alpha^2\|\mathbf{\Lambda}\mathbf{m}(f_i)\|_2^2\,, \qquad 4.12$$

at each frequency f_i, where $\mathbf{m}(f_i)$ is the model vector whose components $m_k(f_i)$ are the slownesses at depth z_k and frequency f_i; $\mathbf{d}_{\log}(f_i)$ is the data vector whose component $(d_{\log}(f_i))_j$ is the slowness log at frequency f_i and measured depth d_j (z denotes any position in the formation, d denotes depth of the log), and $\mathrm{F}_{jk} = F(z_k - d_j)$ is the value of the spatial averaging function F (equation 2.15) at position z_k when the receiver array is centered at depth d_j. The second additive term of the cost function (equation 4.12) is a Tikhonov regularization (stabilization) term, where α is the regularization parameter and $\mathbf{\Lambda}$ is a regularization weighting matrix; when layers are thicker than the FWHM of the function F I do not implement regularization, i.e. I set $\alpha = 0$.

Bed boundaries and the initial guess of model properties are input to the inversion as follows:

- In synthetic cases, locations of bed boundaries are known while for field data they are estimated from other well logs (e.g., gamma ray, density, or resistivity).
- The initial guess of model properties for each layer is chosen as the mean value of the corresponding well log (e.g., density, slowness) across that layer.

To minimize the quadratic cost function (equation 4.12), I use the Levenberg-Marquardt method (Aster et al., 2005). In the examples of this chapter I do not use regularization, thus, $\alpha = 0$ and the gradient of the cost function becomes

$$\frac{\partial e_1(\mathbf{m}(f_q))}{\partial m_k} = \frac{\partial \left\| F(z_j - d_i) m_j(f_q) - (d_{\log}(f_q))_i \right\|_2^2}{\partial m_k}, \tag{4.13}$$

where f_q is frequency, $(d_{log})_i$ is slowness data at measured depth d_i, and m_j is slowness of the layer at depth z_j. Simplifying equation 4.13 yields

$$\frac{\partial e_1(\mathbf{m}(f_q))}{\partial m_k} = 2\left(F_{ij} m_j(f_q) - (d_{\log}(f_q))_i\right) F_{ik}, \tag{4.14}$$

whereby the entries of the Jacobian matrix **J** are given by $J_{ij} = F_{ij} = F(z_j - d_i)$.

Inversion Step 2

In *Step 2* of the inversion method, I calculate stiffness coefficients of layers from the layer-by-layer, frequency-dependent slownesses obtained in *Step 1*. This is accomplished by minimizing the quadratic cost function given by

$$e_2(\mathbf{p}_k) = \|\mathbf{g}(\mathbf{p}_k) - \mathbf{s}_k\|_2^2\,, \tag{4.15}$$

separately for each layer k, where $\mathbf{p}_k$ is the model vector of layer k whose entries are the five stiffness coefficients, $\mathbf{s}_k$ is the slowness vector at all frequencies f_q in a given layer k; i.e. $(\mathrm{s}_q)_k = m_k(f_q)$, and $\mathbf{g}(\mathbf{p}_k)$ is the modeled slowness vector calculated using 1D simulations. To minimize the quadratic cost function (equation 4.15) I use the Levenberg-Marquardt method (Aster et al., 2005) and calculate the entries of the corresponding Jacobian matrix using 1D simulations.

To improve the efficiency of the inversion, I implement equation 4.15 in the following way: First, I use the compressional mode to estimate c_{33} from $c_{33} = {v_{pv}}^2\rho$, where v_{pv} is the vertical compressional velocity obtained from the compressional log and ρ is density (known or obtained from the density log). Next, I use the Stoneley mode at low frequencies to calculate c_{66} given that $S_k^{\{st\}}(\mathbf{p_0}, f < 2\text{ kHz}) \approx 0$ for all p_{0k} except c_{66}. Then, I use the low-frequency component of the flexural/quadrupole modes to estimate c_{44} given that $S_k^{\{fl\}}(\mathbf{p_0},\ f \leq 3\text{ kHz}) \approx 0$ and $S_k^{\{q\}}(\mathbf{p_0},\ f \leq 4\text{ kHz}) \approx 0$ for all p_{0k} except c_{44} (see Figure 4.1 and Figure 4.2). Finally, I invert the flexural/quadrupole log at higher discrete frequencies to estimate c_{11} and c_{13} because the ratios $S_{c44}^{\{fl\}}(\mathbf{p_0},\ f > 4\text{ kHz})/S_{c33\text{ or }c13}^{\{fl\}}(\mathbf{p_0},\ f > 4\text{ kHz})$ and $S_{c44}^{\{q\}}(\mathbf{p_0},\ f > 4\text{ kHz})/S_{c33\text{ or }c13}^{\{q\}}(\mathbf{p_0},\ f > 4\text{ kHz})$ decreases when frequency increases. In all the examples, the inversion is initialized assuming that the formation is isotropic. I use a total of 14 well logs to perform the sequential inversion, as follows:

- One compressional log (to estimate c_{33}).

- One Stoneley log (to estimate c_{66}). The frequency is determined from the Stoneley dispersion curve at the lowest frequency with constant slowness, usually between 1 kHz and 2 kHz.
- One flexural/quadrupole log at low frequency (to estimate c_{44}). For the flexural mode, the frequency is chosen at the point where the dispersion curve asymptotes to a constant value, usually between 2 kHz and 3 kHz. For the quadrupole mode, the low frequency is chosen around the cut-off frequency at approximately 3.5 kHz for slow/intermediate formations and 4.5 kHz for fast formations (Su et al., 2013; Matuszyk and Torres-Verdín, 2014).
- Eleven discrete frequencies from 4.5 kHz to 7 kHz (to estimate c_{11} and c_{13}).

Although I use discrete frequencies for the inversion, continuous frequencies can be used if the measurement is noisy to increase the signal-to-noise ratio. The sampling depth interval of well logs is 0.5 ft. Table 4.3 describes the inversion process.

4.4 RESULTS

I apply the inversion method to three synthetic examples logged with LWD instruments. Synthetic quadrupole, Stoneley, and P-wave slownesses are generated using two-dimensional finite-element (2DFE) and finite-difference (2DFD) numerical simulations. In Example 1, I use sequential inversion to estimate the stiffness coefficients of an intermediate homogeneous formation. Example 2 includes a thin layer within the homogeneous formation with the intent of showing how spatial averaging effects intrinsic to sonic logs can bias the estimated coefficients. Example 3 applies the method to a fast formation that includes a high degree of anisotropy, thin layers (thinner than the length of the receiver array), and large contrast of slownesses (up to 20%) between adjacent layers

with the intent of examining the effects of spatial averaging of sonic logs and formation type on the estimated coefficients. Table 4.4 describes the synthetic examples and summarizes the parameters used for inversion (i.e., frequency, number of logging points, type of tool, and type of formation).

4.4.1 Example 1 – Homogeneous Formation

First, I consider the simple case of a homogeneous VTI formation logged with an LWD instrument to validate the inversion workflow followed in the estimation of stiffness coefficients (*Step 2*, Table 3). Figure 4.3 shows the frequency-dependent slownesses and the stiffness coefficients of the formation in black, of the initial guess in blue, and of the estimations in red. The difference between actual and inverted coefficients, e, varies between 0.03 GPa and 1.14 GPa (equivalent to 0.3% and 9% relative error); e is largest for c_{13} because the quadrupole mode exhibits low sensitivity to this coefficient (see Figure 4.1). I conclude that the proposed method accurately estimates c_{11}, c_{33}, c_{44}, and c_{66} in a homogeneous formation with noise-free measurements which are also devoid of spatial averaging effects, and that the estimation of c_{13} is biased because of low measurement sensitivity.

4.4.2 Example 2 – Layered Formation

The objective of this example is (1) to validate the inversion workflow to mitigate spatial averaging effects on well logs (*Step 1*) and (2) to show the effect of spatial averaging and measurement noise on the estimated coefficients. Therefore, I include a thin layer within the homogeneous formation of Example 1. The log interval is 3 m, corresponding to 21 logging points. Figure 4.4 shows the frequency-dependent, synthetic

borehole sonic logs in black and the true layer-by-layer slownesses with black dashed lines. Spatial averaging effects on synthetic borehole logs are mitigated by applying *Step 1* of the inversion method and calculating layer-by-layer slownesses (blue dashed lines). Error bars superimposing the logs were calculated by adding zero-mean Gaussian noise with 0.4 μs/ft standard deviation to the input logs (blue circles) and applying the inversion method several times with the same initial guess but different instances of noise. Error bars indicate the 95% confidence interval of inverted slownesses (Figure 4.4). Each inversion (*Step 1*) converges in less than five iterations and is completed within a few seconds of CPU time.

I use the value of the inverted frequency-dependent quadrupole, Stoneley, and compressional slownesses (blue dashed lines) of each layer, individually, to calculate stiffness coefficients using the method described in Table 4.3. Figure 4.5 shows the estimated c_{11}, c_{13}, c_{33}, c_{44}, and c_{66} with blue dashed lines while Table 4.4 summarizes the parameters used for inversion.

The distribution of the error of the estimated stiffness coefficients shows a bias, caused by both the de-averaging process and the propagation of error on the stiffness coefficients during sequential inversion. The standard deviation of the error distribution of the stiffness coefficients, σ_{c_k}, depends on the standard deviation of the measured slowness, σ_s. As a first-order approximation, I can quantify the error, Δc_k, in estimating stiffness coefficient c_k in terms of the errors, $\Delta s(f_i)$, of the estimated slowness s at frequency f_i using equation 4.11

$$\Delta s(f_i) = \sum_k S_k(f_i)\Delta c_k, \tag{4.16}$$

where S_k is the sensitivity of mode slowness to c_k. Writing equation 4.16 in matrix form yields

$$\Delta\mathbf{s} = \mathbf{S}\Delta\mathbf{c}. \tag{4.17}$$

An error in $\Delta\mathbf{s}$ can be propagated to an error in $\Delta\mathbf{c}$ using the covariance matrix $\mathbf{cov}(\Delta\mathbf{c})$. The standard deviation of the stiffness coefficients are approximated from the diagonal elements of $\mathbf{cov}(\Delta\mathbf{c})$, which is given by (Aster et al., 2005):

$$\mathbf{cov}(\Delta\mathbf{c}) = (\mathbf{S}^t\boldsymbol{\Sigma}^{\mathbf{2}}\mathbf{S})^{-1}, \tag{4.18}$$

where $S_{ij} = S_j(f_i)$, $\Sigma_{ij} = \mathrm{diag}(1/\sigma_{s(f_i)})$, $\sigma_{s(f_i)}$ is the standard deviation of the error of the inverted slowness at frequency f_i (obtained from *Step 1*), and the superscript t denotes matrix transpose. The standard deviation, σ_{c_k}, of the error of the estimated coefficient is given by,

$$\sigma_{c_k} = (\mathbf{S}^t\boldsymbol{\Sigma}^{\mathbf{2}}\mathbf{S})^{-\mathbf{1}}_{kk}. \tag{4.19}$$

The columns 'Data' and 'Coefficient to Estimate' of Table 4.3 define s and c_k, respectively, for every step of the sequential inversion. In Figure 4.5, error bars indicate the 95% confidence interval of estimated coefficients (equal to $3.92\sigma_{c_k}$).

Table 4.5 describes the relative bias and the maximum standard deviation of the error on the estimated coefficients. Larger error bars and misfits are observed for the estimations of c_{11} and c_{13} compared to c_{44} because the sensitivity of the quadrupole mode to c_{11} and c_{13} is low.

4.4.3 Example 3 – Fast Heterogeneous Formation

In this example, I show that (1) spatial averaging biases the estimated coefficients, (2) sequential inversion provides better estimates of stiffness coefficients than simultaneous inversion, and (3) de-averaging the well logs prior to inversion improves the estimation of coefficients.

I construct a synthetic model with a degree of slowness anisotropy varying between 0.05% and 17%. Layer thicknesses are smaller than the length of the receiver array while the difference between the shear slowness of consecutive layers is on average 22 μs/ft. The sampling interval is 0.5 ft, and the depth interval is 11 m (69 logging points). Because layers are thin and the slowness contrast between consecutive layers is large (up to 20%), sonic logs exhibit spatial averaging. I mitigate spatial averaging by applying *Step 1* of the inversion-based method. Figure 4.6 shows the inverted frequency-dependent slownesses in blue, while the error bars superimposing the logs are calculated by adding zero-mean Gaussian noise with 0.4 μs/ft standard deviation to the modeled logs and applying the inversion method several times with the same initial guess but different instances of noise. Results confirm that de-averaging the well logs improves the estimation of slowness in the vicinity of layer boundaries. I estimate the stiffness coefficients using sequential and simultaneous inversion and calculate the ratio of relative errors. Figure 4.7 shows the estimated stiffness coefficients (blue dashed lines) from the sequential inversion (*Step 2*), where error bars indicate the 95% confidence interval of the estimations.

Table 4.5 summarizes the maximum relative bias and the standard deviation of the estimated coefficients. Figure 4.8 compares the estimated coefficients from the

sequential inversion (blue dashed lines) and the simultaneous (green dashed lines) inversion of coefficients c_{11}, c_{13} and c_{44} obtained using 11 quadrupole logs at discrete frequencies between 4.5 kHz and 7 kHz while Table 4.6 summarizes the ratio of the relative errors. The average ratio is larger than 1 for c_{11} and c_{13} estimates. Therefore, the sequential inversion procedure improves the estimation of c_{11} and c_{13} compared to simultaneous inversion because the sensitivity of the quadrupole mode to c_{44} at $f > 4.5$ kHz is 2 to 4 times larger than the sensitivity to c_{11} and c_{13} (Figure 4.1).

To show the impact of de-averaging well logs prior to inversion, I estimate the stiffness coefficients with and without de-averaging and calculate the ratio of relative errors. Figure 4.8 shows the estimated coefficients (red dots) obtained when I invert the slowness of the input well logs at the center of each layer. Table 4.7 summarizes the ratio of the relative errors and shows that the average value of the ratio is > 1. Therefore, de-averaging well logs prior to inversion improves the estimation of coefficients to more accurately reproduce the actual elastic properties of formations. However, in this example, the ratio remains smaller than 1 for the estimation of c_{11} because of biasing introduced by the sequential inversion.

4.5 DETECTING ANISOTROPY IN VERTICAL WELLS

A conventional method used to detect anisotropy in rock formations logged with acoustic wireline tools is to compare the flexural slownesses measured with orthogonal dipoles; differences between flexural slowness measured with orthogonal dipoles can indicate the presence of elastic anisotropy. However, flexural slownesses measured at low frequencies with orthogonal dipoles are equal in VTI formations penetrated by vertical wells; fast shear slownesses equal slow shear slownesses (Sinha et al., 1994).

I propose an alternative workflow to detect VTI anisotropy in layers penetrated by vertical wells. First, I calculate flexural logs assuming that the formation is isotropic; the parameters needed for that are rock density, c_{44} and c_{33} that I obtain from the density log, the low-frequency flexural log, and the compressional log, respectively. Next, I analyze the data residuals between calculated and measured flexural slownesses. A bias in data residuals will indicate that the formation is anisotropic.

I apply the above workflow to the formation described in Example 2 logged with a wireline tool. A dipole source is used to acquire the flexural logs while a monopole source is used to acquire the compressional, and Stoneley logs. Figure 4.9 shows the input frequency-dependent sonic logs and the inverted layer-by-layer slownesses obtained from *Step 1* of the inversion method. First, I assume that the formation is isotropic and estimate c_{44}, and c_{33} from the low-frequency flexural and compressional slownesses, respectively; next, I forward model the flexural logs. Figure 4.10a compares the input flexural logs (synthetic logs) to the modeled flexural logs while Figure 4.10b shows the histogram of data residuals between input and modeled flexural logs. The histogram shows a biased distribution of data residuals, thereby indicating that the formation is not isotropic. Therefore, to reduce biases in data residuals, I perform the inversion assuming that the formation is VTI. I estimate the five stiffness coefficients using *Step 2* of the inversion-based method. Figure 4.11a compares the input flexural logs to the flexural logs calculated from the inversion while Figure 4.11b shows the histogram of data residuals. The histogram approximates a Gaussian distribution centered at zero and has a 95% confidence interval of 1.46 μs/ft; it is therefore concluded that the formation is better described with vertically transversely isotropic layers. Figure 4.12

shows the estimated stiffness coefficients obtained from *Step 2* of the inversion method while Table 4.5 describes the maximum relative bias and the standard deviation of the error in the estimated coefficients.

I conclude that the analysis of data residuals can be used to detect anisotropy in formations. However, it is remarked that in practice a biased distribution of data residuals could also indicate the presence of features not accounted for in the model such as orthorhombic anisotropy, dipping layers, washout, breakouts, or fractures, among others.

4.6 UNCERTAINTY OF INVERTED COEFFICIENTS

In the synthetic examples described above, I showed that the error in estimating c_{11} and c_{13} is larger than the error in estimating c_{33}, c_{44}, and c_{66}, for two main reasons: first, the sensitivity of the quadrupole/flexural modes to c_{11} and c_{13} is low (Figure 4.1); therefore, small errors in slowness (data) yield large errors in estimated c_{11} and c_{13} (I quantified this type of error by calculating the 95% confidence interval); second, because I use sequential inversion to estimate coefficients, the errors in the estimation of c_{44}, c_{66}, and c_{33} will propagate to and reduce the accuracy of estimated c_{11} and c_{13} (I quantified this type of error by calculating the relative bias between actual and inverted coefficients in Table 4.5).

I use sequential and not simultaneous inversion to estimate stiffness coefficients because flexural/quadrupole slownesses exhibit low sensitivity to c_{11} and c_{13}. Using simultaneous inversion introduces larger uncertainties on c_{11} and c_{13} especially in the presence of noisy slowness measurements. In the presence of noisy slowness measurements, rock physics conditions can be included in the inversion to constrain the estimated stiffness coefficients, e.g., $\gamma > 0$, $\varepsilon - \delta > 0$, $\delta \leq (2/(c_{33}/c_{44} - 1))$, and

$\delta \geq -1/2(1 - c_{44}/c_{33})$ where ε, γ, and δ are Thomsen's parameters (Thomsen, 1986; Berryman et al., 1999; Spikes, 2014; Yan et al., 2016).

The method assumes that bed-boundary locations are known. Errors in the location of bed boundaries will induce errors in *Step 1* of the inversion method. If the locations of bed boundaries are not known, beds can be positioned at the log sampling points. Because layer thicknesses (dictated by the log sampling points) are smaller than the FWHM of the axial sensitivity function, stabilization is required for inversion (i.e., $\alpha > 0$) . However, inverted logs will approach the measured (data) logs; therefore, applying *Step 2* is equivalent to applying the method on the measurements slowness data as I showed in Example 3. Additional sources of errors unaccounted for in this chapter are the presence of near wellbore damage or washouts that impact the flexural and quadrupole modes at high frequencies. Furthermore, the method assumes that the density and velocity of the borehole fluid are known beforehand. Uncertainties in the velocity of the borehole fluid induce errors in the estimated c_{66} from the Stoneley log.

Finally, the proposed inversion method is only applicable to slowness measurements acquired in vertical wells penetrating horizontal layers; it remains to be examined whether small layer dips could have a measurable impact on the estimated coefficients. The method can be applied to horizontally transversely isotropic formations provided that the formation is drilled with a horizontal well.

4.7 ESTIMATING SHEAR SLOWNESSES FROM LOGS

Calculating shear slownesses (or c_{44}) from quadrupole logs is challenging because the low-frequency components of the quadrupole mode are smaller than the true formation shear slowness (Scheibner et al., 2010). Figure 4.13 shows the synthetic

quadrupole logs of Examples 2 and 3 where I superimpose the true layer shear slownesses in black. The low frequency quadrupole does not asymptote to shear slowness and cannot be used to reliably estimate c_{44}. Therefore, I calculate shear slowness (ss_v) from $ss_v = \sqrt{\rho/c_{44}}$ where c_{44} is estimated from *Step 2* of the inversion method (see estimated c_{44} in Figure 4.5 and Figure 4.7). Figure 4.13 shows the values of ss_v in red where the relative estimation error is within 3%. Therefore, the inversion-based method can be used to estimate layer-by-layer shear slownesses of formations from the low-frequency quadrupole slowness.

4.8 SUMMARY AND CONCLUSIONS

I showed that forward modeling and inversion of frequency-dependent borehole sonic logs measured with wireline and LWD tools could be used to calculate the stiffness coefficients of VTI layers. It was verified that the inversion-based interpretation method yields accurate estimations of c_{33}, c_{44}, and c_{66} in VTI formations while reducing spatial averaging effects on slowness logs. Inversion results exhibit larger uncertainties when estimating c_{11} and c_{13} because the sensitivity of sonic modes to these two coefficients is low. However, when measurements are noise-free and mitigated for spatial averaging effects, the inversion method yields reliable estimates for c_{11} and c_{13}.

To mitigate spatial averaging effects on sonic logs, I use the spatial averaging function (F) to forward model sonic logs in a few seconds of CPU time. Additionally, the method estimates layer-by-layer shear slownesses from quadrupole logs and estimated stiffness coefficients are available across the entire depth interval of study.

4.9 TABLES AND FIGURES

Table 4.1: Summary of the assumed elastic properties of borehole fluid and rock formations.

	Borehole	**Slow Formation**	**Fast Formation**
$\boldsymbol{\rho}$ **(kg/m^3)**	1000	2500	2500
$\boldsymbol{c_{11}}$ **(GPa)**	2.25	23.04	43.56
$\boldsymbol{c_{13}}$ **(GPa)**	2.25	5.95	9.76
$\boldsymbol{c_{33}}$ **(GPa)**	2.25	14.40	27.22
$\boldsymbol{c_{44}}$ **(GPa)**	0	4.90	10.0
$\boldsymbol{c_{66}}$ **(GPa)**	0	6.86	14.0

Table 4.2: Geometric properties assumed for the LWD and wireline instruments.

	LWD	**Wireline**
Number of receivers	12	8
Inter-receiver spacing (m)	0.1017	0.1524
Inner/outer radius (m)	0.0254/0.0857	NA/0.046

Table 4.3: Description of *Step 1* of the inversion method.

Step	**Coefficient to Estimate**	**Method**	**Data**	**Initial Guess of Coefficients** $c_{ij_{initial}}$	**Estimated Coefficient** $c_{ij_{final}}$
1	c_{33}	$c_{33} = {v_{pv}}^2\rho$	Compressional log	N/A	$c_{33_{final}}$
2	c_{66}	Minimize equation 4.15 using Levenberg-Marquardt	Stoneley log at low frequency	$c_{33_{initial}} = c_{33_{final}}$, $c_{11_{initial}} = c_{33_{initial}}$, $c_{44_{initial}}$ = quadrupole/flexural log at low frequency, $c_{66_{initial}} = c_{44_{initial}}$, $c_{13_{initial}} = c_{33_{initial}} - 2c_{44_{initial}}$.	$c_{66_{final}}$
3	c_{44}	Minimize equation 4.15 using Levenberg-Marquardt	Quadrupole/ Flexural logs at low frequencies	$c_{33_{initial}} = c_{33_{final}}$, $c_{66_{initial}} = c_{66_{final}}$, $c_{44_{initial}}$ = quadrupole/flexural log at low frequency, $c_{11_{initial}} = (2\varepsilon + 1)c_{33_{final}}$, $\varepsilon = \gamma = \frac{c_{66_{initial}} - c_{44_{initial}}}{2c_{44_{initial}}}$, $c_{13_{initial}} = c_{33_{initial}} - 2c_{44_{initial}}$,	$c_{44_{final}}$
4	c_{11} and c_{13}	Minimize equation 4.15 using Levenberg-Marquardt	Quadrupole/ Flexural logs at high frequencies	$c_{33_{initial}} = c_{33_{final}}$, $c_{66_{initial}} = c_{66_{final}}$, $c_{44_{initial}} = c_{44_{final}}$, $c_{11_{initial}} = (2\varepsilon + 1)c_{33_{final}}$, $\varepsilon = \gamma = \frac{c_{66_{initial}} - c_{44_{initial}}}{2c_{44_{initial}}}$, $c_{13_{initial}} = c_{33_{initial}} - 2c_{44_{initial}}$,	$c_{11_{final}}$ and $c_{13_{final}}$

Table 4.4: Parameters used during inversion in the synthetic examples examined in this chapter.

	Tool type	Formation type	Frequency of Stoneley log used to estimate c_{66}	Frequency of quadrupole/flexural log used to estimate c_{44}	Frequencies of quadrupole/flexural logs used to estimate c_{11} and c_{13}	Number of logging points
Example 1	LWD	Intermediate	1 kHz	3.5 kHz	4.5 kHz to 7 kHz	N/A
Example 2	LWD	Intermediate	1 kHz	3.5 kHz	4.5 kHz to 7 kHz	21
Example 3	LWD	Fast	1.5 kHz	4.5 kHz	4.5 kHz to 7 kHz	69
Example 4	Wireline	Intermediate	1 kHz	3 kHz	4.5 kHz to 7 kHz	21

Table 4.5: Relative bias and standard deviation of the error for the estimated stiffness coefficients in the synthetic examples examined in this chapter.

	Maximum relative bias for the estimated c_{33}, c_{44}, and c_{66}	Maximum relative bias for the estimated c_{11} and c_{13}	Maximum standard deviation of the error of estimated stiffness coefficients: $\sigma_{c_{ij}}$
Example 2	1.6%	15.9%	1.43 GPa
Example 3	6.75%	17.3%	3.86 GPa
Example 4	1.0%	16.2%	4.11 GPa

Table 4.6: Ratio of relative error (norm). Stiffness coefficients are estimated with simultaneous and sequential inversions when calculating the ratio of relative error.

	Ratio of relative error of estimated c_{11} and c_{13}	
	c_{11}	c_{13}
Layer 1	0.96	1.11
Layer 2	3.87	2.87
Layer 3	1.25	0.70
Layer 4	1.86	2.60
Layer 5	3.00	> 100
Layer 6	1.29	1.83
Layer 7	1.82	1.32
Layer 8	0.95	1.06
Layer 9	2.55	4.75
Layer 10	1.42	2.74
Layer 11	0.10	0.25

Table 4.7: Ratio of relative error (norm). Stiffness coefficients are estimated without and with de-averaging of well logs when calculating the ratio of relative error.

	Ratio of relative error of estimated c_{ij}				
	c_{11}	c_{13}	c_{33}	c_{44}	c_{66}
Layer 1	0.04	1.54	1.29	1.06	7.39
Layer 2	0.96	1.90	11.45	3.20	0.59
Layer 3	0.47	1.12	9.37	3.73	2.74
Layer 4	0.74	1.12	43.27	1.51	30.19
Layer 5	0.31	> 100	9.91	2.64	14.21
Layer 6	0.47	1.53	8.22	0.63	66.08
Layer 7	0.09	0.95	4.88	4.39	0.57
Layer 8	2.94	1.46	9.15	2.04	7.82
Layer 9	2.29	0.77	2.73	0.97	1.03
Layer 10	0.34	2.35	38.53	0.70	22.29
Layer 11	0.69	0.56	10.97	1.98	0.77

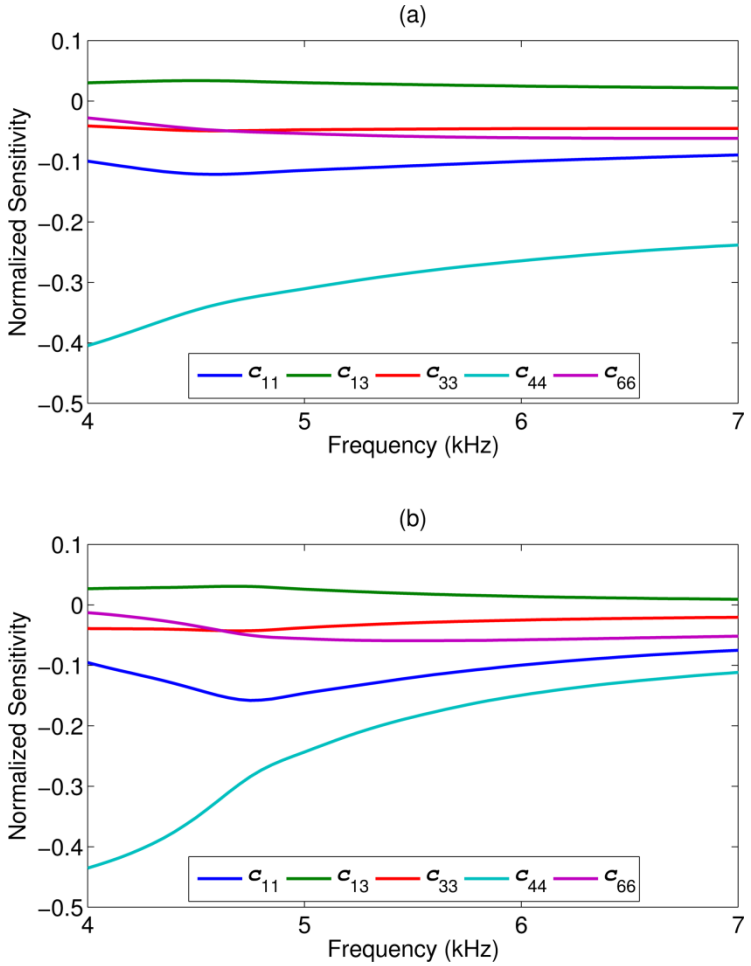

Figure 4.1: Normalized frequency-dependent sensitivity of the quadrupole mode to c_{11}, c_{13}, c_{33}, c_{44}, and c_{66}, for the (a) slow and (b) fast formations logged with an LWD instrument.

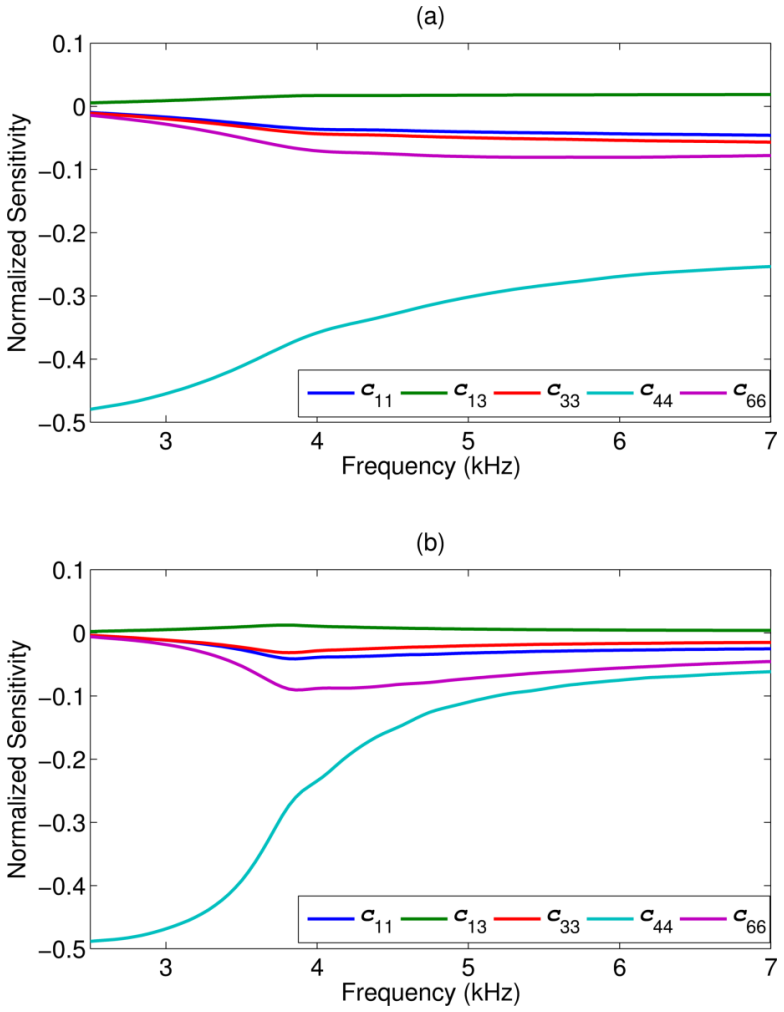

Figure 4.2: Normalized frequency-dependent sensitivity of the flexural mode to c_{11}, c_{13}, c_{33}, c_{44}, and c_{66}, for the (a) slow and (b) fast formations logged with a wireline instrument.

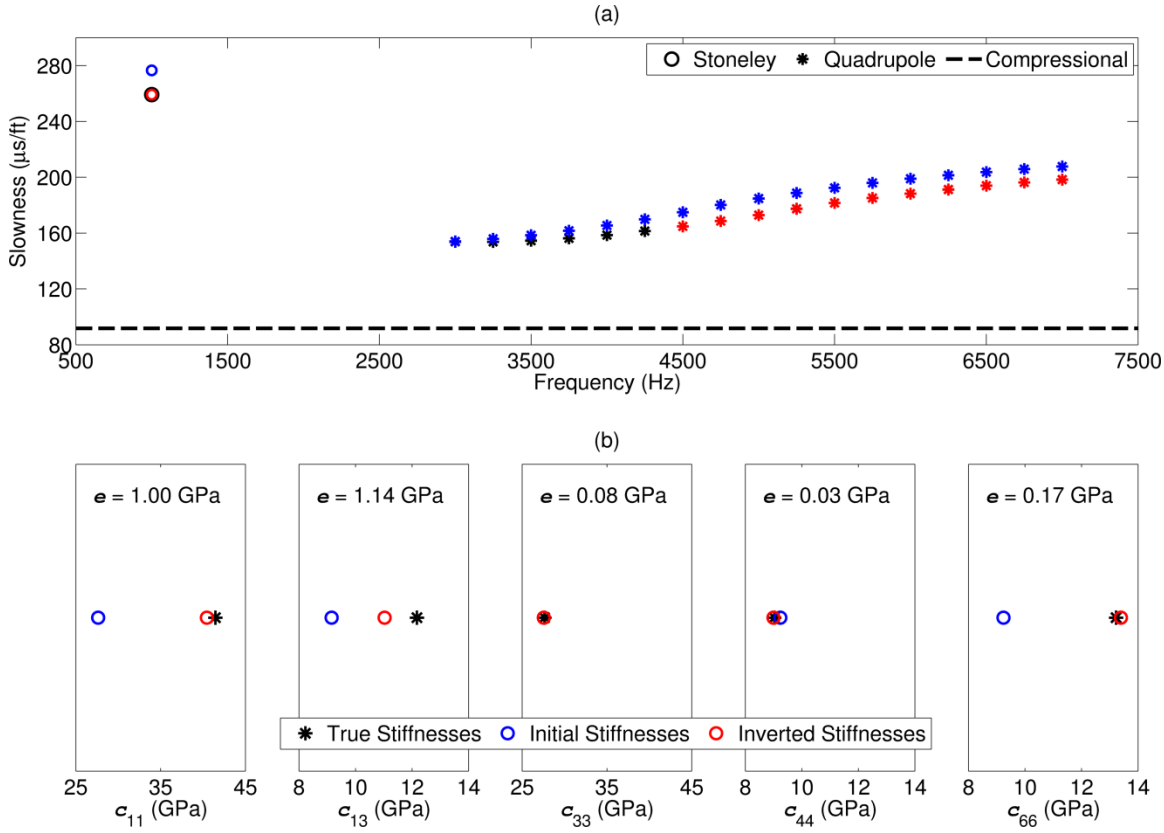

Figure 4.3: (a) Comparison of quadrupole, compressional, and Stoneley slownesses of a homogeneous formation (black) to inverted slownesses (red) obtained from the inversion (*Step 2*) method. Slownesses used to initialize the inversion are shown in blue. (b) Actual, initial, and inverted stiffness coefficients are shown in black, blue, and red, respectively. The error, e, between actual and inverted coefficients varies between 0.03 GPa and 1.14 GPa.

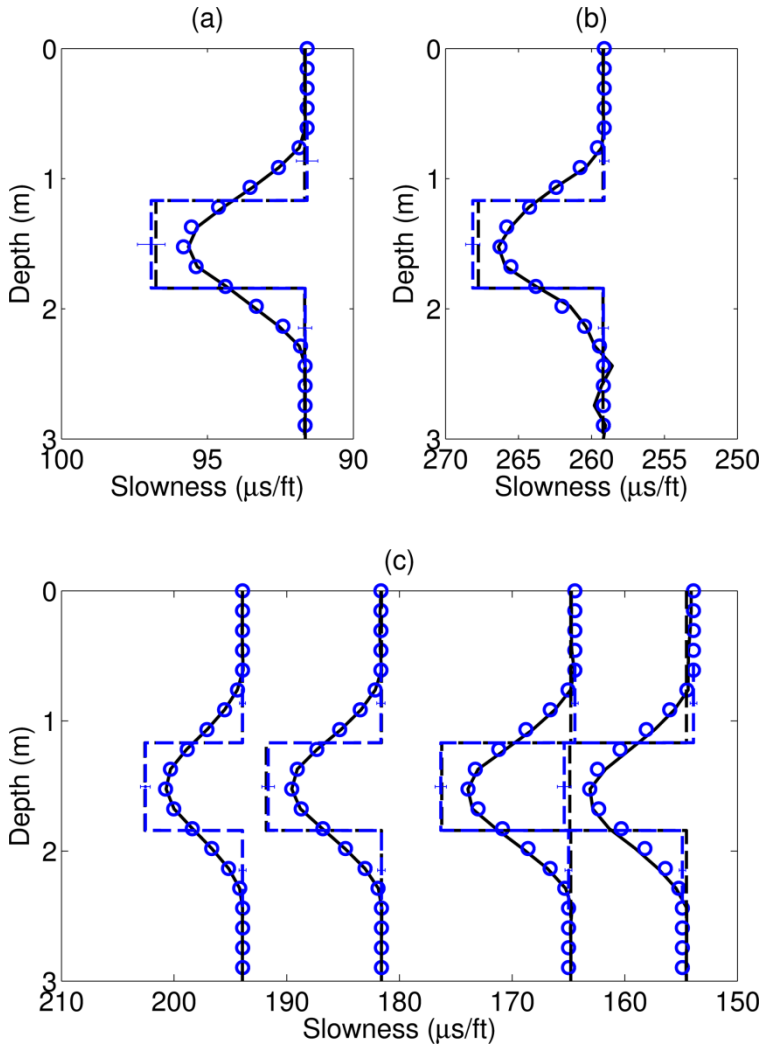

Figure 4.4: Comparison of input logs (black continuous lines) to modeled logs (blue circles) of the (a) compressional, (b) Stoneley at 1 kHz, and (c) quadrupole modes at 4 kHz, 5 kHz, 6 kHz, and 7 kHz (from right to left) for the VTI formation of Example 2 logged with an LWD instrument. Black dashed lines identify the actual slownesses of layers while blue dashed lines identify the slownesses obtained from *Step* 1 of the inversion method. Error bars superimposed to the inverted slownesses represent the 95% confidence interval.

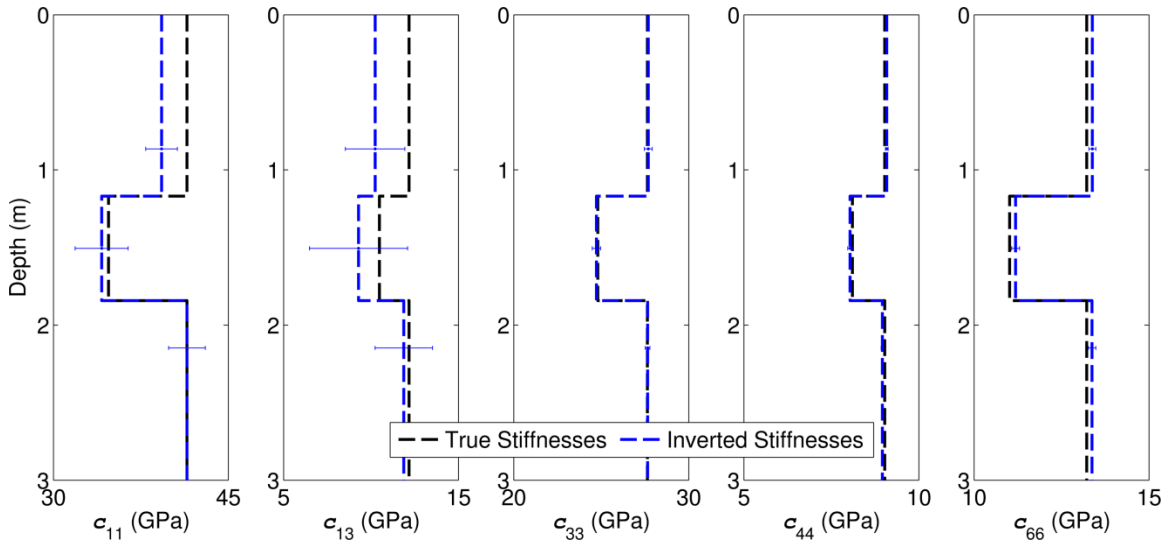

Figure 4.5: Comparison of actual rock stiffness coefficients (black) to inverted coefficients (blue) obtained with the inversion (*Step 2*) method applied to slowness data mitigated for spatial averaging effects (Figure 4.4). Error bars superimposed to the inverted stiffness coefficients represent the 95% confidence interval.

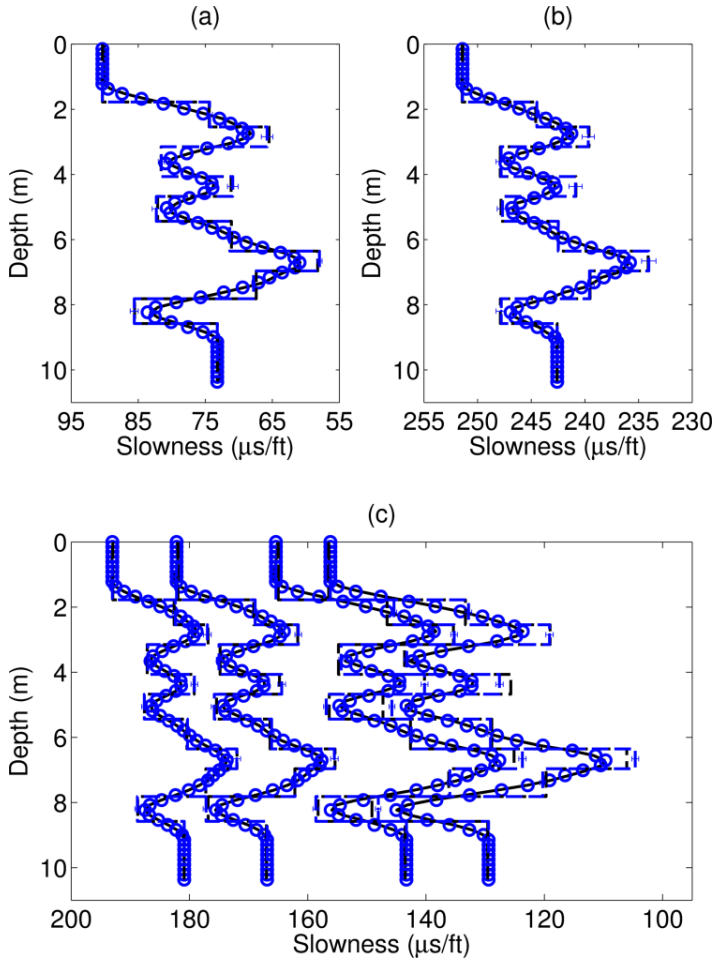

Figure 4.6: Comparison of input logs (black continuous lines) to modeled logs (blue circles) of the (a) compressional, (b) Stoneley at 1.5 kHz, and (c) quadrupole modes at 4.5 kHz, 5 kHz, 6 kHz, and 7 kHz (from right to left) for the VTI formation of Example 3 logged with an LWD instrument. Black dashed lines identify the actual slownesses of layers while blue dashed lines identify the slownesses obtained from *Step 1* of the inversion method. Error bars superimposed to the inverted slownesses represent the 95% confidence interval.

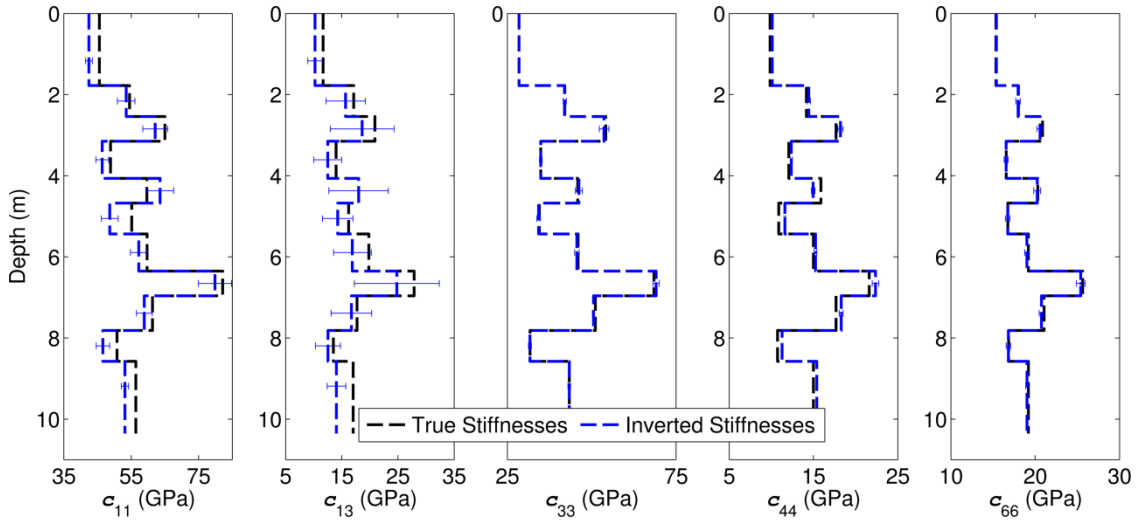

Figure 4.7: Comparison of actual rock stiffness coefficients (black) to inverted coefficients (blue) obtained from the inversion (*Step 2*) method applied to slowness data mitigated for spatial averaging effects (Figure 4.6). Error bars superimposed to the inverted stiffness coefficients represent the 95% confidence interval.

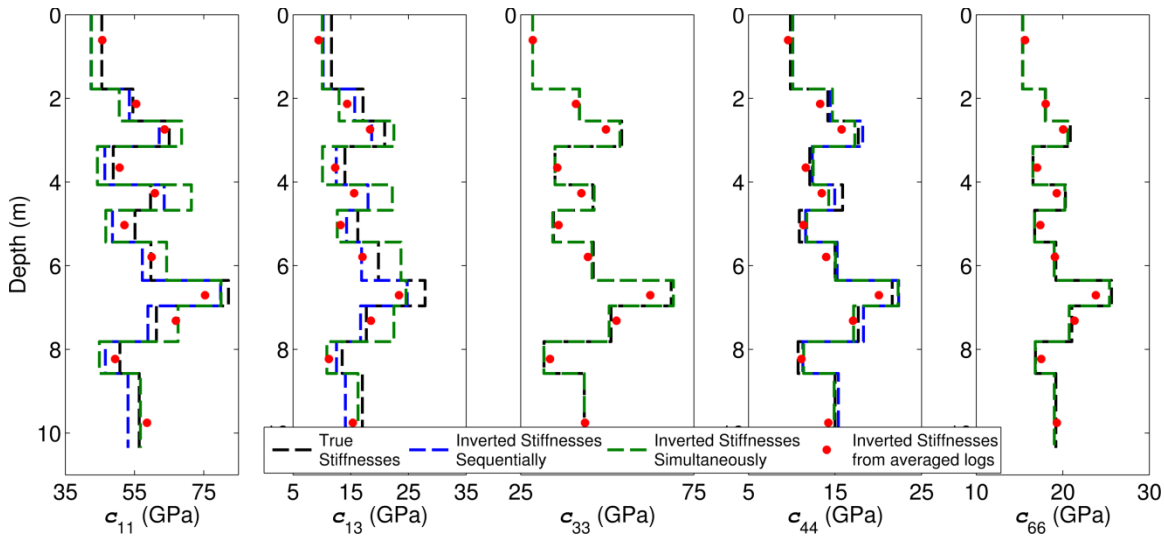

Figure 4.8: Comparison of actual rock stiffness coefficients (black) to inverted coefficients from the sequential (blue) and simultaneous (green) inversion. Red circles indicate the inverted slownesses obtained from the actual (averaged) logs.

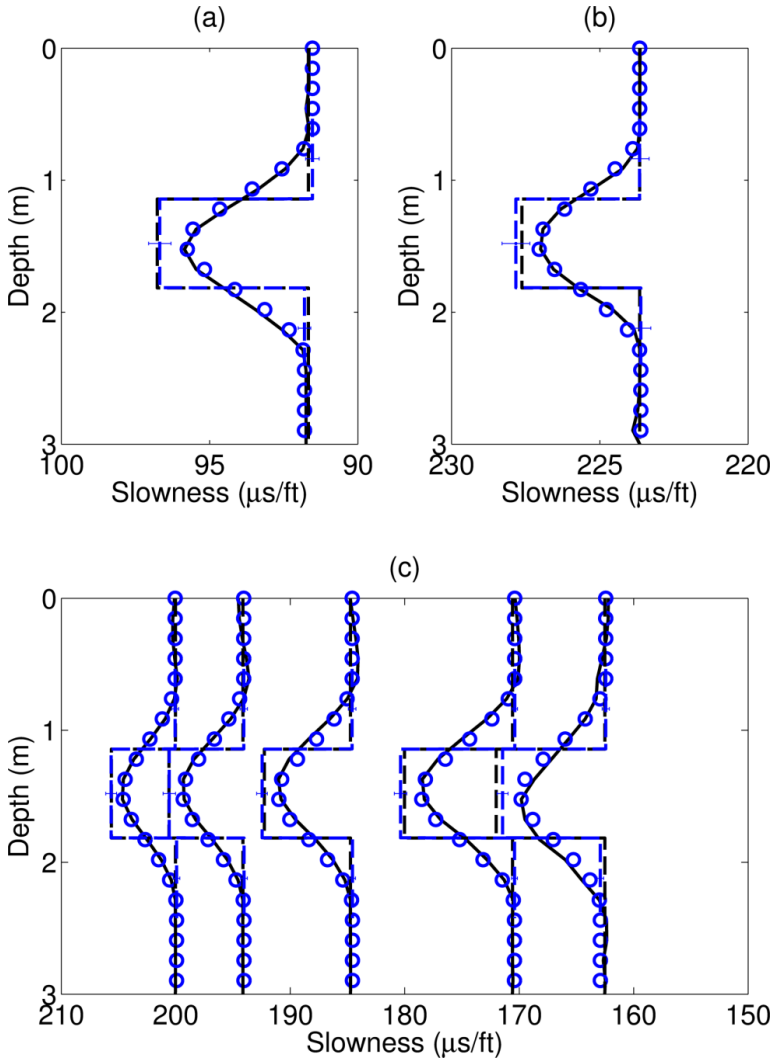

Figure 4.9: Comparison of input logs (black continuous lines) to modeled logs (blue circles) of the (a) compressional, (b) Stoneley at 1 kHz, and (c) flexural modes at 3 kHz, 4 kHz, 5 kHz, 6 kHz, and 7 kHz (from right to left) for the VTI formation logged with a wireline tool. Black dashed lines identify the actual slownesses of layers while blue dashed lines identify the slownesses obtained from *Step 1* of the inversion method. Error bars superimposed to the inverted slownesses represent the 95% confidence interval.

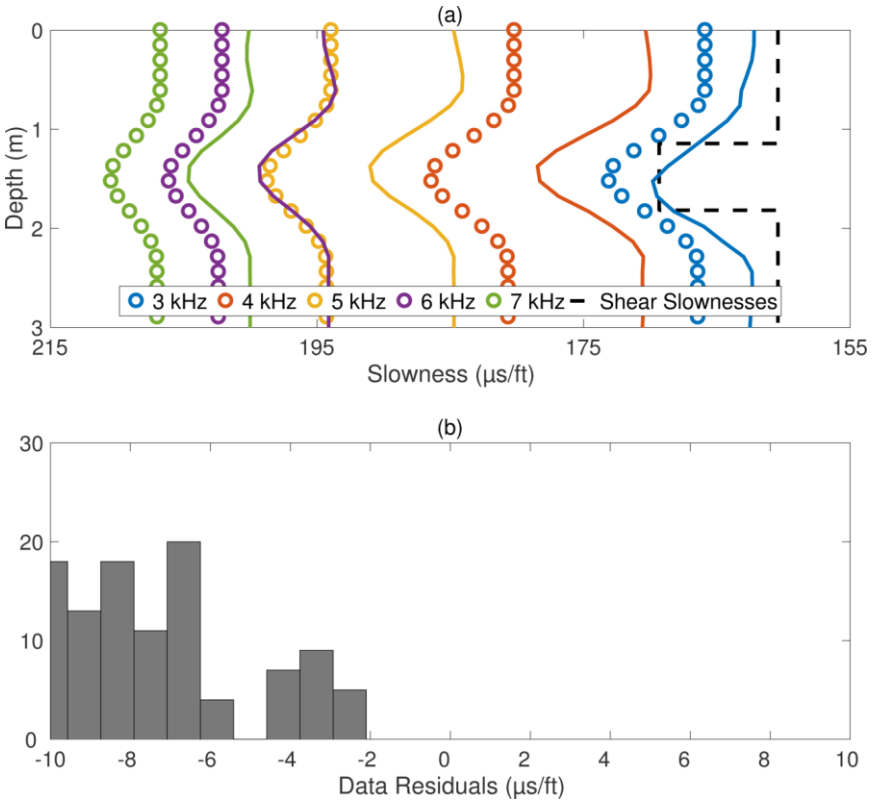

Figure 4.10: (a) Flexural logs at 3 kHz to 7 kHz measured with a wireline tool in the VTI formation (continuous lines) and modeled assuming that the formation is isotropic (circles). The actual vertical shear slownesses of layers are shown with black dashed lines. (b) Data residuals between input (continuous lines) and modeled flexural logs (circles).

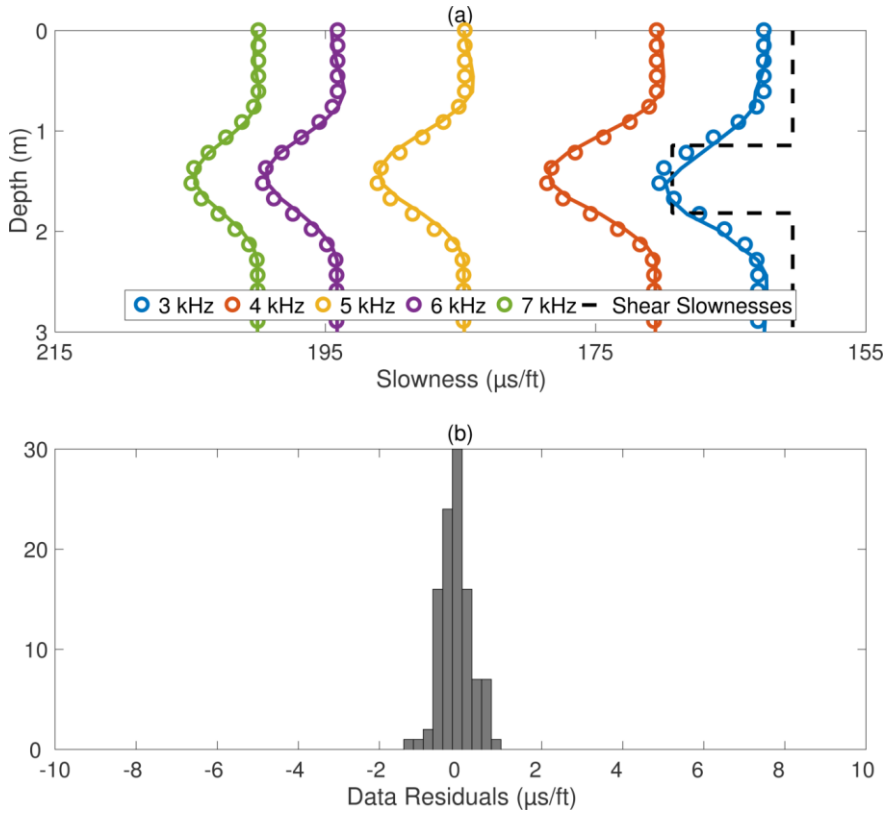

Figure 4.11: (a) Flexural logs at 3 kHz to 7 kHz measured with a wireline tool in the VTI formation (continuous lines) and modeled assuming that the formation is VTI (circles). The actual vertical shear slownesses of layers are shown with black dashed lines. (b) Data residuals between input (continuous lines) and modeled flexural logs (circles).

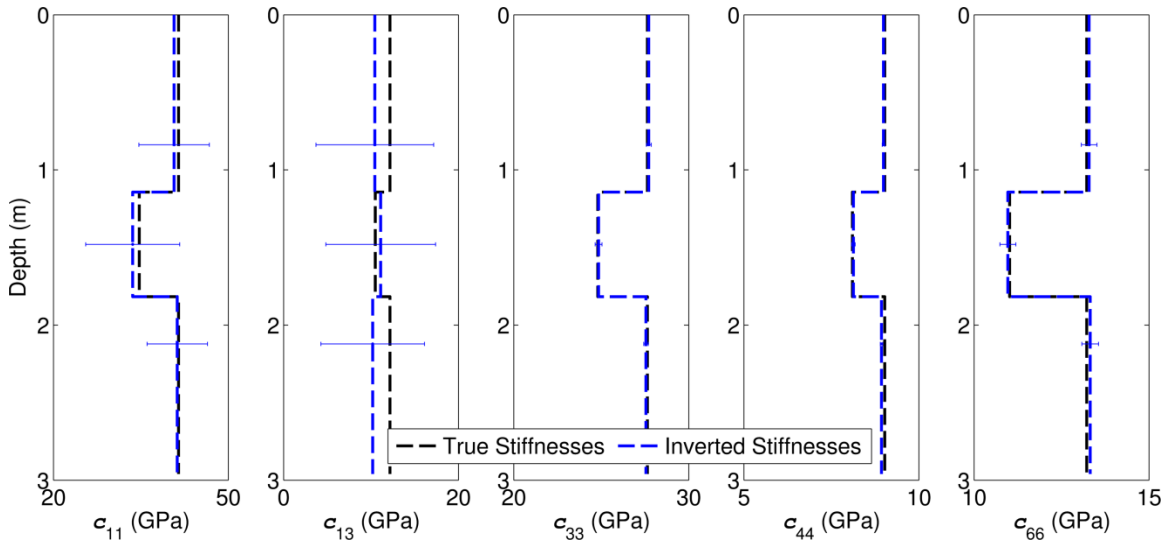

Figure 4.12: Comparison of actual rock stiffness coefficients (black) to coefficients (blue) obtained by applying the inversion (*Step 2*) method on the slowness data mitigated for spatial averaging effects (Figure 4.9). Error bars superimposed to the inverted stiffness coefficients represent the 95% confidence interval.

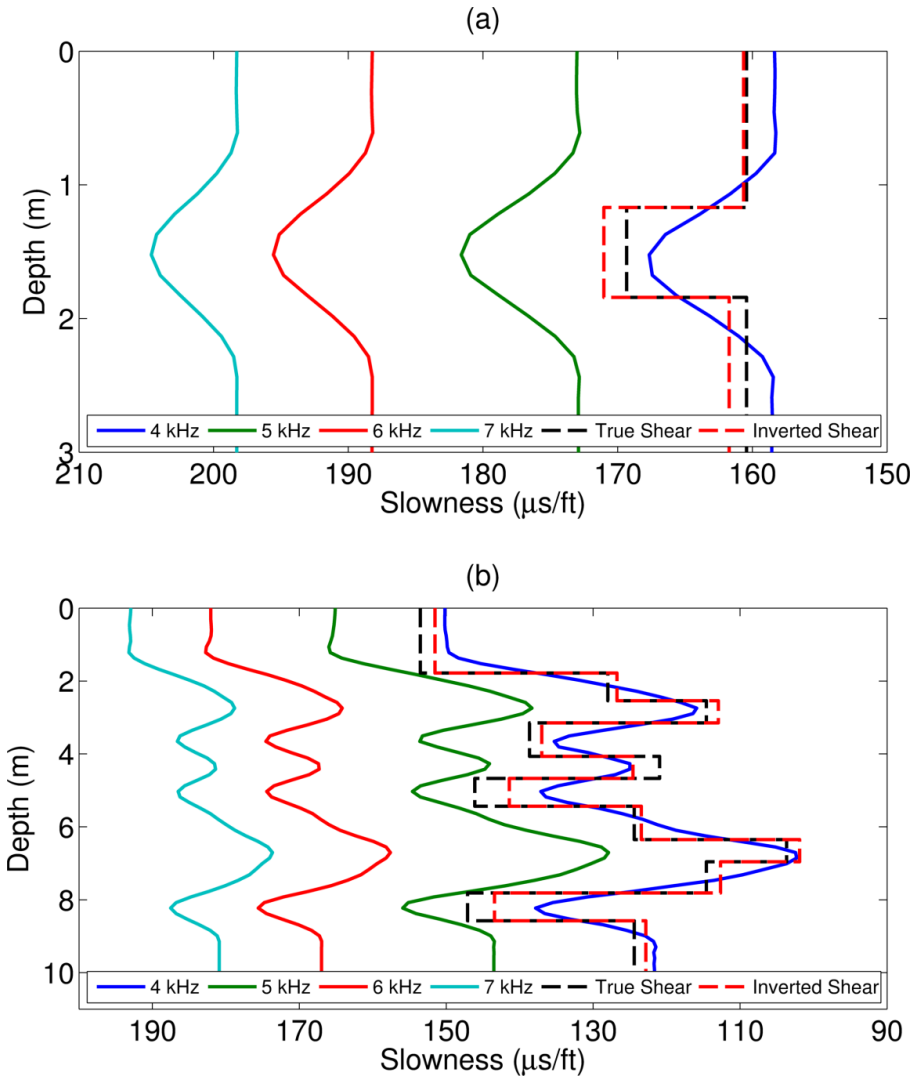

Figure 4.13: (a) Comparison of quadrupole logs of the formation of Example 2 to the actual (black) and estimated (red) shear slownesses of layers. (b) Comparison of quadrupole logs of the formation of Example 3 to the actual (black) and estimated (red) shear slownesses of layers.

Chapter 5: Fast-Forward Modeling of Borehole Sonic Dipole Modes in Isotropic and Transversely Isotropic Formations Penetrated by High-Angle Wells

In this chapter, I extend the rapid-modeling method to calculate flexural slownesses in rock formations penetrated by high-angle wells using 3D frequency-domain sensitivity functions. I calculate flexural logs acquired with cross dipoles in synthetic isotropic and VTI formations. Calculated flexural logs are compared to those simulated with a 3D-TDFD numerical simulations method. All 3D-TDFD simulations are run at the Texas Advanced Computer Center (TACC) in the Lonestar5 cluster, which hosts 1252 compute nodes. Each node in Lonestar5 is an Intel Xeon E5-2650 at 2.30 GHz, with 128 GB of RAM and with 10 cores per socket. All PC simulations are run on an office desktop computer with an Intel core i7 5820K at 3.30 GHz with 64 GB of RAM and 6 cores.

5.1 INTRODUCTION

Undulating wells are routinely drilled to improve reservoir exposure across hydrocarbon-bearing zones. Knowing the mechanical properties of the formation is therefore essential for geosteering applications. Although conventional acoustic-log interpretation methods are reliable in vertical wells, they often yield inaccurate results when applied to HA/HZ wells. In HA/HZ wells, for example, sonic logs are affected by non-symmetric spatial averaging around the borehole (Mallan et al., 2011), giving rise to biased estimations of elastic properties. In isotropic formations, spatial averaging effects induce differences between flexural slownesses measured with cross dipoles which can be falsely interpreted as effective anisotropy. Moreover, low-frequency dipole modes can

exhibit mode interference because acoustic waves are reflected at the boundaries of dipping layers, thereby biasing the estimation of layer shear slowness (Ellis and Singer, 2007). Furthermore, in VTI formations penetrated by a well that is not aligned with the symmetry axis, slownesses measured with cross dipoles at low frequency are affected by formation dip. Therefore, low-frequency flexural modes cannot be used to directly estimate layer shear slownesses.

Conventional methods to quantify and interpret sonic dipole measurements in formations penetrated by HA/HZ wells use 3D finite-difference or finite-element numerical simulations (Wang et al., 2002; Zheng et al., 2004; Byun and Toksöz, 2006). However, 3D numerical methods are CPU time and memory demanding. I develop a fast-forward modeling method to efficiently calculate flexural modes using linear spatial sensitivity functions in formations penetrated by high-angle wells. Spatial sensitivity functions are obtained from first-order linear perturbation theory and quantify variations of phase slowness measured by the sonic tool caused by local spatial perturbations of elastic properties.

Fast-forward modeling was previously introduced to accurately interpret sonic logs acquired in 1D (i.e., homogeneous formations) and 2D media (i.e., heterogeneous formations with horizontal layers) penetrated by vertical wells (Burridge and Sinha, 1996; Sinha et al., 2006b; Mallan et al., 2009). For example, Huang et al. (2015) constructed 2D axial-radial sensitivity functions to efficiently forward model flexural slownesses of 2D invaded-bedded formations penetrated by vertical wells. They showed that axial-radial sensitivities were accurately obtained from the product of 1D axial and 1D radial sensitivity functions.

In this chapter, I apply forward modeling using 3D spatial sensitivity functions to calculate borehole flexural slownesses in high-angle wells. Spatial sensitivity functions of flexural modes are efficiently calculated from the product of 1D axial, radial, and azimuthal sensitivity functions. The 3D forward model is the superposition of a reference background slowness (calculated in a homogeneous isotropic formation) and the convolution of a 3D spatial sensitivity function with layer-by-layer models of elastic properties.

The fast-forward modeling method is applied to synthetic examples to calculate dipole flexural slownesses of dipping isotropic and VTI formations with varying elastic properties. Modeled logs calculated with the 3D sensitivities are compared to actual logs obtained with a 3D-TDFD numerical simulation described and validated by Mallan et al. (2011), Ma et al. (2013), and Wang et al. (2017). In the remainder of this chapter, I refer to the flexural slownesses obtained from 3D-TDFD numerical simulations as *actual* logs, and to the flexural slownesses obtained using 3D spatial sensitivity functions as *modeled* logs. Sonic logs simulated with 3D sensitivity functions agree well with those obtained with 3D-TDFD simulations, with relative differences below 3%. Modeled sonic logs depend on the choice of a reference background; increasing the number of reference backgrounds, in general, improves flexural slowness estimations. Larger errors are observed for the low-frequency component of the flexural mode because (1) flexural logs are affected by the relatively low amplitude of the acoustic source pulse at low frequencies, (2) mode interference and reflection are more severe at low frequencies (Huang et al., 2013), and (3) limitations of the proposed forward modeling method. I compare the slownesses measured from orthogonal dipoles and observe two types of

anisotropy: (1) apparent (geometric) anisotropy when layers are thin, and the contrast of elastic properties between consecutive layers is large, and (2) effective anisotropy when layers are TI.

Three-dimensional spatial sensitivity functions are used to efficiently calculate slownesses of borehole guided waves, reducing CPU simulation time by at least two orders of magnitude compared to 3D-TDFD simulations. However, forward modeling using spatial sensitivity functions are not used to calculate P- and S-wave slownesses because bed boundaries strongly influence the propagation of P and S waves in HA/HZ wells (Wang et al., 2017). Alternative rapid modeling algorithms based on real-axis integration methods exist to calculate first-arrival compressional modes in HA/HZ wells (Huang and Torres-Verdín, 2017). Furthermore, the spectral method and the semianalytical finite-element method can be invoked to simulate borehole acoustic modes in formations with arbitrary anisotropy and spatial heterogeneities (Zharnikov et al., 2013). The latter techniques, however, are not discussed in this dissertation.

5.2 FORWARD MODELING FLEXURAL MODES

Three-dimensional frequency-domain spatial sensitivity functions quantify the variation of phase slowness of a borehole-guided wave caused by local changes of rock elastic properties in the radial (i.e., orthogonal to the borehole axis), axial (i.e., aligned with the borehole axis), and azimuthal directions. Using first-order approximation, the normalized (per unit volume) three-dimensional sensitivity functions $G_{3Dk}^{\{l\}}$ of an acoustic mode $\{l\}$ to a change in elastic property p_{0k} at volume element $\Delta V(r,z,\varphi) = r\Delta r\Delta z\Delta\varphi$ is given by

$$G_{3Dk}^{\{l\}}(r,z,\varphi,\mathbf{p_0},f)=\frac{s^{\{l\}}(r,z,\varphi,\mathbf{p},f)-s^{\{l\}}(r,z,\varphi,\mathbf{p_0},f)}{(p_k-p_{0k})r\Delta r\Delta z\Delta\varphi}, \quad 5.1$$

where $s^{\{l\}}(r,z,\varphi,\mathbf{p_0},f)$ is the slowness of a homogeneous reference background whose elastic properties are given by the vector $\mathbf{p_0}=[ss,sp,\rho]$, where ss is shear slowness, sp is compressional slowness, and ρ is density; $s^{\{l\}}(r,z,\varphi,\mathbf{p},f)$ is slowness of the formation at frequency f measured by the acoustic tool where a volume $r\Delta r\Delta z\Delta\varphi$ with elastic properties $\mathbf{p}$ is inserted and centered at position (r,z,φ) in the presence of a reference homogeneous formation. Figure 5.1 shows the cylindrical system of coordinates assumed in this chapter.

Calculating $G_{3Dk}^{\{l\}}$ from equation 5.1 requires CPU-intensive 3D numerical simulations. A single run of the 3D-TDFD on a Lonestar5 core takes approximately 30 CPU minutes. Because the typical grid dimensions used to calculate $G_{3Dk}^{\{l\}}$ via 3D-TDFD simulations are $500\times500\times99$ in the x, y, and z directions (of a Cartesian coordinate system), respectively, it would require more than 400 CPU days to calculate a full 3D sensitivity function with Lonestar5's 1,252 cores by sequentially perturbing each volumetric element in the grid. By comparison, the computation of 2D axial-radial sensitivity functions of the flexural mode for a single frequency and a grid size of 250×99 in the radial and axial directions (of a cylindrical coordinate system), respectively, using an hp-adaptive 2D finite-element method (Matuszyk et al., 2013), requires approximately 17 CPU days on a desktop PC.

Alternatively, Huang et al. (2015) showed that the axial-radial sensitivity functions could be approximated using the product of 1D axial and radial sensitivities; they used the approximated axial-radial sensitivities to forward model sonic logs across thinly-bedded and invaded formations. I follow the same strategy to extend the definition

of spatial sensitivity functions in three dimensions by approximating $G_{3Dk}^{\{l\}}(r,z,\varphi,\mathbf{p_0},f)$ with the product of radial $R_k^{\{l\}}$, axial $F(z)$, and azimuthal $G_\varphi^{\{l\}}$ sensitivities; $R_k^{\{l\}}$ and $F(z)$ are defined in Chapter 2. The *normalized* azimuthal sensitivity depends on the acoustic source mode; for the case of a dipole source it is given by

$$G_\varphi^{\{l\}}(\varphi)=\begin{cases}\frac{1}{4}\,|\cos(\varphi)\,|\,, & \text{for dipole X}\\ \frac{1}{4}\,|\sin(\varphi)\,|, & \text{for dipole Y}\end{cases} \tag{5.2}$$

where $\varphi\in[0,2\pi]$ is the cylindrical azimuthal angle. The normalized (per unit volume) 3D sensitivity function becomes

$$G_{3Dk}^{\{l\}}(r,z,\varphi,\mathbf{p_0},f)=\frac{R_k^{\{l\}}(\mathbf{p_0},r,f)}{r\Delta r}\frac{F(z)}{\Delta z}G_\varphi^{\{l\}}(\varphi), \tag{5.3}$$

where Δr is the thickness of the cylindrical shell of radius r used to calculate $R_k^{\{l\}}$ and is equal to 10^{-3} m, while Δz is the thickness in the axial direction used to calculate F and is equal to 0.0185 m. Therefore, the 3D spatial sensitivity function associated with the flexural acoustic mode is constructed using a cylindrical system of coordinates for frequencies between 2 kHz and 7 kHz.

The average slowness $\bar{s}^{\{l\}}(d,f)$ measured at depth d by the sonic tool of a borehole mode $\{l\}$ at frequency f is given by

$$\bar{s}^{\{l\}}(d,f)=s^{\{l\}}(\mathbf{p_0},d,f)+\sum_k\sum_{r,z,\varphi}[p_k(r,z,\varphi)-p_{0k}(d)]G_{3Dk}^{\{l\}}(r,z,\varphi,\mathbf{p_0},f)\,\Delta V, \tag{5.4}$$

where $\{l\}$ denotes the flexural mode, $s^{\{l\}}(\mathbf{p_0},d,f)$ is the slowness at frequency f of the reference homogenous background with elastic properties $\mathbf{p_0}=[ss,sp,\rho]$, where ss is

shear slowness, sp is compressional slowness, and ρ is density; p_k is the k-th elastic property of the formation at position (r, z, φ) and p_{0k} must be chosen close to the average value of elastic property p_k in the vicinity of depth d; $\Delta V = r\Delta r\Delta z\Delta\varphi$ where Δz and Δr are thicknesses in the axial and radial directions, and $\Delta\varphi$ is the differential azimuthal angle used to construct $G_{3Dk}^{\{l\}}$ and is equal to 1 degree.

The spatial sensitivity function implemented with the synthetic examples considered in this chapter was constructed with 98 grid points in the radial direction, 99 in the axial direction, and 180 in the azimuthal direction, for a total 1.75×10^6 grid points; the same grid is implemented for all frequencies. The radial sensitivity function is more densely sampled in the vicinity of the borehole where the sensitivity value is greatest (see Figure 2.12 and Figure 2.13 in Chapter 2). To validate the choice of discretization, I verified that using a finer grid did not modify the forward modeled flexural logs for a wide range of background formation properties.

The shear slowness of the reference background is determined from the low-frequency flexural slowness. Compressional slowness and density are assumed known and can be obtained from compressional and density logs. It is remarked, however, that the sensitivity (integral of the spatial sensitivity over the 3D space) of the flexural mode to compressional slowness and density is at least one order of magnitude smaller than the sensitivity to shear slowness; thus, their contribution to the calculation of $\bar{s}^{\{l\}}(d, f)$ is negligible. Forward-modeled flexural logs are obtained in only a few CPU seconds when libraries of pre-computed 3D spatial sensitivity functions are available for different background formations and for specific selections of acoustic tool and borehole properties.

Equation 5.4 is valid for isotropic formations, where group and phase velocities are equal. In VTI formations, however, Hornby et al. (2003) emphasized that the low-frequency components of wave modes excited by dipole tools measure group velocities. Therefore, before applying equation 5.4, VTI layers are modeled as isotropic layers described by an apparent shear slowness (s_s^a) obtained from the wave's group velocity. Group velocities are derived from phase velocities following the procedure described by Miller et al. (2012). The theoretical formulae of v_{qSV} and v_{SH} polarized S-wave phase velocities, and quasi-compressional wave velocity v_{qP} in a TI medium are expressed in terms of stiffness coefficients c_{ij} (Daley and Hron, 1977; Chi and Tang, 2003), and are given by

$$v_{qP} = \left[\frac{c_{11}\sin^2(\vartheta_P) + c_{33}\cos^2(\vartheta_P) + c_{44} + \sqrt{M}}{2\rho}\right]^{\frac{1}{2}}, \tag{5.5}$$

$$v_{qSV} = \left[\frac{c_{11}\sin^2(\vartheta_P) + c_{33}\cos^2(\vartheta_P) + c_{44} - \sqrt{M}}{2\rho}\right]^{\frac{1}{2}}, \tag{5.6}$$

$$v_{SH} = \left[\frac{c_{66}\sin^2(\vartheta_P) + c_{44}\cos^2(\vartheta_P)}{\rho}\right]^{\frac{1}{2}}, \tag{5.7}$$

and

$$M = [(c_{11} - c_{44})\sin^2(\vartheta_P) - (c_{33} - c_{44})\cos^2(\vartheta_P)]^2 + (c_{13} + c_{44})^2\sin^2(2\vartheta_P), \tag{5.8}$$

where ϑ_P is the phase angle between the wavefront normal and the symmetry axis of the VTI medium, ρ is density, and c_{ij} are the stiffness coefficients. The group velocity is given in terms of phase velocity (Miller et al., 2012) as

$$v_G{}^2(\vartheta_P) = v_P{}^2(\vartheta_P) + \left[\frac{\partial v_P}{\partial \vartheta_P}\right]^2, \tag{5.9}$$

where the group angle ϑ_G is the angle between the group velocity vector and the symmetry axis of the VTI medium and is given by

$$\tan(\vartheta_P - \vartheta_G) = \frac{\left[\frac{\partial v_P}{\partial \vartheta_P}\right]}{v_P(\vartheta_P)}. \tag{5.10}$$

Therefore, the group velocity as function of group angle v_g becomes

$$v_g(\vartheta_G) = v_G(\vartheta_P), \tag{5.11}$$

where ϑ_G is obtained from equation 5.10 and $v_G(\vartheta_P)$ is obtained from equation 5.9. Thus, the apparent shear slowness is expressed as

$$s_s^a = 1/v_{g_{qSV}}, \text{ for an X-oriented dipole source} \tag{5.12}$$

$$s_s^a = 1/v_{g_{SH}}, \text{ for a Y-oriented dipole source} \tag{5.13}$$

where $v_{g_{qSV}}$ is the vertically polarized shear velocity, and $v_{g_{SH}}$ is the horizontally polarized shear velocity.

I validate the proposed forward model by comparing *modeled* slownesses obtained from equation 5.4 to *actual* slownesses obtained from 3D-TDFD numerical simulations. For self-consistency, I calculate $s^{\{l\}}(\mathbf{p_0}, d, f)$ using the 3D-TDFD code; therefore, any discrepancies observed between the actual and modeled slownesses are not

associated with processing bias or numerical errors (see 'Simulation method' in Mallan et al., 2011).

The grid step size in the x, y, and z direction, and the time step Δt chosen for the 3D-TDFD simulations satisfy (Stephen et al., 1985; Liu et al., 1996)

$$\Delta x, \Delta y, \Delta z \ \leq \frac{V_{min}}{10 f_{max}}, \tag{5.14}$$

$$\Delta t \ \leq \frac{[\Delta x^2 + \Delta y^2 + \Delta z^2]^{\frac{1}{2}}}{V_{max}}, \tag{5.15}$$

where V_{min} and V_{max} are the minimum and maximum wave velocities, respectively, and f_{max} is the dominant frequency in the source spectrum. In the examples examined in this chapter, f_{max}= 3 kHz, 0.6 cm $\leq \ \Delta x, \Delta y, \Delta z \ \leq$ 0.8 cm, and 1.5 μs $\leq \Delta t \leq$ 2 μs.

5.3 MODELING APPLICATIONS IN HIGH-ANGLE WELLS

The forward modeling method is applied to simulate flexural slownesses of synthetic layered formations. Results are compared to flexural slownesses obtained by processing time-domain waveforms of 3D-TDFD simulations using a matrix-pencil algorithm. In Example 1, I apply the method to an isotropic formation with a thin layer logged at 70 degrees to show that the input to the forward model in isotropic layers is the vertical shear slownesses of layers (equal to the horizontal shear slownesses). In Example 2, I apply the method to an isotropic formation with seven layers, which are thinner than the length of the receiver array, and logged at 75 degrees to show that the forward modeling method can reproduce spatial averaging effects on flexural logs. Next, in Example 3, I apply the method to a VTI formation with two semi-infinite layers logged at both 40 and 80 degrees to show that low-frequency components of flexural slownesses

measure group slownesses, hence group slownesses (that depend on dip) are the inputs to the forward model. Finally, in Example 4, I apply the method to an isotropic formation with large contrast between the shear slownesses of adjacent layers (> 20%) to show that spatial averaging effects induce differences between slownesses measured with orthogonal dipoles (apparent anisotropy).

I showed in equation 5.4 that a reference homogeneous background is required to forward model flexural logs using spatial sensitivity functions. To determine the reference background, I first partition the actual flexural log so that in a given interval the relative variation of slowness between any two points of the log is between ±10%. Two methods can then be used to determine the reference background invoked within each depth interval. If a library of pre-computed spatial sensitivity functions for different reference backgrounds is available, I choose the background (and its corresponding sensitivity function) that has a shear slowness closest to the average value of the low-frequency flexural slownesses (~ 2 kHz) within a given depth interval. Otherwise, I calculate the average of the low-frequency flexural slowness within a given depth interval and use this value, along with the compressional slowness and density, to define the background medium (and compute the corresponding spatial sensitivity function).

Each example is identified with the following name: *Type*+*NL*+L+*dip*, where *Type* = ISO, if the formation is isotropic, or *Type* = VTI, if the formation is VTI; *NL* = number of layers; L denotes layers; and *dip* = angle between the normal of layers and the borehole axis. For instance, an isotropic formation with 3 layers (horizontal layers) logged at 70 degrees is referred as ISO3L70.

In all examples, the sampling interval of logs is 0.6096 m (to minimize computational time and memory in 3D-TDFD simulations). A wireline tool with homogeneous elastic properties is assumed for modeling the spatial complexity and variability of material properties of actual acoustic tools (Su et al., 2011); it consists of a heavy fluid column as suggested by Sinha et al. (2006a) and Wang et al. (2017) with density 3110 kg/m^3 and compressional velocity 1800 m/s. The logging tool is placed at the center of the borehole of radius 0.11 m, fluid density 1000 kg/m^3, and compressional velocity 1500 m/s. Table 5.1 describes the geometrical and material properties of the wireline tool assumed in the numerical simulations described below.

5.3.1 Synthetic Example 1 – Isotropic Formation (ISO3L70)

First, I consider the case of an isotropic formation that includes a thin layer of 3 ft and logged at an angle of 70 degrees to show that in isotropic formations the elastic properties that are an input to the forward model are obtained from the actual layer shear slownesses (without angle correction). Table 5.2 shows the assumed layer properties while Figure 5.2 compares the actual flexural logs (continuous lines) obtained from 3D-TDFD to the modeled logs (circles) at discrete frequencies from 2 kHz to 7 kHz. Because the mid-layer is thinner than the length of the receiver array (6 ft) and dip is 70 degrees, flexural slownesses are averaged over a measured depth of approximately 6 m. Black dashed lines identify the flexural slowness of the reference backgrounds used to forward model the logs. The log is partitioned into three depth intervals; within each interval, the difference between the background flexural slowness (black dashed lines) and the actual slowness (continuous lines) is below 5%. Starting from a reference-background log containing two different slowness values (at each frequency), I reproduce the flexural

slownesses (circles) with a relative error of standard deviation below 1% for 30 logging points and for all frequencies. Figure 5.3 shows that low frequency (1.25 kHz) flexural slownesses measured with orthogonal dipoles are different from the exact shear slownesses (black dashed lines) in the vicinity of bed boundaries because of spatial averaging effects. Furthermore, spatial averaging effects induce differences in orthogonal dipole logs, giving rise to apparent (geometric) anisotropy. To locate bed boundaries (black dashed lines in Figure 5.3), I assume that the receiver array is within a given layer when the center of the receiver array at the borehole axis is within that layer.

5.3.2 Synthetic Example 2 – Multi-Layer Formation (ISO7L75)

The objective of this example is to show that 3D spatial sensitivity functions can reproduce the averaging effects observed in an isotropic formation when layer thicknesses are smaller than the length of the receiver array. For that purpose, I consider a seven-layer isotropic formation logged at 75 degrees with layer thicknesses smaller than the length of the receiver array (1.8 m) varying from 0.47 m to 0.82 m.

Table 5.3 summarizes the assumed formation properties while Figure 5.4 shows the actual flexural logs (continuous lines) and the modeled logs (circles) that agree with a relative error of standard deviation below 1% for 50 logging depth points and for all frequencies. Black dashed lines identify the flexural slownesses of the five reference background used to forward model the flexural logs. At every depth point, the difference between the background flexural slowness (black dashed lines) and the actual slowness (continuous lines) is below 5%. In this example, the same five backgrounds are used to model flexural slownesses obtained with dipole X and dipole Y sources. Figure 5.5 compares the low-frequency (1.25 kHz) flexural logs measured with orthogonal dipoles

to the exact layer shear slownesses (black dashed lines). The difference between the flexural logs and exact shear slownesses is more significant in the vicinity of layer boundaries because of spatial averaging effects and equals 5 μs/ft at measured depth -4.5 m.

Total CPU simulation time on a desktop PC required to calculate the modeled logs is under 3 minutes, compared to 15 hours using the 3D-TDFD in Lonestar5. Therefore, forward modeling of logs using spatial sensitivity functions is efficient to quantify spatial averaging effects on flexural logs across thinly-bedded formations.

5.3.3 Synthetic Example 3 – VTI Formation (VTI2L40 and VTI2L80)

In this example, I apply the fast-modeling method to a VTI formation to show that the input to the forward model for VTI layers is the apparent shear slowness s_s^a (which depends on dip).

I consider a formation with two VTI layers logged at 40 and 80 degrees. Table 5.4 shows the assumed formation properties where the vertical shear slownesses of layers 1 and 2 are 110 μs/ft and 132 μs/ft, respectively. The formation is logged at 40 degrees from Layer 1 to Layer 2 and 80 degrees from Layer 2 to Layer 1. Figure 5.6 and Figure 5.7 compare the actual logs (continuous lines), the modeled logs (circles), and the flexural slownesses of the reference backgrounds (black dashed lines) at 2 kHz, measured at 40 degrees and 80 degrees, respectively. At each log point, the difference between the background flexural slowness (black dashed lines) and the actual slowness (continuous lines) is below 10%. A total of 5 different backgrounds (black dashed lines in Figure 5.6 and Figure 5.7) are used to model the cross-dipole flexural logs at 2 kHz. The relative

error between the modeled logs and actual logs has a standard deviation below 3% for 30 logging points.

Figure 5.8 and Figure 5.9 compare flexural logs to apparent layer shear slownesses (s_s^a) (dashed lines) and to vertical and horizontal layer shear slownesses (triangles) for the formations penetrated by a well at 40 and 80 degrees, respectively; flexural logs at 2 kHz are equal to apparent shear slownesses (given by equations 5.12 and 5.13). In the vicinity of the layer boundary (measured depth 4 m), the difference between apparent shear slowness (s_s^a) and the flexural slowness at 2 kHz is approximately 10 μs/ft. In this example, differences in slownesses obtained from orthogonal dipoles are due to effective rather geometrical (apparent) anisotropy because layers are semi-infinite.

5.3.4 Synthetic Example 4 – Apparent Anisotropy (ISO4L75)

In Synthetic Examples 1 and 2 (ISO3L70 and ISO7L75), I showed that isotropic formations with thin layers exhibit apparent anisotropy. To better illustrate the concept of apparent anisotropy, I consider an isotropic formation with two thin layers of 1.5 ft and 2 ft logged at 75 degrees where the slowness contrast between adjacent layers is larger than 20%. Table 5.5 describes the assumed formation properties while Figure 5.10 compares the actual logs (continuous lines), the modeled logs (circles), and the flexural slownesses of the reference backgrounds (black dashed lines). In this example, the flexural slowness is calculated at frequencies above 4 kHz to show the effects of spatial averaging on logs without biasing caused by mode interference. Modeled logs agree with actual logs with a relative difference below 2% for 20 logging points. Figure 5.11 shows that orthogonal dipole logs at 4 kHz are different even though the formation is isotropic, which can be

falsely interpreted as effective anisotropy. Furthermore, slownesses obtained with a dipole-X source exhibit higher degree of averaging (over the measured depth) compared to dipole-Y slownesses because of the azimuthal asymmetry around the borehole (see Figure 5.1, the plane of symmetry lies along the X direction). Wang et al. (2017) showed that one method to reduce spatial averaging effects is to implement selective azimuthal processing of receivers. I illustrate the latter interpretation strategy by comparing the flexural slowness at 4 kHz measured with dipole X receivers to slownesses calculated using equation 5.4 with receivers located along +X and –X directions. Figure 5.12 shows that 'azimuthally' processed slownesses exhibit reduced spatial averaging effects. The flexural slowness logs at 4 kHz are different from the shear slownesses of layers (black dashed lines in Figure 5.11 and Figure 5.12) because, for this formation, the cutoff frequency is approximately 2 kHz. Another method to reduce apparent dipole anisotropy and enhance the spatial resolution of logs consists of using selective processing of receivers (along the tool mandrel) similarly to previous work reported by Hsu and Chang (1987) in vertical wells. In practice, however, obtaining accurate slownesses via selective and azimuthal processing of receivers requires an extended receiver array to enhance processing resolution and increase the signal-to-noise ratio.

5.4 EFFECT OF NUMBER OF BACKGROUNDS

I quantify the effect of number of backgrounds on the modeled logs by calculating the flexural logs of the formation described in Synthetic Example 2 (ISO7L75) using different backgrounds. The log is partitioned into intervals of equal measured depth, with the number of intervals varying from 1 to 50. Along each depth interval, I invoke a reference background that has a shear slowness equal to the mean value of the low-

frequency flexural slowness. Figure 5.13 compares the root-mean-square (RMS) difference of actual flexural logs with respect to model logs obtained with 1 to 50 different backgrounds. It is found that that the error decreases when the number of backgrounds increases. The effect of the number of backgrounds on modeled slowness is more pronounced at low frequencies because low-frequency slowness asymptotes to formation shear slowness (which can vary significantly across adjacent layers) while higher frequency slowness asymptotes to the borehole fluid slowness.

5.5 LIMITATIONS OF THE METHOD

Wang et al. (2017) studied wave propagation of the flexural mode and the P- and S-wave modes in formations penetrated by high-angle wells. They show that bed boundaries do not influence the propagation of flexural waves, but they strongly influence the propagation of P and S waves. Hence, the 3D spatial sensitivity function method cannot be used to estimate compressional and shear logs acquired in high-angle wells with a monopole source because P- and S-waves are not borehole guided waves in HA/HZ wells. The 3D linear spatial sensitivity function method could be extended to the case of borehole-guided Stoneley and quadrupole modes in isotropic formations. To model low-frequency Stoneley modes in TI formations using spatial sensitivity functions, the input to the fast simulation method would be a dip-dependent apparent/equivalent shear-wave velocity (Chi and Tang, 2003).

Furthermore, the forward-modeling method does not consider anisotropy in the calculation of spatial sensitivity function; anisotropic layers must be converted to equivalent-isotropic layers with group velocities that depend on dip. Zharnikov et al. (2013) showed that, in some formations (e.g., slow-anisotropic formations), the

equivalent-isotropic model is not reliable to accurately simulate flexural dispersion curves; higher-order approximations need to be considered for that purpose.

Larger differences are observed between flexural logs obtained with spatial sensitivity functions and those obtained from 3D-TDFD methods at low frequencies (below 4 kHz) because flexural modes can exhibit mode interference in the vicinity of dipping beds. Improved estimates of low-frequency flexural slowness can be achieved by using a 'dispersion-correction' inversion-based algorithm (Wang et al., 2010) where low-frequency flexural slownesses are obtained from the high-frequency components of flexural modes. This method, however, may suffer from non-uniqueness because high-frequency flexural modes are sensitive to borehole fluid properties.

5.6 SUMMARY AND CONCLUSIONS

Interpretation of flexural logs acquired in HA/HZ wells is challenging because geometrical and environmental features such as thin beds, spatial averaging, azimuthal asymmetry, and anisotropy affect the measured logs. To improve flexural log interpretation acquired in HA/HZ wells, 3D linear sensitivity functions were introduced. Three-dimensional sensitivity functions are constructed with the product of 1D axial, radial, and azimuthal sensitivities to efficiently calculate flexural-mode slownesses. Using synthetic examples, I showed that spatial sensitivity functions reduce simulation time of flexural logs from an average of 15 CPU hours (using 3D-TDFD methods) to 3 CPU minutes. Furthermore, flexural logs calculated with spatial sensitivity functions exhibit maximum relative differences of 3% when compared to those calculated with a 3D-TDFD method. Near the boundary of dipping beds, differences between the modeled

flexural logs and flexural logs calculated with 3D-TDFD methods can be due to interference between different wave modes.

In HA/HZ wells, azimuthal asymmetry around the borehole causes spatial averaging effects on flexural logs; we found that the difference between measured flexural slownesses and shear slownesses of layers is between 5 μs/ft to 10 μs/ft in the vicinity of layer boundaries. Furthermore, differences between the low-frequency components of flexural slownesses acquired with orthogonal dipoles indicate the presence of effective (when layers are VTI) or apparent (geometric) anisotropy (caused by spatial averaging effects).

In VTI formations penetrated by HA/HZ wells, both group shear slowness and quasi-compressional slowness depend on dip. Therefore, measuring both slownesses can be used, together with the density log, to estimate stiffness coefficients of VTI layers. Group shear slowness is obtained from the low-frequency dipole flexural mode, while quasi-compressional slowness is obtained from the compressional log.

5.7 TABLES AND FIGURES

Table 5.1: Geometric and elastic properties assumed for the wireline tool.

v_p (m/s)	1800
ρ (kg/m^3)	3110
Number of receivers	13
Inter-receiver spacing (m)	0.1524
First receiver offset	3.2766
Inner/outer radius (m)	NA/0.046

Table 5.2: Summary of the assumed elastic properties for Synthetic Example 1 (ISO3L70).

	ρ (kg/m^3)	**v_p (m/s)**	**v_s (m/s)**	**Thickness (m)**
Layer 1	2500	2880	1800	N/A
Layer 2	2520	3135	1900	0.9144
Layer 3	2500	2880	1800	N/A

Table 5.3: Summary of the assumed elastic properties for Synthetic Example 2 (ISO7L75).

	ρ (kg/m^3)	**v_p (m/s)**	**v_s (m/s)**	**Thickness (m)**
Layer 1	2500	2800	1750	N/A
Layer 2	2500	2809	1619	0.63
Layer 3	2500	2666	1561	0.82
Layer 4	2500	2754	1661	0.47
Layer 5	2500	2824	1751	0.65
Layer 6	2500	2743	1682	0.82
Layer 7	2500	2800	1750	N/A

Table 5.4: Summary of the assumed elastic properties for Synthetic Example 3 (VTI2L40 and VTI2L80).

	ρ (kg/m^3)	c_{11} (GPa)	c_{13} (GPa)	c_{33} (GPa)	c_{44} (GPa)	c_{66} (GPa)
Layer 1	2450	66.8	19.7	53.9	18.7	22.4
Layer 2	2500	48.8	18.3	40	13.2	15.6

Table 5.5: Summary of the assumed elastic properties for Synthetic Example 4 (ISO4L75).

	ρ (kg/m^3)	v_p (m/s)	v_s (m/s)	Thickness (m)
Layer 1	2600	4800	2500	N/A
Layer 2	2520	3800	1920	0.6096
Layer 3	2650	4600	2700	0.4572
Layer 4	2600	4800	2500	N/A

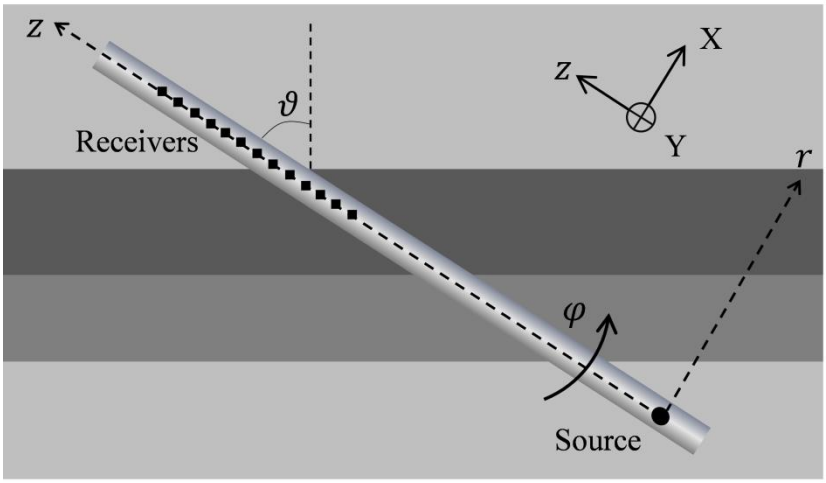

Figure 5.1: Formation with four layers and a sonic tool dipping at an angle ϑ. Dipole X points along the X axis while dipole Y points in and out of the page. The cylindrical system of coordinates is represented by (r, z, φ).

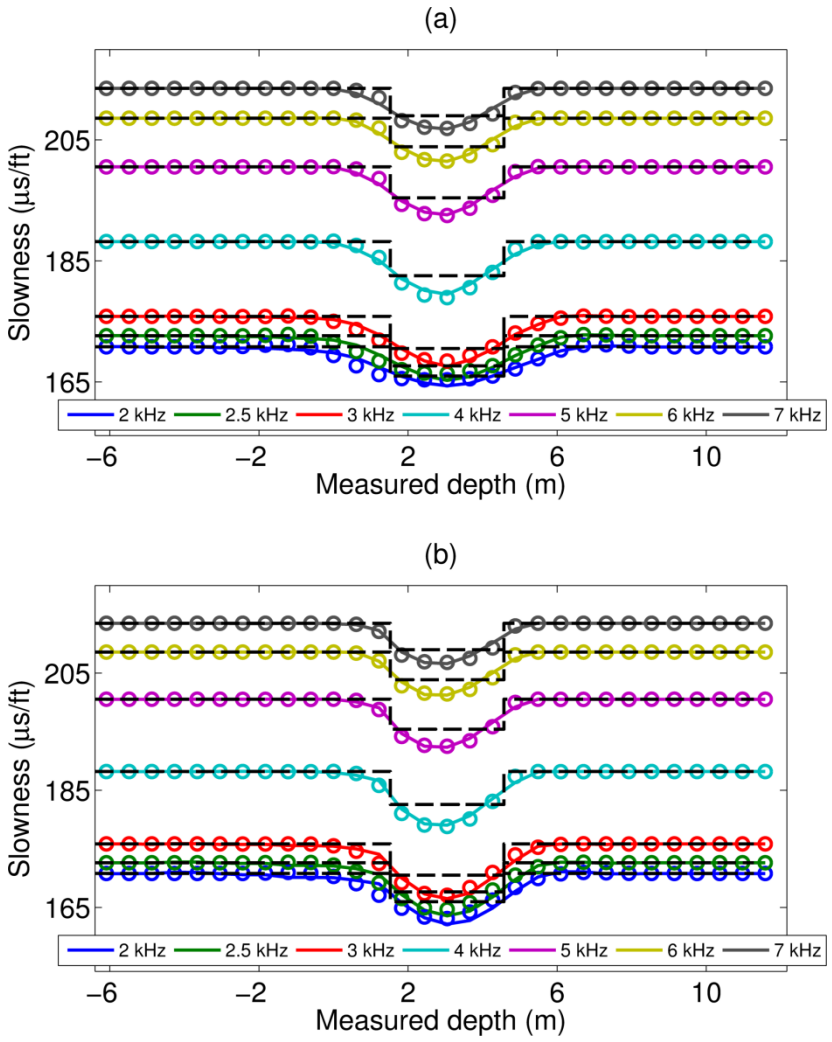

Figure 5.2: Comparison of actual logs (continuous lines) to modeled logs (circles) measured with (a) dipole-X, and (b) dipole-Y sources for the isotropic formation of Synthetic Example 1 (ISO3L70). Black dashed lines identify the slownesses of the two reference backgrounds.

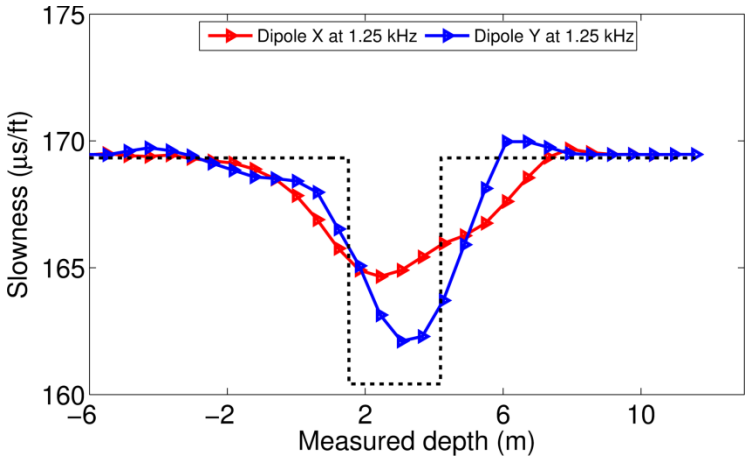

Figure 5.3: Comparison of flexural logs at 1.25 kHz measured with orthogonal dipoles (dipole X and dipole Y) to formation shear slownesses (black dashed lines) for the isotropic model of Example 1 (ISO3L70).

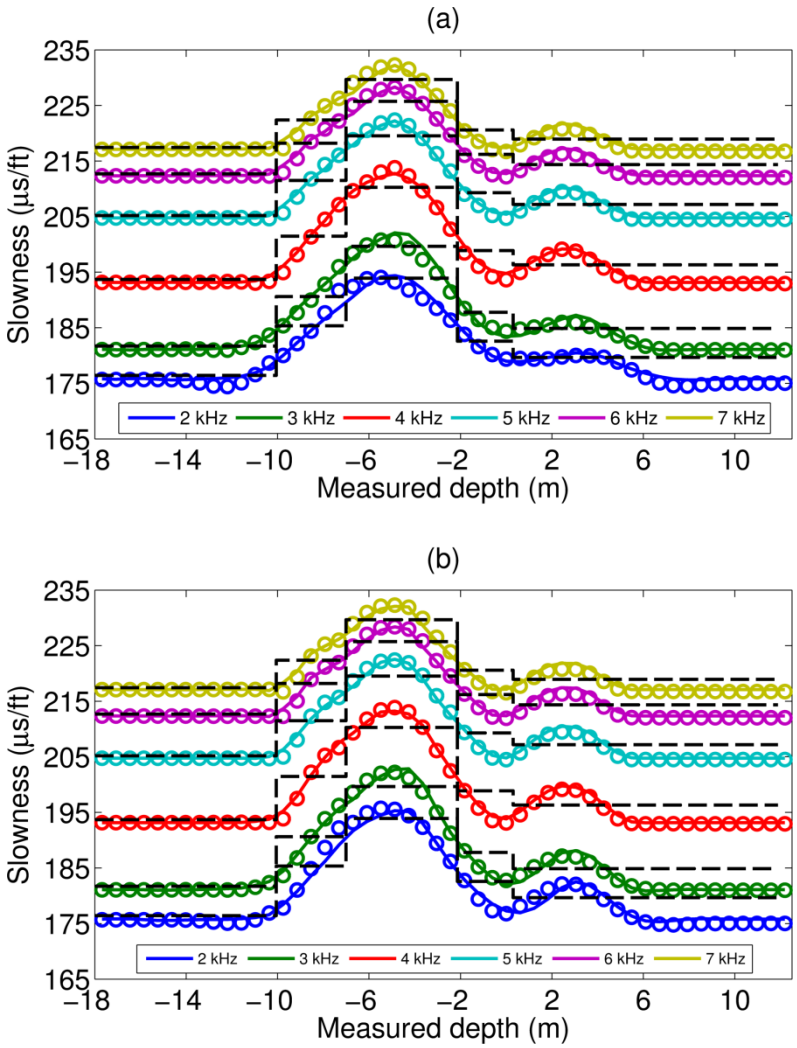

Figure 5.4: Comparison of actual logs (continuous lines) to modeled logs (circles) measured with (a) dipole-X, and (b) dipole-Y sources for the isotropic formation of Synthetic Example 2 (ISO7L75). Black dashed lines identify the slownesses of the five reference backgrounds.

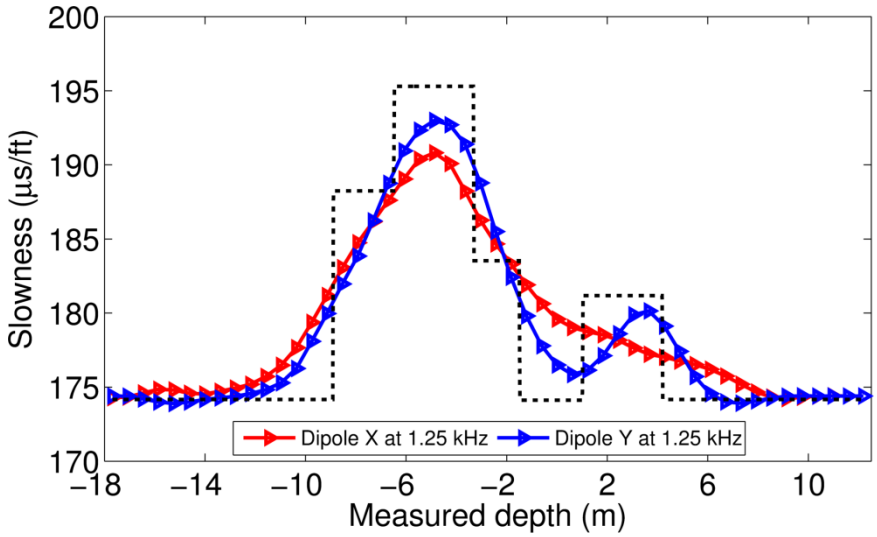

Figure 5.5: Comparison of flexural logs at 1.25 kHz measured with orthogonal dipoles (dipole X and dipole Y) to formation shear slownesses (black dashed lines) for the isotropic model of Synthetic Example 2 (ISO7L75).

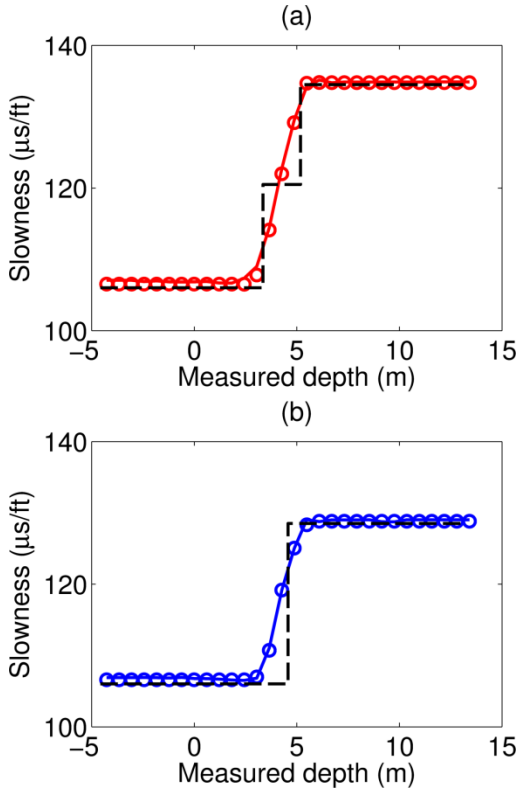

Figure 5.6: Comparison of actual logs (continuous lines) to modeled logs (circles) at 2 kHz measured with (a) dipole-X, and (b) dipole-Y sources for the VTI formation of Synthetic Example 3 (VTI2L40). Black dashed lines identify the slownesses of the reference backgrounds.

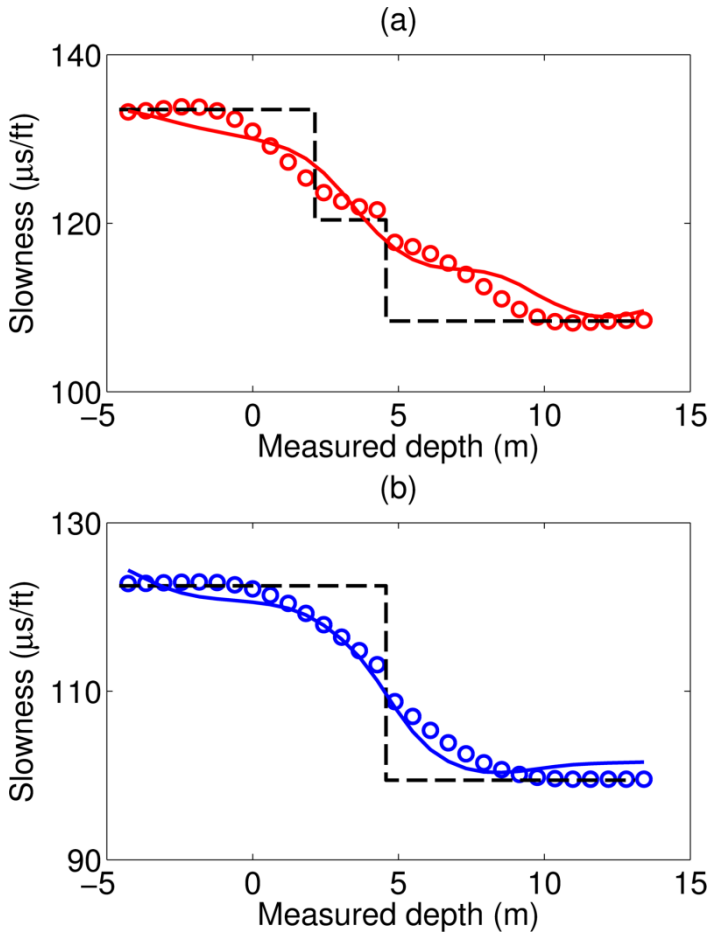

Figure 5.7: Comparison of actual logs (continuous lines) to modeled logs (circles) measured with (a) dipole-X, and (b) dipole-Y sources at 2 kHz for the VTI formation of Synthetic Example 3 (VTI2L80). Black dashed lines identify the slownesses of the reference backgrounds.

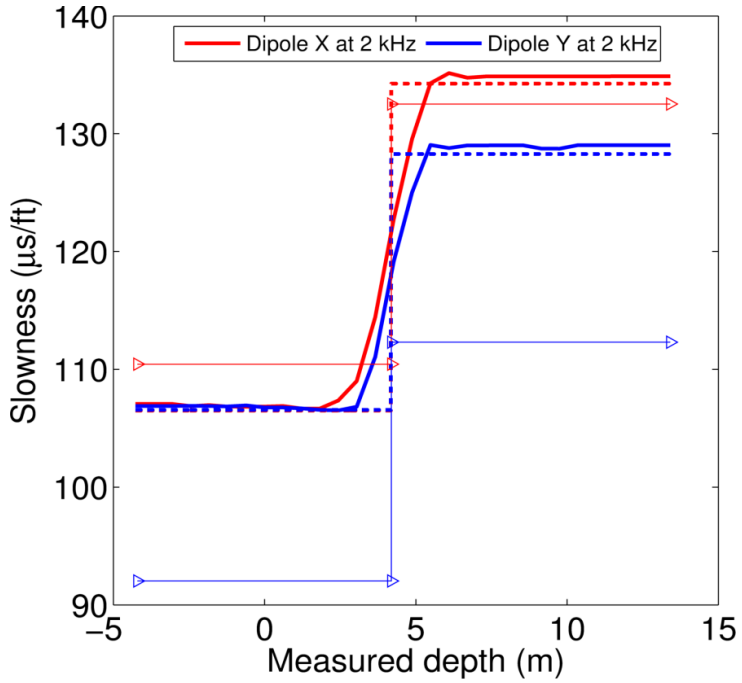

Figure 5.8: Comparison of actual logs at 2 kHz (continuous lines) to apparent shear slownesses (dashed line) for the VTI formation of Synthetic Example 3 (VTI2L40). Vertical and horizontal shear slownesses of layers are identified with red and blue triangles, respectively.

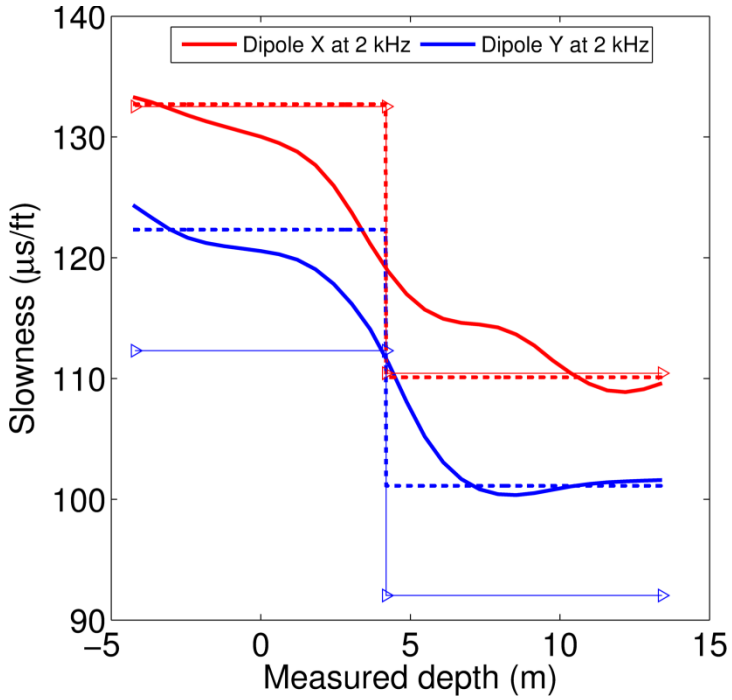

Figure 5.9: Comparison of actual logs (continuous lines) to apparent shear slownesses (dashed line) for the VTI formation of Synthetic Example 3 (VTI2L80). Vertical and horizontal shear slownesses of layers are identified with red and blue triangles, respectively.

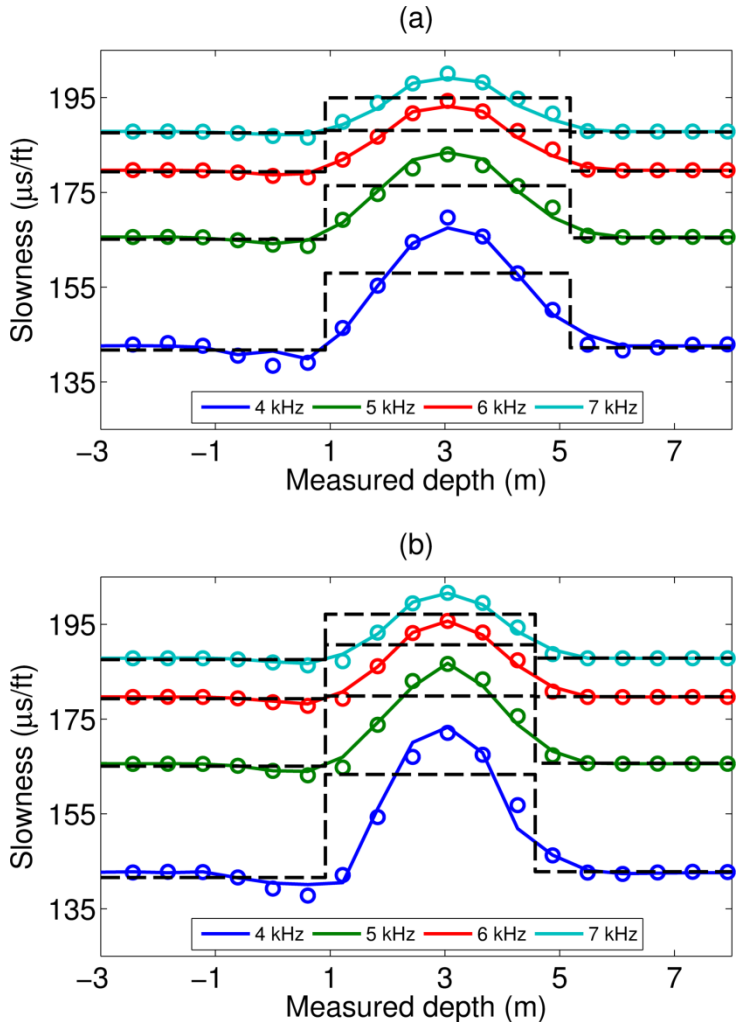

Figure 5.10: Comparison of actual logs (continuous lines) to modeled logs (circles) measured with (a) dipole-X, and (b) dipole-Y sources for the isotropic formation of Synthetic Example 4 (ISO4L75). Black dashed lines identify the slownesses of the reference backgrounds.

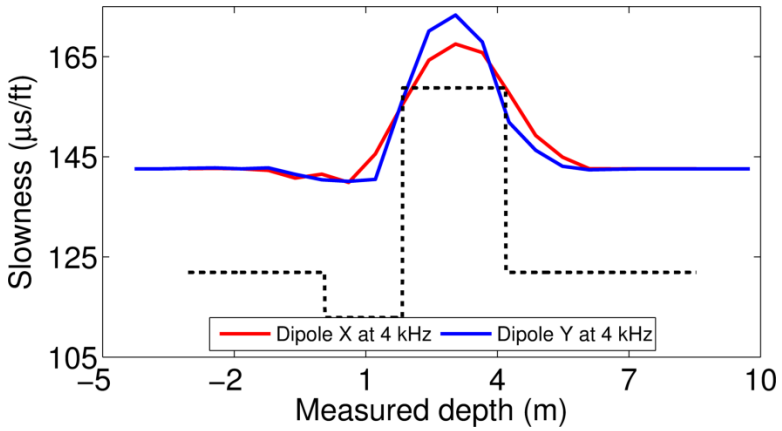

Figure 5.11: Comparison of flexural logs at 4 kHz measured with dipole-X and dipole-Y sources for the isotropic formation of Synthetic Example 4 (ISO4L75). Black dashed lines indicate the shear slownesses of layers.

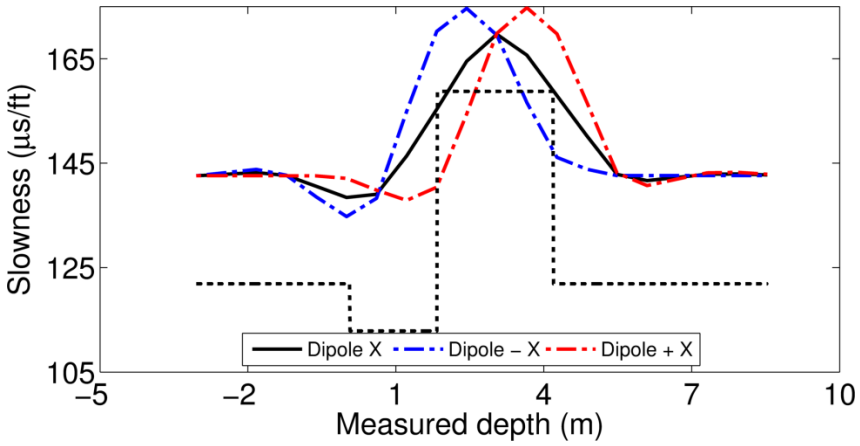

Figure 5.12: Flexural slownesses at 4 kHz calculated with the fast-forward modeling procedure assuming azimuthal receivers located along the +X and –X directions (ISO4L75). Black dashed lines identify the shear slownesses of layers.

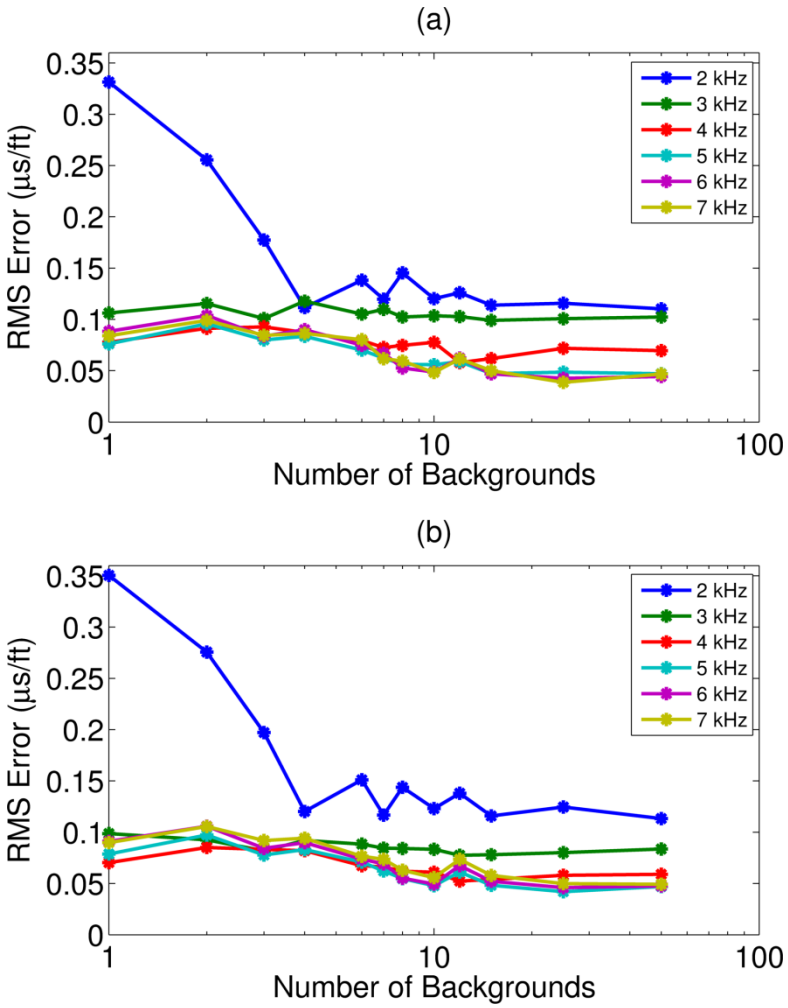

Figure 5.13: Root-mean-square (RMS) difference between actual logs and flexural logs modeled using 1 to 50 backgrounds measured with (a) dipole-X, and (b) dipole-Y sources for Synthetic Example 2 (ISO7L75).

Chapter 6: Summary, Conclusions, and Recommendations

This chapter summarizes the developments and contributions of this dissertation, draws general conclusions from the findings, and presents recommendations for future research.

6.1 SUMMARY

There are two main objectives of this dissertation:

1) to develop fast modeling of borehole acoustic modes in vertical wells and HA/HZ wells, and
2) to implement inversion-based algorithms in vertical wells to
    a. reduce noise and spatial averaging effects on acoustic logs taking into account physical and geometrical constraints, and
    b. estimate layer-by-layer stiffness coefficients of formations from sequential inversion of multi-frequency borehole acoustic logs.

The motivations behind these objectives are: (1) forward modeling of acoustic modes often requires time-consuming finite-difference and finite-element numerical simulations, (2) current noise mitigation methods filter slowness data without taking into account physical constraints, and (3) current methods to estimate stiffness coefficients are either expensive (core data analysis), non-unique (effective medium models), or limited by the vertical resolution of logs (because of spatial averaging effects).

Fast-forward modeling of acoustic logs is achieved using spatial sensitivity functions derived from first-order perturbation theory. Spatial sensitivity functions quantify (1) the variation of phase slowness measured by the sonic tool caused by a

spatially local perturbation of elastic properties, and (2) the geometrical averaging introduced by acoustic instruments on logs. Three-dimensional spatial sensitivity functions are efficiently calculated using the product of 1D axial, radial, and azimuthal sensitivities. The axial sensitivity function quantifies the spatial averaging introduced on sonic logs by the acoustic tool and depends on the geometrical properties of the tool. Axial sensitivities can be derived analytically using ray theory approximations. Radial sensitivity functions quantify the length of investigation of borehole modes and depend on the formation type (i.e., fast, intermediate, or slow), borehole fluid properties, and the tool geometrical and elastic properties. The azimuthal sensitivity function depends on the acoustic source mode.

In a formation with horizontal layers penetrated by a vertical well, the fast-forward modeled log is the convolution of the axial sensitivity function with model parameters obtained from layer-by-layer slownesses. While in a formation with azimuthal asymmetry (HA/HZ wells), the forward model is the superposition of a reference background slowness and the convolution of a 3D spatial sensitivity function with layer-by-layer models of elastic properties. Forward modeling using spatial sensitivity functions was validated with synthetic examples that included formations with thin layers, dipping layers, and anisotropy. In vertical wells, acoustic logs are calculated at least 100 times faster using 1D axial sensitivity functions compared to conventional finite-element or finite-difference methods. In HA/HZ wells, acoustic logs are calculated at least 300 times faster (for simple geometries) and on average 2000 times faster (for complex geometries) compared to 3D finite-difference methods.

In formations with horizontal layers penetrated by high-angle wells, the fast-forward modeling method of acoustic logs allows the implementation of two inversion-based methods: (1) a physics-based method to mitigate and reduce spatial averaging effects and noise on logs, and (2) a sequential inversion to estimate stiffness coefficients of layers.

Mitigating noise in borehole sonic logs

The inputs to the physics-based method are bed boundaries of layers and initial estimates of slownesses within each layer. For synthetic examples bed boundaries are known, while for field measurements they are determined from gamma ray (GR), bulk density (ρ), or sonic logs. Initial estimates of slownesses are calculated from the mean value of shear and compressional logs within each layer. I showed that the physics-based inversion method efficiently mitigates measurement noise and spatial averaging effect of acoustic logs using synthetic examples and two field examples in the North Sea and the deepwater Gulf of Mexico. Resulting logs from the inversion reflect more accurately layer-by-layer slowness values of rock formations and are calculated in less than 14 seconds for a 100 ft depth log.

When bed boundaries of formations are not known, the method can be applied with beds uniformly spaced at the log sampling interval, and yields noise mitigated logs that match the synthetic noise-free logs with a correlation larger than 0.97. When layers are thinner than the FWHM of the sensitivity function, the method can be applied to logs calculated with a subset of receivers. In the North Sea example, GR, bulk density, or compressional logs can be used to estimate the locations of bed boundaries. Although the bed boundaries derived from the aforementioned three well logs may be slightly

different, the effect on the noise-mitigated sonic logs is minimal; the difference between any two noise-mitigated sonic logs has a standard deviation below 3 μs/ft.

The physics-based method uses geometrical and physical constraints for noise reduction and yields sonic logs that more accurately reflect the physical properties of formations penetrated by vertical wells.

Estimating stiffness coefficients of VTI formations

In VTI formations, I developed a sequential inversion method that uses compressional, Stoneley, and flexural/quadrupole logs to estimate c_{11}, c_{13}, c_{33}, c_{44}, and c_{66} of layers. Logs are mitigated for spatial averaging prior to the sequential inversion by invoking axial sensitivity functions. The sequential inversion takes advantage of the different sensitivities of borehole modes to stiffness coefficients. First, c_{33} and c_{66} are estimated from the compressional log and the Stoneley log at low frequency, respectively. Then, c_{44} is estimated from the low-frequency flexural/quadrupole mode, and finally c_{11} and c_{13} are estimated from the flexural/quadrupole logs at higher frequencies; c_{11} and c_{13} are calculated last because borehole modes exhibit low sensitivity to both coefficients. Fourteen logs are used during inversion (1 compressional log, 1 Stoneley log, and 12 frequency-dependent flexural/quadrupole logs).

The sequential inversion method was applied to synthetic formations with thin layers and large contrast of elastic properties between adjacent layers logged with wireline and LWD instruments. I showed that: (1) the inversion-based interpretation method yields accurate estimations of c_{33}, c_{44}, and c_{66}, (2) larger uncertainties are obtained when estimating c_{11} and c_{13}, and (3) stiffness coefficients are obtained layer-by-layer and continuously along the depth interval of interest.

The fast-forward modeling method introduced in this dissertation is used to calculate flexural slownesses of formations penetrated by a high-angle well. Fast-forward modeling is achieved using three-dimensional spatial sensitivity functions. Synthetic formations with varying dip, elastic properties, and layer thicknesses were considered. In isotropic formations, the inputs to the fast-forward model are density, shear slowness, and compressional slowness. In VTI formations, however, the inputs are density and apparent shear and compressional slownesses that depend on dip. Apparent shear slowness is obtained from the low-frequency dipole flexural mode, while apparent compressional slowness is obtained from the compressional log. Modeled flexural logs calculated using spatial sensitivity functions agree with flexural logs simulated using a 3D-TDFD method with relative errors below 3%. It was found that in isotopic formations with layers thinner than the length of the receiver array cross-dipole slownesses are different because of apparent (geometric) anisotropy, while in VTI formations they are different because of effective anisotropy.

6.2 CONCLUSIONS

The research and methods documented in the dissertation led to the following general conclusions:

6.2.1 Spatial Sensitivity Functions and Forward Modeling

i. First-order perturbation theory and spatial sensitivity functions enable fast-forward modeling of sonic logs in isotropic and VTI formations penetrated by vertical or HA/HZ wells.

ii. Spatial sensitivity functions decouple (1) the effect of spatial averaging introduced by acoustic tools and (2) the intrinsic elastic properties of layers on measured logs.

iii. Calculating sonic logs using spatial sensitivity functions reduces simulation time from an average of 240 seconds to 2 seconds per depth for vertical wells and from 15 CPU-hours to 3 CPU-minutes per depth for HA/HZ wells, allowing inversion-based interpretation of formations with complex geometries.

6.2.2 Mitigating Noise in Borehole Sonic Logs

i. Axial sensitivity functions allow the implementation of a fast and physics-based inversion method to mitigate averaging effects and borehole environmental noise on sonic logs.

ii. The inversion-based method to mitigate noise on logs is stable and converges in less than 20 iterations and less than 14 seconds for a 100 ft depth log.

iii. To achieve stability during inversion, Tikhonov regularization can be used in formations with layers thinner than the FWHM of the axial sensitivity functions and in formations with a low signal-to-noise ratio.

iv. The noise mitigation method reduces noise on sonic logs even when bed boundaries are not known by placing boundaries separated by the sampling interval of logs.

v. The inversion-based noise mitigation method is robust: slight variations in bed boundary locations estimated from gamma ray, density, or compressional logs

have minimal effect on the noise-mitigated acoustic logs – the standard deviation of the difference between any two logs being under 3 μs/ft.

vi. When layers are thinner than the FWHM of the axial sensitivity function, sonic logs must be processed with a subset of receivers before applying the inversion-based method.

6.2.3 Estimating Stiffness Coefficients of VTI Formations

i. Stiffness coefficients of VTI layers can be estimated efficiently from compressional, Stoneley, and flexural/quadrupole logs by applying a two-step inversion algorithm: *Step 1)* de-averaging of acoustic logs using spatial sensitivity functions, and *Step 2)* applying sequential inversion of stiffness coefficients.

ii. Sequential inversion is more stable and efficient than simultaneous inversion when borehole modes exhibit low sensitivity to stiffness coefficients.

iii. The inversion algorithm allows the estimation of layer-by-layer shear slownesses from low-frequency quadrupole modes with relative errors below 3%.

iv. Layer anisotropy is detected by analyzing data residuals between the field/measured (actual) logs and the modeled logs obtained when layers are assumed isotropic. A bias distribution of data residuals indicates that using an isotropic model to estimate stiffness coefficients is incomplete and that anisotropic models should be used instead.

v. Three sources of errors on the estimated stiffness coefficients were observed: (1) bias error that results from de-averaging the logs prior to inversion, (2)

bias error propagated during the sequential inversion, and (3) error associated with noisy slowness logs. The error of the estimated coefficients is largest for c_{11} and c_{13} (up to 17% relative error) because borehole modes exhibit low sensitivity to these two coefficients.

6.2.4 Modeling Flexural Logs in High-Angle Wells

i. Spatial sensitivity functions are used to quantitatively interpret sonic logs obtained from orthogonal dipoles in high-angle wells and are efficiently calculated using the product of 1D axial, radial, and azimuthal sensitivities.
ii. Fast-forward modeling using spatial sensitivity functions is at least 300 times faster than conventional 3D-TDFD numerical simulations and provides accurate estimations of flexural slownesses with relative errors below 3%.
iii. In isotropic formations, azimuthal asymmetry causes differences in orthogonal dipole logs that can falsely be interpreted as effective anisotropy.
iv. In VTI formations penetrated by HA/HZ wells, flexural slownesses asymptote (at low frequencies) to group shear slowness that depends on dip.
v. The error between flexural slownesses calculated with 3D sensitivity functions and slownesses simulated using a 3D-TDFD method is largest at low frequencies because of mode interference.

6.3 RECOMMENDED BEST PRACTICES

In this section, I summarize recommendations for best practices to apply the forward and inverse modeling methods proposed in this dissertation:

6.3.1 Mitigating Noise in Borehole Sonic Logs

i. Define bed boundaries from sonic logs and other petrophysical logs, e.g., gamma ray and density.

ii. If bed boundaries are unknown, place beds continuously over the depth interval separated by the sampling interval of logs (typically 0.5 ft).

iii. Use second-order regularization to stabilize inversion results. One method to determine the regularization parameter is using a misfit (between measured and modeled logs) versus regularization plot. The point of maximum curvature yields the value of regularization at which the slowness logs have been mitigated of most of the high-amplitude noise.

iv. Apply the inversion method to minimize noise jointly on compressional and shear slownesses. Accordingly, estimated slownesses in isotropic layers verify $v_p/v_s > \sqrt{2}$.

v. Use a subset of receivers to process sonic logs when layer thicknesses are smaller than the FWHM of the axial sensitivity functions.

vi. Use a data weighting matrix to the data misfit term of the quadratic cost function when measurements are unreliable or do not satisfy rock physics constraints (e.g., $v_p/v_s < \sqrt{2}$).

vii. Evaluate the accuracy of the inversion results by examining the data residuals from inversion: a bimodal or a biased (non-zero mean) distribution could indicate model limitations, while outliers indicate noise.

6.3.2 Estimating Stiffness Coefficients of VTI Formations

i. Mitigate noise (e.g., cable tension, tool vibrations) and spatial averaging effects on sonic logs before estimating stiffness coefficients from multi-frequency borehole acoustic logs.

ii. Calculate spatial sensitivity functions using the exact elastic and geometrical properties of the tool and borehole fluid because flexural and Stoneley modes are sensitive to borehole properties.

iii. Error bars should accompany the estimated coefficients and can be obtained by adding zero-mean Gaussian noise to acoustic logs and applying error propagation methods.

iv. Use sequential inversion (not simultaneous) to calculate stiffness coefficients in the following order:

    1. estimate c_{33} from the compressional log,
    2. estimate c_{66} from the low-frequency Stoneley log,
    3. estimate c_{44} from the low-frequency flexural/quadrupole log, and
    4. estimate c_{11} and c_{13} from high-frequency flexural/quadrupole logs.

v. In LWD operations, use quadrupole slownesses to estimate elastic properties because flexural slownesses are biased by tool modes.

vi. Although discrete frequencies were used to perform the sequential inversion and estimate stiffness coefficients, a continuous range of frequencies can be used if slowness measurements are noisy.

vii. Analyze the histogram of data residual to determine whether isotropic or VTI models more accurately describe the formation.

6.3.3 Modeling Flexural Logs in High-Angle Wells

i. In HA/HZ wells, estimate the shear slowness of the reference background from the low-frequency flexural log.

ii. In general, to model flexural slownesses with relative errors below 3%, the relative difference between the low-frequency flexural slowness and the shear slowness of the background should be below 10%.

iii. To improve the efficiency of forward modeling, use a library of pre-computed 3D spatial sensitivity functions for different background formations and for specific selections of acoustic tool and borehole properties.

iv. Calculate 3D spatial sensitivity from the product of F (axial sensitivity), R (radial sensitivity), and G_{φ} (azimuthal sensitivity).

v. To apply fast-forward modeling in VTI formations, model VTI layers as equivalent-isotropic layers that are described by apparent shear and compressional slownesses (that depend on dip).

vi. In formations with high dip and large contrast of elastic properties between adjacent layers, flexural modes can exhibit mode distortions. Hence, high-frequency flexural modes can be used to estimate shear slownesses of layers by applying a 'dispersion-correction' method (Wang et al., 2017).

6.4 RECOMMENDATIONS FOR FUTURE WORK

The following is a list of recommendations that could advance the research topics documented in this dissertation:

- Tang and Cheng (2004) show that cross-dipole tools are capable of measuring flexural modes behind casing if casing and formation are well bonded.

Therefore, forward modeling of acoustic logs could be extended to formations with cased boreholes; the sensitivity function will account for the tool elastic and geometric properties, the borehole fluid properties, the borehole size, and the elastic and geometrical properties of the casing.

- The forward modeling described in this dissertation assumes that the tool is centered in the borehole. However, in high-angle wells or in the presence of borehole damage the tool is off-centered (Zheng et al., 2004; Byun and Toksöz, 2006; Pardo et al., 2013). Therefore, the forward modeling proposed in this dissertation could be extended for applications in formations logged with an off-centered tool.
- The proposed inversion-based methods implemented in this dissertation use Levenberg-Marquardt minimization techniques. Non-gradient based methods such as Bayesian inversion could be used instead.
- Acoustic tool instruments have complex geometries, e.g., grooves that attenuate the arrival of tool modes. Therefore, modeling the exact tool geometry would require complex three-dimensional numerical methods which are computationally expensive. To increase the efficiency and speed of calculating sensitivity functions for complex tools, equivalent tools may be developed following the techniques described by Su et al. (2011) and Lee et al. (2016). The equivalent tool model is defined with two parameters: a and M_T, where a is equivalent tool radius and M_T is the effective modulus of the tool.

- Borehole acoustic modes measured by acoustic tools depend on tool radius, first-receiver offset, number of receivers, and spacing between consecutive receivers. A thorough analysis of the influence of tool parameters on borehole modes could lead to the development of an acoustic tool with improved frequency and vertical resolutions. This could reduce aliasing or ripples (Foti et al., 2002) on measured slownesses.
- The 3D-TDFD method used in this dissertation was implemented using a Cartesian coordinate system; however, the borehole and tool are cylindrical. Therefore, implementing the 3D-TDFD method in cylindrical coordinate could reduce numerical errors, computational time, and memory resources.
- I recommend implementing a joint-interpretation method to estimate stiffness coefficients of VTI formations using borehole sonic modes, effective medium model, and core measurements (e.g., tri-axial strength tests and ultra-sonic measurements) which would yield dynamic and static estimations of stiffness coefficients.
- An important step in the proposed inversion-based interpretation method is the construction of a layered-geometrical model. To enhance the detection of bed boundaries, high-resolution borehole images, such as formation micro-images or acoustic image measurements could be used.
- In high-angle wells, errors in the relative dip between borehole and layers can generate errors in estimated elastic constant. Well survey data can be used to reduce the uncertainty in estimations of relative dip.

- In the presence of invasion, radial sensitivities are used to describe the variation of slownesses in the radial direction; therefore, radial sensitivities can be used for fluid substitution applications on sonic logs.
- Joint-inversion of shear and compressional logs with other petrophysical logs such as density, nuclear, and resistivity can be implemented for petrophysical interpretations of reservoirs.
- Investigating and comparing different wave processing methods would improve the efficiency and accuracy of measured slownesses from acoustic tools.
- Applying spatial sensitivity functions in fractured formations to improve fracture characterization.
- The perturbation theory developed in this dissertation uses first-order approximations. Although first-order approximations yield accurate results for a wide range of conditions, using higher-order (second-order) approximations could improve the accuracy of estimated slownesses and stiffness coefficients. The limitations of using second-order approximations would be the higher computing requirements.

Nomenclature

List of symbols

α: regularization parameter

A, B, C, D, E : complex amplitudes of transmitted and reflected waves

$\mathbf{B}$: model vector of slowness

$\{c\}$: compressional borehole mode

c: velocity

c_{11}, c_{13}, c_{33}, c_{44}, c_{66},: stiffness coefficients

$\mathbf{C}$: elastic stiffness tensor

$\mathbf{cov}$: covariance

δ: Thomsen parameter

$\Delta\mathbf{c}$: vector of uncertainty in the estimated stiffness coefficient

Δc_k: uncertainty in the estimated stiffness coefficient c_k

$\Delta\rho$: variation of density

$\Delta\mathbf{s}$: vector of uncertainty in the estimated slowness s

$\Delta s_i(f_i)$: uncertainty in the estimated slowness s at frequency f_i

Δt: time step in 3D-TDFD simulations

Δv_p: variation of compressional velocity

Δv_s: variation of shear velocity

ΔV: elemental volume equal to $r\Delta r\Delta z\Delta\varphi$ in cylindrical coordinates

$\Delta x, \Delta y, \Delta z$: grid step size in 3D-TDFD simulations

Δz_R: vertical distance between two consecutive receivers

d: acoustic log depth (or center of receiver array)

$\mathbf{d_{log}}$: data vector (slowness log)

D_T: total distance

ε: Thomsen parameter

$\boldsymbol{\varepsilon}$: strain tensor

e: cost function

e_1: cost function of inversion *Step 1*

e_2: cost function of inversion *Step 2*

$E^{(p)}$: misfit of forward model and data of compressional slowness

$E^{(s)}$: misfit of forward model and data of shear slowness

ϕ: wave potential

φ: azimuthal angle

f: frequency

$\{fl\}$: flexural borehole mode

$\mathbf{f}(\mathbf{m})$: forward model

F: spatial averaging function

F: matrix respresentation of the axial sensitivity function

γ: Thomsen parameter

$\mathbf{g}(\mathbf{p})$: forward model of slownesses of a homogeneous formation with elastic property **p**

$G^{\{l\}}$: normalized axial sensitivity function of wave mode $\{l\}$

$G_{\varphi}^{\{l\}}$: normalized azimuthal sensitivity function of wave mode $\{l\}$

$G_{3Dk}^{\{l\}}$: normalized three-dimensional sensitivity function of wave mode $\{l\}$

J: Jacobian matrix

k_i: wavenumber of layer *i*

k_I, k_{II}, k_{III}: wave numbers of layers *I, II,* and *III*

Λ: regularization weighing matrix

$\{l\}$: borehole mode

L: length of receiver array

L_i: non-negative model parameter of layer i equal to $ss_i^2 - 2sp_i^2$

m: vector of model parameters

n_t: total number of layers

N: total number of receivers

p_{0k}: k-th component of the vector $\mathbf{p_0}$

p_k: k-th component of the vector $\mathbf{p}$

$\mathbf{p_0}$: vector of elastic properties for the reference formation

$\mathbf{p}$: vector of elastic properties for a homogeneous formation

P_i: non-negative model parameter of layer i equal to sp_i^2

$\{q\}$: quadrupole borehole mode

ρ: density

$R_k^{\{l\}}$: radial sensitivity function of wave mode $\{l\}$

$R(\theta)$: PP reflectivity at angle θ

σ: 1D-stress

$\boldsymbol{\sigma}$: stress tensor

σ_{c_k}: standard deviation of the error of the estimated stiffness coefficient c_k

$\sigma_{s(f_i)}$: standard deviation of the error of the estimated slowness at frequency f_i

$\{st\}$: Stoneley borehole mode

$s(z)$: slowness at depth z

s_r: slowness of the reference homogeneous formation

s_p: slowness of the perturbed homogeneous formation

$\mathbf{s_{sp}}$: compressional slowness logs

$\mathbf{s_{ss}}$: shear slowness logs

$s^{\{l\}}$: slowness of mode $\{l\}$

$\bar{s}^{\{l\}}(d, f)$: averaged slowness of mode $\{l\}$ at depth d and frequency f

ss: shear slowness

sp: compressional slowness

s_s^a: apparent shear slowness

$\mathbf{S}$: matrix representation of $S_k^{\{l\}}(f_i)$

$S_k^{\{l\}}$: sensitivity of mode $\{l\}$ to stiffness coefficient c_k

$^{\mathbf{t}}$: transpose

t_{ij}: travel time between receivers i and j

ϑ_G: group angle

ϑ_P: phase angle

T: total travel time

u: one-dimensional displacement field

$\mathbf{u}$: composite compressional and shear log data vector $\mathbf{u} = [\mathbf{u_p}, \mathbf{u_s}]$

$\mathbf{u_p}$: compressional log data vector

$\mathbf{u_s}$: shear log data vector

$v_{g_{qSV}}$: quasi-shear vertically-polarized group phase velocity

$v_{g_{SH}}$: horizontally-polarized shear group phase velocity

v_{SH}: horizontally-polarized shear wave phase velocity

v_G: group velocity

v_P: phase velocity

v_p: compressional velocity

v_s: shear velocity

v_{p45}: compressional velocity at 45 degrees

v_{ph}: horizontal compressional velocity

v_{pv}: vertical compressional velocity

v_{qP}: quasi-compressional wave phase velocity

v_{qSV}: quasi-shear vertically-polarized wave phase velocity

v_{SH}: horizontally-polarized shear wave phase velocity

v_{sh}: horizontal shear velocity

v_{sv}: vertical shear velocity

$\mathbf{W_d}$: data weight matrix

$\mathbf{\Sigma}$: diagonal matrix whose component are $\Sigma_{ii} = 1/\sigma_{s(f_i)}$

X_i: spectrum at receiver i

Y: layer of slowness s_p and thickness Δz_L

z: depth of formation

z_l: lower boundary of layer Y

z_u: upper boundary of layer Y

Z: phase delay

List of acronyms

1D: one-dimensional

2D: two-dimensional

3D: three-dimensional

2DFD: two-dimensional finite difference

2DFE: two-dimensional finite element

3D-TDFD: three-dimensional time-domain finite difference

CPU: central processing unit

FWHM: full-width at half-maximum

GR: gamma ray

GPa: gigaPascal (10^9 Pascal)

LWD: logging while drilling

RAM: random-access memory

RMS: root-mean-square

STC: slowness time coherence

TI: transversely isotropic

VTI: vertical transversely isotropic

References

Aki, K., and P. G. Richards, 2002, Quantitative Seismology, Second edition: University Science Books.

Aster, R. C., B. Borchers, and C. H. Thurber, 2005, Parameter estimation and inverse problems: Elsevier Academic.

Berryman, J., V. Grechka, and P. A. Berge, 1999, Analysis of Thomsen parameters for finely layered VTI media: Geophysical Prospecting, **47**, p. 959–978, doi:10.1046/j.1365-2478.1999.00163.x.

Burridge, R., and B. Sinha, 1996, Inversion for formation shear modulus and radial depth of investigation using borehole flexural waves: Society of Exploration Geophysicists, SEG Technical Program Expanded Abstracts, p. 158–161, doi:10.1190/1.1826426.

Byun, J., and N. M. Toksöz, 2006, Effects of an off-centered tool on dipole and quadrupole logging: Geophysics, **71**, no. 4, p. F91–F100, doi:10.1190/1.2217368.

Cheng, C. H., and X. M. Tang, 1993, Effects Of A Logging Tool On The Stoneley Waves In Elastic And Porous Boreholes: The Log Analyst, **34**, no. 05.

Chi, S., and X. M. Tang, 2003, Accurate Approximations To Qsv And Qp Wave Speeds In Tiv Media And Stoneley Wave Speed In General Anisotropic Media: Society of Petrophysicists and Well-Log Analysts.

Chi, S., C. Torres-Verdin, J. Wu, and F. O. Alpak, 2006, Assessment of Mud-Filtrate-Invasion Effects on Borehole Acoustic Logs and Radial Profiling of Formation Elastic Properties: SPE Reservoir Evaluation & Engineering, **9**, no. 05, p. 553–564, doi:10.2118/90159-PA.

Close, D., D. Cho, F. Horn, and H. Edmundson, 2009, The sound of sonic: A historical perspective and introduction to acoustic logging: CSEG Recorder, **34**, no. 05, p. 34–43.

Daley, P. F., and F. Hron, 1977, Reflection and transmission coefficients for transversely isotropic media: Bulletin of the Seismological Society of America, **67**, no. 3, p. 661–675.

Ellis, D. V., and J. M. Singer (eds.), 2007, Well Logging for Earth Scientists: Dordrecht, Springer Netherlands, doi:10.1007/978-1-4020-4602-5.

Fjar, E., R. M. Holt, A. M. Raaen, R. Risnes, and P. Horsrud, 2008, Petroleum Related Rock Mechanics, Second edition: Elsevier B.V.

Foti, S., L. Sambuelli, L. V. Socco, and C. Strobbia, 2002, Spatial sampling issues in fk analysis of surface waves: Society of Exploration Geophysicists, p. SEI8-SEI8.

Hill, R., 1965, A self-consistent mechanics of composite materials: Journal of the Mechanics and Physics of Solids, **13**, no. 4, p. 213–222, doi:10.1016/0022-5096(65)90010-4.

Hornby, B., L. Schwartz, and J. Hudson, 1994, Anisotropic effective-medium modeling of the elastic properties of shales: Geophysics, **59**, no. 10, p. 1570–1583, doi:10.1190/1.1443546.

Hornby, B., X. Wang, and K. Dodds, 2003, Do We Measure Phase or Group Velocity with Dipole Sonic Tools? 65th EAGE Conference & Exhibition.

Hsu, K., and S. Chang, 1987, Multiple-shot processing of array sonic waveforms: Geophysics, **52**, no. 10, p. 1376–1390, doi:10.1190/1.1442250.

Huang, S., P. Matuszyk, J. Ma, and C. Torres-Verdín, 2013, Abnormal sonic dispersive-mode responses in high-angle wells: Joint Industry Research Consortium on Formation Evaluation 13th Annual Meeting, 115.

Huang, S., P. J. Matuszyk, and C. Torres-Verdín, 2015, Spatial sensitivity functions for rapid numerical simulation of borehole sonic measurements in vertical wells: Geophysics, **80**, no. 5, p. D459–D480, doi:10.1190/geo2014-0587.1.

Huang, S., and C. Torres-Verdín, 2017, Fast-forward modeling of compressional arrival slowness logs in high-angle and horizontal wells: Geophysics, **82**, no. 2, p. D107–D122, doi:10.1190/geo2016-0317.1.

Huang, S., and C. Torres-Verdín, 2016, Inversion-based interpretation of borehole sonic measurements using semianalytical spatial sensitivity functions: Geophysics, **81**, no. 2, p. D111–D124, doi:10.1190/geo2015-0335.1.

Kimball, C., and T. Marzetta, 1984, Semblance processing of borehole acoustic array data: Geophysics, **49**, no. 3, p. 274–281, doi:10.1190/1.1441659.

King, G. E., 2010, Thirty Years of Gas Shale Fracturing: What Have We Learned? Society of Petroleum Engineers, doi:10.2118/133456-MS.

Kosset, T. B., and A. N. Tutuncu, 2015, A Case Study for Wellpath Optimization and Drilling Risk Reduction for Vaca Muerta Shale in Argentina: 49th U.S. Rock Mechanics/Geomechanics Symposium, American Rock Mechanics Association.

Lee, S.-Q., X.-M. Tang, Y. Su, and C.-X. Zhuang, 2016, Model-based dispersive processing of borehole dipole wave data using an equivalent-tool theory: Geophysics, **81**, no. 1, p. D35–D9, doi:10.1190/geo2015-0210.1.

Lee, M. W., and W. F. Waite, 2008, Estimating pore-space gas hydrate saturations from well log acoustic data: Geochemistry, Geophysics, Geosystems, **9**, no. 7, p. Q07008, doi:10.1029/2008GC002081.

Liu, Q., E. Schoen, F. Daube, C. Randall, H. Liu, and P. Lee, 1996, A three-dimensional finite difference simulation of sonic logging: The Journal of the Acoustical Society of America, **100**, no. 1, p. 72–79, doi:10.1121/1.415869.

Luo, Y., and G. Schuster, 1991, Wave-equation traveltime inversion: GEOPHYSICS, **56**, no. 5, p. 645–653, doi:10.1190/1.1443081.

Ma, J., R. Wang, and C. Torres-Verdín, 2013, 3D simulation of acoustic waveforms in high-angle wells in the presence of the tool mandrel: Joint Industry Research Consortium on Formation Evaluation 13th Annual Meeting, 159.

Maalouf, E., and C. Torres-Verdin, 2017, Inversion-based method to mitigate noise in borehole sonic logs: (submitted for publication).

Mallan, R., J. Ma, C. Torres-Verdin, and G. L. Wang, 2009, Joint Radial Inversion of Resistivity and Sonic Logs To Estimate In Situ Petrophysical and Elastic Properties of Formations: Society of Petroleum Engineers, doi:10.2118/124624-MS.

Mallan, R., C. Torres-Verdín, and J. Ma, 2011, Simulation of borehole sonic waveforms in dipping, anisotropic, and invaded formations: Geophysics, **76**, no. 4, p. E127–E139, doi:10.1190/1.3589101.

Market, J., C. Barnett, R. Deady, G. Althoff, G. L. Varsamis, and J. Blanch, 2001, New Processing Techniques to Meet Challenges of LWD Acoustic Logging: Society of Petroleum Engineers, doi:10.2118/71731-MS.

Matuszyk, P., and C. Torres-Verdín, 2014, Frequency-domain simulation of logging-while-drilling borehole sonic waveforms: Geophysics, **79**, no. 2, p. D99–D113, doi:10.1190/geo2013-0279.1.

Matuszyk, P., C. Torres-Verdín, and D. Pardo, 2013, Frequency-domain finite-element simulations of 2D sonic wireline borehole measurements acquired in fractured and thinly bedded formations: Geophysics, **78**, no. 4, p. D193–D207, doi:10.1190/geo2012-0397.1.

Miller, D., S. Horne, and J. Walsh, 2012, Precise inversion of logged slownesses for elastic parameters in a gas shale formation: Geophysics, **77**, no. 4, p. B197–B206, doi:10.1190/geo2011-0334.1.

Murphy, E., S. R. Barraza, M. Gu, D. Gokaraju, M. E. Far, and J. Quirein, 2015, New Models for Acoustic Anisotropic Interpretation in Shale: Presented at the SPWLA 56th Annual Logging Symposium.

Oyler, D. C., C. Mark, and G. M. Molinda, 2008, Correlation of sonic travel time to the uniaxial compressive strength of US coal measure rocks: Proceedings of the 27th International Ground Control in Mining Conference, Morgantown, WV, p. 338–346.

Pardo, D., P. J. Matuszyk, C. Torres-Verdin, A. Mora, I. Muga, and V. M. Calo, 2013, Influence of borehole-eccentred tools on wireline and logging-while-drilling sonic logging measurements: Geophysical Prospecting, **61**, no. s1, p. 268–283, doi:10.1111/1365-2478.12022.

Peyret, A., and C. Torres-Verdin, 2006, Assessment of shoulder-bed, invasion, and lamination effects on borehole sonic logs: a numerical sensitivity study: Presented at the SPWLA 47th Annual Logging Symposium, Veracruz, Mexico.

Prioul, R., and J. Jocker, 2009, Fracture characterization at multiple scales using borehole images, sonic logs, and walkaround vertical seismic profile: AAPG Bulletin, **93**, no. 11, p. 1503–1516.

Sams, M., 1995, Attenuation and anisotropy: The effect of extra fine layering: Geophysics, **60**, no. 6, p. 1646–1655, doi:10.1190/1.1443897.

Sayar, P., and C. Torres-Verdín, 2016, Using anisotropic effective medium theories to quantify elastic properties of sandstone-shale laminated rocks: Geophysics, **81**, no. 4, p. D315–D333, doi:10.1190/geo2015-0323.1.

Scheibner, D., S. Yoneshima, Z. Zhang, W. Izuhara, Y. Wada, P. Wu, F. Pampuri, and M. Pelorosso, 2010, Slow Formation Shear From An Lwd Tool: Quadrupole Inversion With A Gulf Of Mexico Example: SPWLA 51st Annual Logging Symposium.

Shuey, R. T., 1985, A simplification of the Zoeppritz equations: Geophysics, **50**, no. 4, p. 609–614, doi:10.1190/1.1441936.

Sinha, B. K., 1997, Sensitivity and inversion of borehole flexural dispersions for formation parameters: Geophysical Journal International, **128**, no. 1, p. 84–96, doi:10.1111/j.1365-246X.1997.tb04073.x.

Sinha, B., A. Donald, J. Walsh, and T. Lei, 2014, Anisotropic elastic constants from dipole flexural dispersions in unconventional shale-gas reservoirs: Society of Exploration Geophysicists, SEG Technical Program Expanded Abstracts, p. 596–600, doi:10.1190/segam2014-0193.1.

Sinha, B., A. Norris, and S. Chang, 1994, Borehole flexural modes in anisotropic formations: Geophysics, **59**, no. 7, p. 1037–1052, doi:10.1190/1.1443660.

Sinha, B., E. Şimşek, and S. Asvadurov, 2009, Influence of a pipe tool on borehole modes: Geophysics, **74**, no. 3, p. E111–E123, doi:10.1190/1.3085644.

Sinha, B., E. Şimşek, and Q. Liu, 2006a, Elastic-wave propagation in deviated wells in anisotropic formations: Geophysics, **71**, no. 6, p. D191–D202, doi:10.1190/1.2358402.

Sinha, B., B. Vissapragada, L. Renlie, and S. Tysse, 2006b, Radial profiling of the three formation shear moduli and its application to well completions: Geophysics, **71**, no. 6, p. E65–E77, doi:10.1190/1.2335879.

Sinha, B., L. Xu, O. Magbagbeola, and K. Macphail, 2016, A new workflow for geomechanical analyses in the Marcellus Shale Gas Basin: Society of Exploration Geophysicists, SEG Technical Program Expanded Abstracts, p. 652–656, doi:10.1190/segam2016-13778225.1.

Song, X., Y. Zhao, and J. Dykstra, 2017, Active Damping of Acoustic Ringing Effect for Oil Well Sonic Logging System: IEEE Transactions on Industrial Electronics, **64**, no. 4, p. 3423–3432, doi:10.1109/TIE.2016.2598315.

Souder, W. W., 2002, Using Sonic Logs To Predict Fluid Type: Petrophysics, **43**, no. 05.

Spikes, K. T., 2014, Error estimates of elastic components in stress-dependent VTI media: Journal of Applied Geophysics, **108**, no. Supplement C, p. 110–123, doi:10.1016/j.jappgeo.2014.06.015.

Stephen, R., F. Cardo-Casas, and C. Cheng, 1985, Finite-difference synthetic acoustic logs: Geophysics, **50**, no. 10, p. 1588–1609, doi:10.1190/1.1441849.

Su, Y.-D., X.-M. Tang, C. Hei, and C.-X. Zhuang, 2011, An equivalent-tool theory for acoustic logging and applications: Applied Geophysics, **8**, no. 1, p. 69–78, doi:10.1007/s11770-011-0272-6.

Su, Y., X. Tang, C. Zhuang, S. Xu, and L. Zhao, 2013, Mapping formation shear-velocity variation by inverting logging-while-drilling quadrupole-wave dispersion data: Geophysics, **78**, no. 6, p. D491–D498, doi:10.1190/geo2013-0136.1.

Suarez-Rivera, R., and T. R. Bratton, 2009, Estimating horizontal stress from three-dimensional anisotropy, U. S. Patent 8,175,807 B2.

Tang, X., and C. Cheng, 1996, Fast inversion of formation permeability from Stoneley wave logs using a simplified Biot-Rosenbaum model: Geophysics, **61**, no. 3, p. 639–645, doi:10.1190/1.1443993.

Tang, X.-M., and C. H. A. Cheng, 2004, Quantitative Borehole Acoustic Methods: Gulf Professional Publishing, 280 p.

Thompson, D., and D. Burns, 1989, Multi-Shot Processing For Better Velocity Determination, Technical Report: Massachusetts Institute of Technology, Earth Resources Laboratory.

Thomsen, L., 1986, Weak elastic anisotropy: Geophysics, **51**, no. 10, p. 1954–1966, doi:10.1190/1.1442051.

Tutuncu, A. N., 2010, Anisotropy, Compaction And Dispersion Characteristics of Reservoir And Seal Shales: American Rock Mechanics Association.

Vernik, L., and X. Liu, 1997, Velocity anisotropy in shales: A petrophysical study: Geophysics, **62**, no. 2, p. 521–532, doi:10.1190/1.1444162.

Walsh, J., B. Sinha, and A. Donald, 2006, Formation Anisotropy Parameters Using Borehole Sonic Data: SPWLA 47th Annual Logging Symposium.

Walsh, J., B. Sinha, T. Plona, D. Miller, D. Bentley, and M. Ammerman, 2007, Derivation of anisotropy parameters in a shale using borehole sonic data: Society of Exploration Geophysicists, SEG Technical Program Expanded Abstracts, p. 323–327, doi:10.1190/1.2792435.

Wang, R., W. Herrera, and C. Torres-Verdín, 2017, Simulation and interpretation of sonic waveforms in high-angle and horizontal wells: Geophysics, **82**, no. 4, p. D251–D263, doi:10.1190/geo2016-0402.1.

Wang, X., B. Hornby, and K. Dodds, 2002, Dipole sonic response in deviated boreholes penetrating an anisotropic formation: Society of Exploration Geophysicists, SEG Technical Program Expanded Abstracts, p. 360–363, doi:10.1190/1.1817253.

Wang, R. J., W. X. Qiao, and X. H. Che, 2010, A new method of extracting shear slowness from borehole mode waves: 3rd International Congress on Image and Signal Processing, p. 4308–4312, doi:10.1109/CISP.2010.5647298.

Willis, M. J., A. N. Tutuncu, and T. Bratton, 2014, A Novel Approach to Upscaling Elastic Moduli in Unconventional Reservoirs: 48th U.S. Rock Mechanics/Geomechanics Symposium, American Rock Mechanics Association.

Winkler, K., B. Sinha, and T. Plona, 1998, Effects of borehole stress concentrations on dipole anisotropy measurements: Geophysics, **63**, no. 1, p. 11–17, doi:10.1190/1.1444303.

Wu, T. T., 1966, The effect of inclusion shape on the elastic moduli of a two-phase material: International Journal of Solids and Structures, **2**, no. 1, p. 1–8, doi:10.1016/0020-7683(66)90002-3.

Wyllie, M., A. Gregory, and L. Gardner, 1956, Elastic wave velocities in heterogeneous and porous media: Geophysics, **21**, no. 1, p. 41–70, doi:10.1190/1.1438217.

Yan, F., D. Han, X. Chen, and S. Sil, 2016, Analysis of seismic anisotropy parameters for sedimentary strata: Society of Exploration Geophysicists, SEG Technical Program Expanded Abstracts, p. 3502–3507, doi:10.1190/segam2016-13777643.1.

Zharnikov, T. V., D. E. Syresin, and C.-J. Hsu, 2013, Calculating the spectrum of anisotropic waveguides using a spectral method: The Journal of the Acoustical Society of America, **134**, no. 3, p. 1739–1753, doi:10.1121/1.4817839.

Zheng, Y., X. Huang, and M. Toksöz, 2004, A finite element analysis of the effects of tool eccentricity on wave dispersion properties in borehole acoustic logging while drilling: Society of Exploration Geophysicists, SEG Technical Program Expanded Abstracts, p. 294–297, doi:10.1190/1.1839721.